Aix-Marseille Université

Ecole Doctorale ED 352
PHYSIQUE ET SCIENCES DE LA MATIÈRE

Ph.D THESIS

to obtain the title of

Ph.D of Science

of the Université d'Aix-Marseille

Specialty : Optics and Photonics

defended by

Brice Rolly

Subwavelength photonic resonators for enhancing light-matter interactions

Thesis Advisors: Brian Stout, Nicolas Bonod

prepared at the **Institut Fresnel**, CLARTÉ team

defended on October **, 2013

Jury :

Reviewers:	Niek van Hulst	-	iCrea (ICFO)
	Jean-Jacques Greffet	-	Inst. d'Optique (Lab. Charles Fabry)
Advisors:	Brian Stout	-	CNRS / U. d'Aix-Marseille (Inst. Fresnel)
	Nicolas Bonod	-	CNRS / U. d'Aix-Marseille (Inst. Fresnel)
Examinators:	Stefan Enoch	-	CNRS / U. d'Aix-Marseille (Inst. Fresnel)
	Frédérique De Fornel	-	CNRS / U. de Bourgogne (ICB)

Remerciements

I want to thank my thesis advisors, Brian Stout and Nicolas Bonod, for these three years of studies under their supervision. I owe them a major part of my scientific training. They spent considerable amounts of time and efforts in supervising me, and they are mainstays of this thesis.

I also wish to warmly thank Niek van Hulst, Jean-Jacques Greffet, Fréderique De Fornel and Stefan Enoch for taking part in my defense committee. I am particularly grateful to Niek van Hulst and Jean-Jacques Greffet for accepting to review this manuscript.

This thesis was carried out in the Institut Fresnel, in the St-Jérôme campus of my employer, Aix-Marseille Université, and under the academic authority of École Doctorale 352. I want to thank all the people that allow the proper functioning of those great institutions.

I would like to thank everyone I had the great opportunity to collaborate and interact with. I have a special thought for Alexis Devilez, for the good times we spent together. I also address my warm thanks to Stefan Varault, Guillaume Boudarham, Betina Bebey, Abir Tahri, Mandiaye Fall, and Victor Grigoriev of the CLARTÉ team. I am very grateful to Sébastien Bidault and Mickaël Busson from Institut Langevin. I also thank Redha Abdeddaïm and Jean-Michel Geffrin from the HIPE team; and Pierre Bon, Jérôme Wenger, Hervé Rigneault and Serge Monneret from the MOSAIC team, at Institut Fresnel.

I also thank all the Ph.D candidates, post-docs and permanent employee, both administrative and scientific, of Institut Fresnel, for the great atmosphere in the cofee room. I give a particular thank to those I had the pleasure to have extensive discussions with: Thomas Begou, Aurélie Bétourné, Pascal Berto, Benjamin Vial, Fatma-Zohra Bioud, Guillaume Demesy, Petru Ghenuche, Vincent Debierre, Guillaume Dupont, Soufiane Nounouh, Marc Traversari and Francesco Pastorelli.

J'ai une pensée chaleureuse pour les coqlocs, dans le désordre chronologique: Georges IInd, Mathou, Georges I^{er}, JiPi, Marie, Jana, Rohan-Jean, Laura, Maria-La, Flo, Raphaël, Mona, Adrien, Quentin, Laurent, Julien, JiBi, Sophie, Antoine Jr, Sarah, tous les coqlocs d'un soir, d'une semaine, ou plus, ceux que j'oublie, et bien sûr Antoine (St-Just en force). Je veux aussi remercier Manon, qui m'a épaulé dans des moments difficiles, et m'a été d'un secours vital.

Enfin je remercie mes parents, ma famille, et tous mes amis, sans qui tout cela ne serait pas arrivé!

So close, no matter how far
Couldn't be much more from the heart
Forever trusting who we are
And nothing else matters

Never opened myself this way
Life is ours, we live it our way
All these words I don't just say
And nothing else matters

Trust I seek and I find in you
Every day for us something new
Open mind for a different view
And nothing else matters

Never cared for what they do
Never cared for what they know
But I know

So close, no matter how far
Couldn't be much more from the heart
Forever trusting who we are
And nothing else matters

Never cared for what they do
Never cared for what they know
But I know

Never opened myself this way
Life is ours, we live it our way
All these words I don't just say

Trust I seek and I find in you
Every day for us, something new
Open mind for a different view
And nothing else matters

Never cared for what they say
Never cared for games they play
Never cared for what they do
Never cared for what they know
And I know

So close, no matter how far
Couldn't be much more from the heart
Forever trusting who we are
No, nothing else matters

Metallica, "*Nothing Else Matters*" (1991)

Contents

Chapter 1

Introduction

"A journey of a thousand li *starts with a single step."*
Lao Tzu, Chinese philosopher
(around $6^{\text{th}} - 5^{\text{th}}$ century B.C.)

Contents

Optical antennas act as transducers of the visible spectrum electromagnetic fields: they convert electromagnetic power coming from the far-field (*i.e.* from sources "infinitely" far away), to localized electromagnetic power, and vice versa. They are thus able to convert freely-propagating light beams into sub-wavelength, high intensity "hot spots", the power being then readily available to sub-wavelength sized absorbers, *e.g.* fluorescent molecules, thereby increasing the excitation rate of those molecules, since more photons per unit time are available in their immediate proximity. Reciprocally, for a light emitter in an excited state, optical antennas can enhance both its radiative and non-radiative decay rates, since antenna elements act as secondary sources that scatter light back onto the emitter, thereby modifying the power that the emitter dissipates for a given transition dipole moment. Scattered and emitted fields also interfere in the far-field, thereby modifying the radiation pattern of the emission. The outline of this thesis is based on this dual behavior of optical antennas: chapter 2 treats the case of a far-field excitation of the antenna structure, while chapter 3 treats the case of the local excitation of the antenna, *via* a point dipole light source that is placed near the antenna structure.

Throughout this thesis, we adopt a multipole formulation of the electromagnetic fields based on the separation of variables treatment of the the Helmholtz equation in spherical coordinates. The angular variations of the electromagnetic fields can be developed in terms of Laplace's spherical harmonics. Two linearly independent solutions for the radial dependence of the equations, the scattered fields and the incident fields, are discriminated by imposing different boundary conditions on a spherical surface enclosing the origin. Scattered fields are characterized by an outgoing Poynting vector at every point of the boundary, which means that they enclose a source; their radial dependence is described using outgoing spherical Hankel functions and their derivatives. Incident fields are characterized by a null Poynting vector flux through the boundary (*e.g.* a plane wave that travels through the sphere) and correspond to the superposition of a scattered field and an opposite, "ingoing" field that cancels source divergences, their dependence is described using spherical Bessel functions and their derivatives.

In this manuscript, we analyze and theoretically conceive optical antennas employing sub-wavelength resonators made of metallic or dielectric materials. The resonances of the scatterers, or ensemble of scatterers, can be defined by resonances of their T-matrix eigenvalues, which in the multipole formalism, link the coefficients of the scattered fields to those of the incident fields. In most of our examples (with the only notable exception of section 2.2) we privilege scatterers that are spherical, and made of homogeneous materials; which ensures that the diagonal scalar T-matrix assumption (see glossary) is verified. This assumption considerably reduces the complexity of explicit formulas, and thus allows more intuitive insight for the physical phenomenons under study. Moreover, the individual response of the scatterers is known for those homogeneous spherical particles (in terms of explicit functions of their radius, size and permittivity): it is given by Mie theory [Mie 1908]; in contrast, there is generally no known solution in the case of non-spherical shapes and/or inhomogeneous materials. Nevertheless, multiple-scattering T-matrix theory is not restricted to spherical scatterers, and the formulas we derive could be extended to non-spherical and/or inhomogeneous scatterers. In this case, the computation of numerical values requires numerical estimates of the T-matrix of the individual scatterers, which is possible, *e.g.* using Discrete Dipole Approximation (DDA) and derived methods [Evlyukhin 2011].

The mathematical demonstrations of most of the formulas given in the main text are relegated to the appendices: appendix A presents the multipole expansion of the electromagnetic fields; appendix B treats the Mie theory for single particles; appendix C gives a derivation of the multiple scattering T-matrix; appendix D contains the derivation of formulas for figure of merit computations, and appendix E gives a derivation of the different simplified models that are used throughout the manuscript.

1.1 Sub-wavelength photonic resonators

We consider a homogeneous, spherical particle of radius a, made of an isotropic material of relative permittivity ε_s, embedded in a background medium of relative permittivity ε_b and refractive index $n_b = \sqrt{\varepsilon_b}$ (since they are highly uncommon in the visible spectrum, we do not consider materials with non-unit relative permeability). We further assume that a plane wave of frequency $\omega = 2\pi\frac{c}{\lambda_0}$ (λ_0 is the vacuum wavelength), characterized by an electric field $\mathbf{E}(\omega)$, is incident on the particle. The wave vector is $k_b = 2\pi\frac{n_b}{\lambda_0}$ in the embedding medium, and $k_s = 2\pi\frac{n_s}{\lambda_0}$ inside the sphere.

We present below the effect of this plane-wave excitation, assuming a linear response of the scatterer. Since the scatterers are typically sub-wavelength, it is convenient to describe their response within the multipole expansion of the fields (see appendix A): in this case, a somewhat low maximal multipolarity order $n_{\max}$ is required in order to accurately describe the scattering process, typically, $n_{\max} \approx \text{floor}(a|k_s|) + 1$ in the present case of a plane wave excitation. The response of the spheres is thus characterized by the excitation of induced dipoles and multipoles. These originate from the bond and free polarization charges produced by the incident field inside the scatterers. We will first consider the electric dipole resonances of metals, and explain their origin under a quasi-static framework, then we will introduce the multipole resonances by taking into account the finite size of metallic particles. Next, we will introduce the dipole and multipole resonances of dielectric particles, which can be of electric as well as magnetic nature.

1.1.1 Electric resonances in metallic particles

Electric dipoles: The induced electric dipole moment $\mathbf{p}(\omega)$ inside the sphere is proportional to the incoming field and to its electric dipole polarizability $\alpha(\omega)$: [Jackson 1999]

$$\mathbf{p}(\omega) \equiv \varepsilon_0\varepsilon_b\alpha(\omega)\mathbf{E}(\omega),$$

For particles sufficiently small compared to the wavelength ($a \ll \lambda$), the polarizability can be derived from the Clausius-Mossotti relation:

$$\alpha_{\text{qs}}(\omega) = 3V\frac{\varepsilon_s - \varepsilon_b}{\varepsilon_s + 2\varepsilon_b}, \tag{1.1}$$

where $V = 4\pi a^3/3$ is the sphere's volume and the (qs) subscript denotes the quasi-static approximation. For metallic particles, since $\Re(\varepsilon_s) < 0$, equation 1.1 predicts that whenever $\Re(\varepsilon_s + 2\varepsilon_b) = 0$, the polarizability can be resonant, $\alpha = 3V\frac{i\Im(\varepsilon_s)-3\varepsilon_b}{i\Im(\varepsilon_s)} = 3V\left(1 + \frac{3i\varepsilon_b}{\Im(\varepsilon_s)}\right)$, if the imaginary part of the relative permittivity of the metal at the same frequency, $\Im(\varepsilon_s)$ is low compared to $3\varepsilon_b$. In this case, the polarizability α can be approximated as a large imaginary number, $\alpha \approx 9V\frac{i\varepsilon_b}{\Im(\varepsilon_s)}$. This means that the induced dipole moment $\mathbf{p}$ will be resonant, and have a $+\pi/2$ relative phase with respect to the incoming field. This large induced dipole will produce a strong electric field in the vicinity of the scatterer, even for very small

particles of metal (see figure 1.1). In the surrounding homogeneous medium, the electric field produced by the induced dipole can be cast [Jackson 1999]:

$$\mathbf{E}_{\text{scat}}(\mathbf{r}) = \frac{e^{ikr}}{4\pi\varepsilon_s\varepsilon_0 r^3}\left\{k^2r^2(\hat{\mathbf{r}}\times\mathbf{p})\times\hat{\mathbf{r}} + (1-ikr)\left[3(\hat{\mathbf{r}}\cdot\mathbf{p}\hat{\mathbf{r}} - \mathbf{p}\right]\right\}. \qquad (1.2)$$

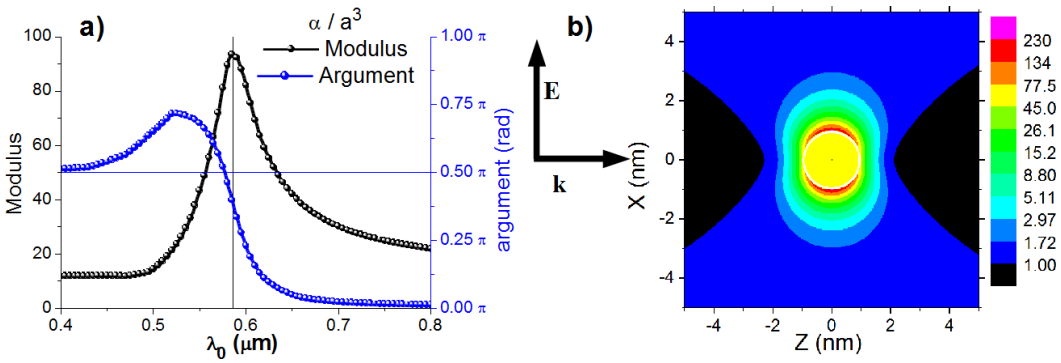

Figure 1.1: (a) (Black line, left scale) Modulus, and (blue line, right scale) argument of the theoretical volumic polarizability, $\alpha(\omega)/a^3$, given by Mie theory for a gold sphere (refractive index taken from experimental bulk values [Johnson 1972]) of radius 1 nm, embedded into a $n_b = 2$ medium, as functions of the vacuum wavelength λ_0. The horizontal blue line indicates the $\pi/2$ argument value, and the black vertical line indicates the abscissa of the maximal polarizabilitymodulus. (b) Theoretical electric field intensity map at the polarizability resonance ($\lambda_0 = 586$ nm) of the sphere. The intensity is normalized by the incoming field's intensity.

The induced dipole resonance will also result in a resonant light scattering, the scattered power W_{scat} being proportional to $\frac{|\alpha|^2}{\lambda^4}$. The metallic sphere will also resonantly dissipate energy *via* ohmic losses; the sum of the scattered power plus the power dissipated by ohmic losses, W_{ext}, is proportional to $\frac{\Im(\alpha)}{\lambda}$ [Bohren 1983]. We recall that in the derivation of equation 1.1, the $a \ll \lambda$ assumption represents a quasi-static approximation: in order to derive the polarizability in the form of equation 1.1, the incoming electric field is assumed to be *constant* over the volume of the particle. Since $\alpha \propto V \propto a^3 \ll \lambda^3$, one consequence of equation 1.1 is that the induced dipole resonance of small metallic particles mainly leads to ohmic dissipation of the energy of the incoming field:

$$W_{\text{ext}} \propto \frac{\Im(\alpha)}{\lambda} \propto a^3\frac{3\varepsilon_b}{\Im(\varepsilon_s)\lambda} \ll \lambda^2 \quad (\text{since } a \ll \lambda)$$

$$W_{\text{scat}} \propto \frac{|\alpha|^2}{\lambda^4} \approx V^2\frac{9\varepsilon_b^2}{\Im(\varepsilon_s)^2\lambda^4} \propto a^6\frac{9\varepsilon_b^2}{\Im(\varepsilon_s)^2\lambda^4} \approx \frac{W_{\text{ext}}^2}{\lambda^2} \ll W_{\text{ext}}$$

However, the quasistatic approximation of the electric dipole polarizability (equation 1.1) does not comply with the "optical theorem" [Colas des Francs 2008].

One can use a corrected form of the quasi-static electric dipole polarizability in order to satisfy the optical theorem; this is done by including a radiation damping and a dynamic polarization term into the polarizability [Colas des Francs 2008]:

$$\alpha_{\text{corr}} = \frac{\alpha_{\text{qs}}}{1 - [(1 - ik_b a)e^{ik_b a} - 1]\frac{1}{2\pi a^3}\alpha_{\text{qs}}}. \tag{1.3}$$

This model thus takes into account the first corrections to the polarizability of the particle, that are induced by its finite size. When the particle becomes comparable in size with the wavelength (diameter $2a \lesssim \lambda$), the more accurate description of the polarizability α shows that metallic particles whose size are smaller than (but not negligible compared to) the wavelength can radiate more power than they dissipate in ohmic losses. The exact solution of the dipole polarizability of spherical particles can be derived from Mie theory[Mie 1908]: Mie solved the scattering problem for spherical scatterers of arbitrary size – though this method is impractical for scatterers that are too large compared to the wavelength. Using Mie theory, the electric dipole polarizability can be cast:

$$\alpha_{\text{Mie}} = 6\pi a_1/(ik^3), \tag{1.4}$$

where a_1 is the electric dipole Mie coefficient of the sphere (see section 1.3.3.1).

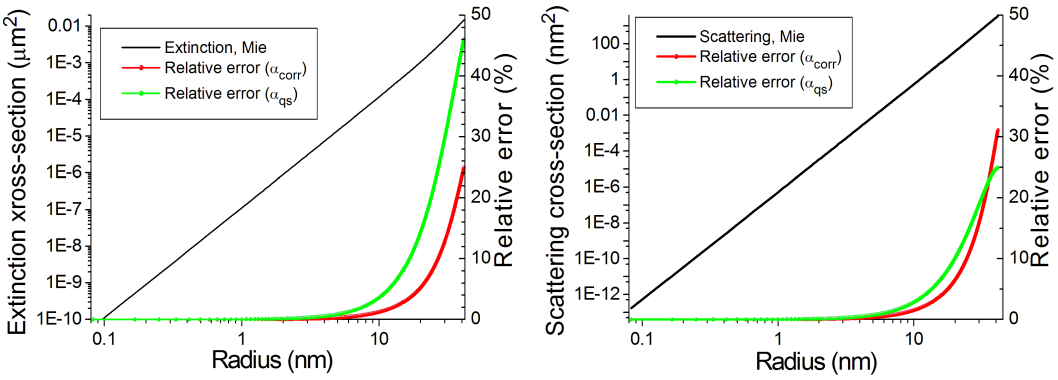

Figure 1.2: (Black lines, left scale) (left) Extinction and (right) scattering cross-sections for a hypothetical gold sphere (permittivity $\varepsilon_s = -3.946161 + 2.58044i$ corresponding to $\lambda = 521$ nm bulk material value [Johnson 1972], chosen at the small radius extinction resonance in the optical domain) as a function of the radius. The embedding medium is vacuum, $n_b = 1$. (Right scale) Relative errors when using the polarizabilities of the (red line) corrected polarizability of equation 1.3, (green line) quasi-static polarizability of equation 1.1, instead of the Mie theory.

In figure 1.2 we see that the quasi-static polarizability approximation holds when considering resonant metallic particles under ≈ 10 nm in radius. For radii > 20 nm, neither the quasistatic approximation of the polarizability (equation 1.1), nor the corrected dynamic polarizability (equation 1.3) are within a $< 5\%$ error bound

(compared to Mie theory) for the estimation of the scattered and absorbed powers. As expected, for small radii, the corrected polarizability yields lower error than the quasistatic approximation.

Electric multipoles: Another effect arises when the size of the particle is no longer negligible compared to the wavelength : on account of retardation effects of the incoming field in the volume of the particle, electric multipoles can also be excited in sub-wavelength metallic particles. Indeed, Mie theory predicts that multipoles can also be resonantly excited in spherical scatterers. For metallic particles at optical wavelengths, multipoles (quadrupoles, octopoles, *etc.*) generally lead to a high ohmic dissipation of the incoming electromagnetic field. These induced multipoles are a major obstacle when trying to reduce ohmic losses in designs that use plasmonic resonators. Even at frequencies where the induced quadrupoles and higher order multipoles are not resonant, they can induce high losses. In the case of a fluorescent dye brought to within a few nanometers from the surface of a metallic particle for instance, a high amount of energy is dissipated because of the multipole excitation of the particle, which leads to a drastic decrease of the emission's quantum efficiency [Thomas 2004] (see section 1.2.1 below).

1.1.2 Electric and Magnetic resonances of dielectric particles

The seminal work of Mie [Mie 1908] was originally aimed at the understanding of the colors featured by gold colloidal suspensions, but the so-called "Mie" resonances also occur in dielectrics. We remark two main differences between the resonances in metals and dielectrics. First, the resonances in dielectrics generally require the particle size to be non-negligible compared to the wavelength, whereas highly sub-wavelength sized metallic particles can be resonant in the optical regime. Secondly, dielectric spheres naturally present magnetic resonances, while the resonances of metallic spheres are predominantly of electric nature.

Size comparison: The polarizability of dielectric particles can also be derived from the Clausius-Mossotti relation (equation 1.1) in the quasi-static regime: $\alpha_{\mathrm{qs}}(\omega) = 3V\frac{\varepsilon_s-\varepsilon_b}{\varepsilon_s+2\varepsilon_b}$, which means that no particular resonance is expected for particles of small radius, as opposed to the case of metallic particles where the negative real part of the permittivity ensures a resonance whenever $\Re(\varepsilon_s + 2\varepsilon_b) = 0$. Still, when considering the full analytical result of Mie theory, electric resonances are expected to occur for sub-wavelength dielectric spheres, if the permittivity of the material is sufficiently high. Indeed, we show in figure 1.3 that dielectric particles of relatively high refractive index can present a resonance in terms of volumic polarizability when their size is not too small (*e.g.* for a refractive index $n = 4$ and at $\lambda = 521$ nm, the resonance occurs for a radius $a = 83$ nm).

Magnetic resonances: In the quasi-static approximation, the volumic magnetic polarizability of any spherical scatterer tends to zero, and this is true for any non-

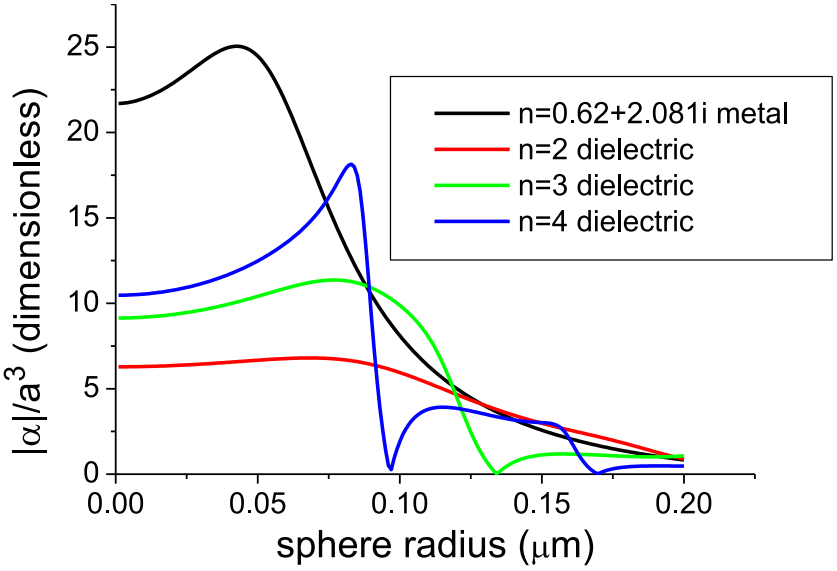

Figure 1.3: Volumic electric dipole polarizabilities as a function of the radius at $\lambda = 521$ nm for spheres embedded in air and made of (black, red, green, and blue lines) gold, and lossless dielectrics of refractive index 2,3, and 4 respectively.

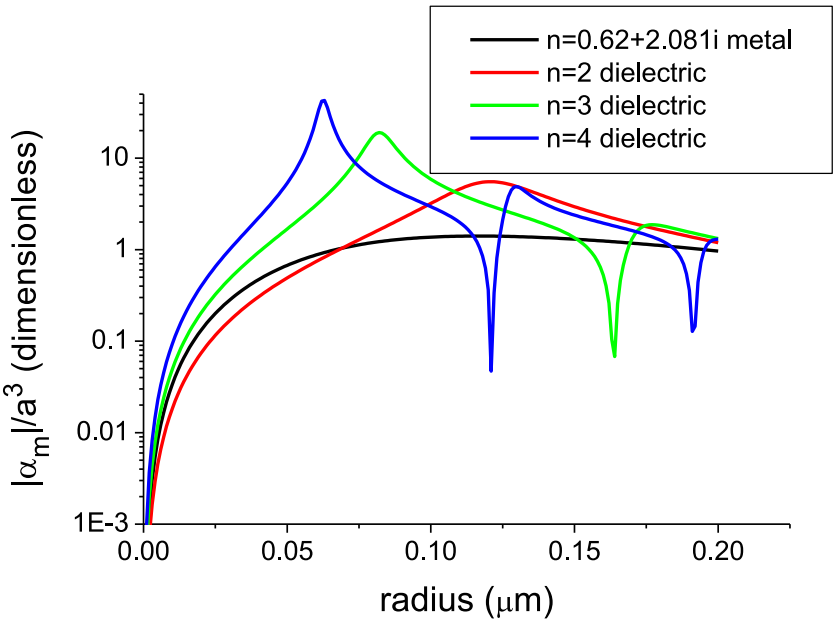

Figure 1.4: Volumic magnetic dipole polarizabilities as a function of the radius at the chosen wavelength $\lambda = 521$ nm for spheres made of (black) gold, (red, green, blue respectively) lossless dielectrics of refractive index 2,3, and 4 respectively. (logarithmic scale)

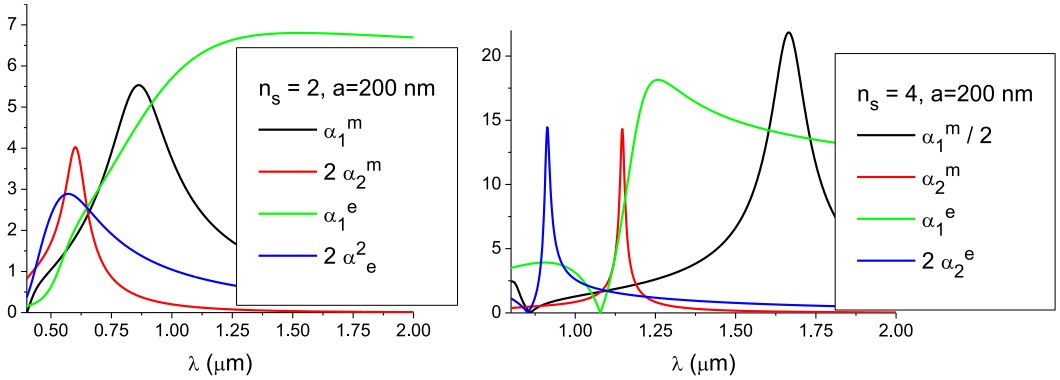

Figure 1.5: Modulus of the volumic polarizabilities, $|\alpha|/a^3$, of a sphere of radius 200 nm, as a function of the wavelength. (left) $n_s = 2$, (right) $n_s = 4$. The coefficients have been scaled by different factors in order to keep the same global scale (see legends). α_n^q is the polarizability of order n and type q (see appendix A)

magnetic material (unit relative permeability). However, when the size of the scatterer is not negligible compared to the wavelength, Mie theory predicts that dielectric particles also present magnetic dipole and multipole resonances (see below equation 1.8). Once again, as seen in figure 1.4, a higher refractive index results in a stronger resonance of the polarizability.

Finally, we want to point out the effect of high refractive index dielectrics on the various resonances. Figure 1.5 is a comparative plot of the first four Mie resonances (electric and magnetic dipoles and quadripoles) for two spheres of radius 200 nm and of refractive index $n_s = 2$ and $n_s = 4$ respectively. We remark three effects of an increase of the refractive index. First, the resonances become narrower (they have a higher quality factor). The quality factor of the resonances also increase with the multipolarity order n. Secondly, in link with the first point, the resonances have a tendency to be more spectrally separated. Finally, the order in which the resonances appear (*e.g.* for increasing frequencies) can be modified: the electric dipole resonance occurs before the magnetic dipole one, when $n_s = 2$ in figure 1.5a; whereas the order is reversed when $n_s = 4$ in figure 1.5b.

1.2 Enhancing light-matter interactions

1.2.1 Enhancing decay rates

Let us consider an atom or molecule with 3 energy states: the ground state (0), and two excited states (1) and (2) (see figure 1.6). An electron may be excited by an incoming photon at frequency ν_{20}, thus bringing the molecule from the ground state (0), to the excited state (2). The latter is considered to decay non-radiatively to the excited state (1), which can spontaneously decay to the ground state, either radiatively (by emitting a photon at frequency ν_{10}), or non-radiatively. Right after

the transition between excited states (2) and (1) occurs, the time interval (averaged over a number of transitions) before the molecule decays to the ground state is called the lifetime, τ, of the excited state (1). This lifetime is a Poisson process: the probability, $P_{\text{exc}}(t)$, that the atom is still in the excited state at time t if it is in the excited state at time $t = 0$, follows an exponential law:

$$P_{\text{exc}}(t) = \mathrm{e}^{-t/\tau} = \mathrm{e}^{-t\Gamma_{\text{tot}}} \qquad (\Gamma_{\text{tot}} \equiv 1/\tau),$$

where the inverse of the lifetime, Γ_{tot}, is called the total decay rate [Novotny 2006]. By decomposing the total decay rate into radiative and non-radiative decay rates, $\Gamma_{\text{tot}} = \Gamma_{\text{rad}} + \Gamma_{\text{nr}}$, we can cast "radiative" and "non-radiative" lifetimes, that are the inverses of the radiative and non-radiative decay rates respectively:

$$\begin{aligned} \tau_{\text{rad}} &= \tfrac{1}{\Gamma_{\text{rad}}} \quad \tau_{\text{nr}} = \frac{1}{\Gamma_{\text{nr}}} \\ \Gamma_{\text{tot}} &= \tfrac{1}{\tau} = \quad \frac{1}{\tau_{\text{rad}}} + \frac{1}{\tau_{\text{nr}}}, \end{aligned}$$

and the probability $P_{\text{exc}}(t)$ can thus be cast:

$$P_{\text{exc}}(t) = \mathrm{e}^{-t/\tau_{\text{rad}}}\mathrm{e}^{-t/\tau_{\text{nr}}} = \mathrm{e}^{-t\Gamma_{\text{rad}}}\mathrm{e}^{-t\Gamma_{\text{nr}}}$$

where the successive exponential decays correspond to the partial probability of a radiative or non-radiative decay, respectively. Thus, when the emitter deexcites, there is a probability:

$$\eta = \frac{\tau}{\tau_{\text{rad}}} = \frac{\Gamma_{\text{rad}}}{\Gamma_{\text{tot}}}$$

that the transition is a radiative one. Since non-radiative transitions are generally an undesirable source of energy dissipation, η is called the quantum efficiency of the emission.

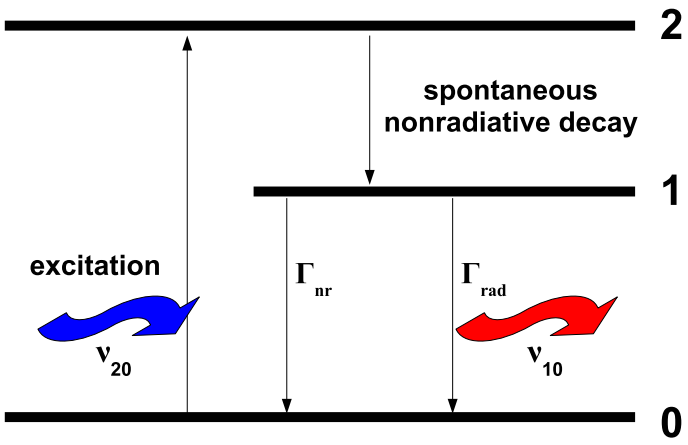

Figure 1.6: The 3-level atom or molecule considered

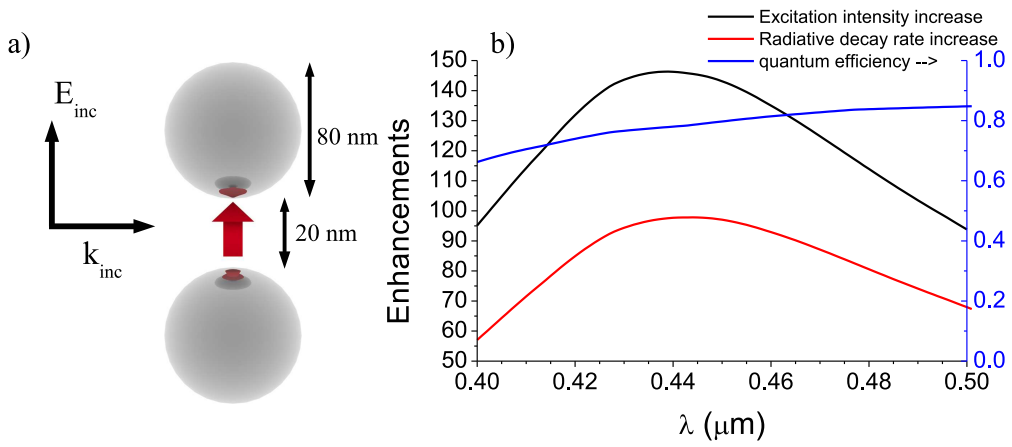

Figure 1.7: (a) Sketch of the considered dimer. The incoming field is either a plane wave with electric field parallel to the gap, or an electric dipole placed at the centre of the dimer and oriented along its axis (red arrow). The spheres are made of silver and the surrounding medium is air. (b) Numerical computation of the enhancements of (black line) excitation and (red line) radiative decay rate; (blue line, right scale) quantum efficiency of the emission, for $\eta_0 = 1$

The decay rates are dependent on the electromagnetic environment of the emitter. Compared to a reference decay rate Γ_0 (*i.e.* the predicted or measured decay rates when the emitter is isolated in vacuum or in a given embedding medium), the modification, Γ/Γ_0, of the decay rate provided by structures like optical antennas can attain several orders of magnitude, *e.g.* for gap structures like bow-tie antennas [Novotny 2011] or dimer antennas [Lereu 2008]; figure 1.7 shows an example, when considering two spherical silver particles 80 nm in diameter and separated by a 20 nm nanogap. The modification of the decay rates, a quantum mechanical phenomenon in essence, can be calculated within a semi-classical approach [Novotny 2006, Greffet 2010, Stout 2011]. This approach uses the Green function of the structure to compute the Local Density of Optical States (LDOS, see *e.g.* [Novotny 2006]).

Lastly we point out that both radiative and non-radiative decay rates can be increased, particularly when using metallic resonators. The quantum efficiency of the $1 \rightarrow 0$ transition for the isolated emitter, $\eta_0 = \Gamma_{\mathrm{rad},0}/\Gamma_{\mathrm{tot},0} = 1 - \Gamma_{\mathrm{nr},0}/\Gamma_{\mathrm{tot},0}$ is also modified when it is coupled to the photonic structure. The new effective quantum efficiency of the $1 \rightarrow 0$ transition, η_{eff}, can be cast: [Bharadwaj 2009]

$$\eta_{\mathrm{eff}} = \tilde{\Gamma}_{\mathrm{rad}}/\left[\tilde{\Gamma}_{\mathrm{tot}} + (1-\eta_0)/\eta_0\right]$$

If the emitter is considered as perfect ($\eta_0 = 1$) then the quantum efficiency reduces to the ratio $\tilde{\Gamma}_{\mathrm{rad}}/\tilde{\Gamma}_{\mathrm{tot}}$.

1.2.2 Enhancing excitation intensities

In order to excite an emitter, one may use an incoming electromagnetic field (like a plane wave, or a focused beam) at a carefully chosen wavelength. In our case, one might want to excite the emitter, modeled here by a 3-level atom (see figure 1.6) from level 0 to 2, by using a laser beam of central frequency $\nu_{20} = \frac{E_2 - E_0}{h}$. In a weak excitation regime (when the atom or molecule decays back to the ground state faster than the available rate of excitation), the excitation rate of a molecule by means of the laser beam is proportional to the square norm of the electric field component parallel to the molecule's dipole orientation $\mathbf{p}$ [Novotny 2006]. Compared to the incoming electromagnetic field $\mathbf{E}_{\text{inc}}$, the modification of the excitation rate provided by the antenna structure can thus be cast:

$$f_{\text{enh,exc}} = \frac{|\mathbf{E}_{\text{tot}} \cdot \mathbf{p}|^2}{|\mathbf{E}_{\text{inc}} \cdot \mathbf{p}|^2}$$

An increased local field intensity at the position of the emitter (more precisely, a higher square norm of the electric field in the direction of the dipole moment of the molecule) thus results in a faster excitation. This means that a lower incoming beam power is required in order to excite the molecule at the same rate. As for the decay rates, an easy and convenient way to achieve high field intensities consists in using a gap antenna structure, such as a bow-tie antenna or a dimer antenna. Figure 1.7b shows the excitation enhancements for the same silver dimer than previously considered.

1.2.3 Enhancing directivity

Emission directivity may be a concern for a number of applications, especially in integrated photonic structures. If the supporting molecule is embedded in a homogeneous medium, most electronic transitions radiate as an electric dipole. Figure 1.8a presents the classical dipole radiation pattern; the molecule radiates isotropically in the plane perpendicular to the dipole transition moment. When using structures like a Yagi-Uda antenna [Taminiau 2008, Curto 2010], a patch antenna [Esteban 2010] or an appropriate dielectric sphere for instance [Devilez 2010, Rolly 2012c], the emission can be rendered more directive (see figure 1.8b).

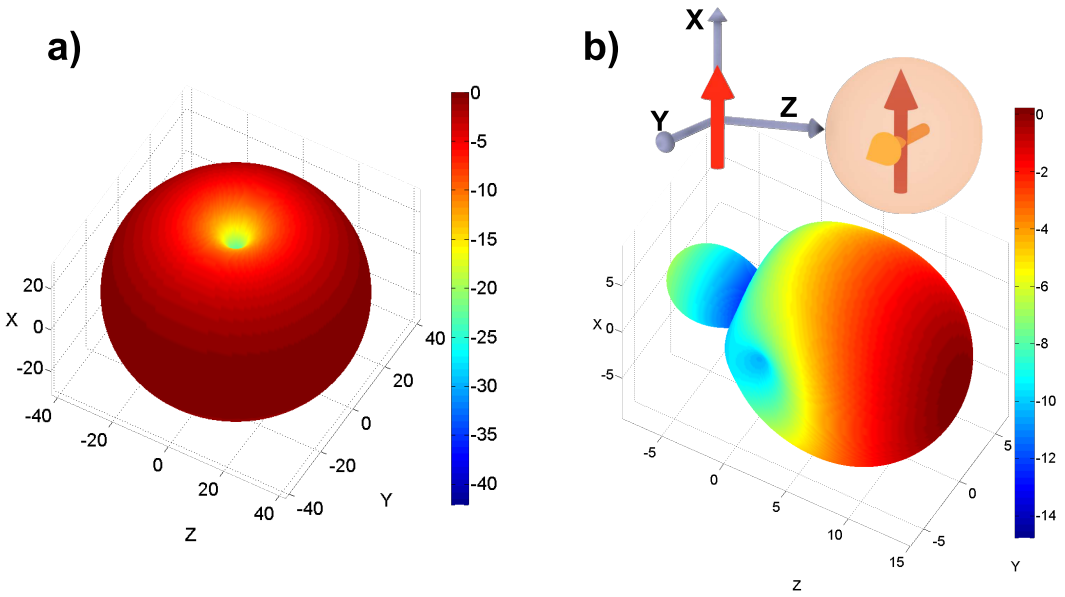

Figure 1.8: Radiation diagrams (in logarithmic scale) at $\lambda_0 = 585$ nm, (a) for an isolated $\hat{\mathbf{x}}$-oriented electric dipole, emission directivity: 1.76 dBi; (b) for an electric dipole coupled to a GaP sphere (refractive index $n = 3.36$) of radius 100 nm with a 5 nm gap on the $\hat{\mathbf{z}}$ axis, emission directivity: 6 dBi. Inset: sketch of the emitter and the induced electric (red) and magnetic (orange) induced dipoles in the sphere. See section 1.3.4.4 for a definition of the directivity expressed in isotropic decibels (dBi).

1.3 Technical introduction

1.3.1 Mathematical and notational conventions

A summarized list of mathematical symbols used in this manuscript is presented on page 105. Here, we will define the basic mathematical notations that will be used throughout the thesis.

1.3.1.1 General notational conventions

Number sets:

- $\mathbb{N}$ is the set of natural numbers : $\{0, 1, 2, 3, 4, \dots\}$.
- $\mathbb{Z}$ is the set of relative integers. Segments of $\mathbb{Z}$ will be written $[a..b]$ where a and b are the extrema.
- $\mathbb{R}$ is the set of real numbers, $\mathbb{C}$ is the set of complex numbers
- excluding 0 from a number set (e.g. $\mathbb{N}$) will be written with an asterisk (e.g. $\mathbb{N}^* = \{1, 2, 3, 4, 5, \dots\}$).

Basic complex operations:

- i is the imaginary number ($i^2 = e^{i\pi} = -1$)
- the complex conjugate of $z = a + ib$ is noted $z^* = a - ib$

Vectorial and tensorial operations:

- vectors and matrices are printed in bold : $\mathbf{x}, \mathbf{M}$
- tensors are hovered by the symbol "$\leftrightarrow$": $\overleftrightarrow{\mathbf{G_0}}$
- the identity matrix (respectively the identity dyad) will be written $\mathbf{Id}$ (respectively $\overleftrightarrow{\mathbf{Id}}$)
- the additive identity will be written 0 regardless of its corresponding set
- the transposed conjugate of a vector or matrix $\mathbf{M} = (m_{i,j})_{i,j}$ is noted $\mathbf{M}^\dagger = (m^*_{j,i})_{i,j}$ – the simple transposition will be indicated by a superscript t: $[m_{i,j}]^t = [m_{j,i}]$
- the scalar product is represented by a central dot: $\mathbf{u} \cdot \mathbf{v} = \sum_i u_i^* v_i$
- a hat above a vector means that it is unitary : $\hat{\mathbf{x}} \cdot \hat{\mathbf{x}} = 1$
- the vector product is represented by a cross : $\hat{\mathbf{x}} \times \hat{\mathbf{y}} = \hat{\mathbf{z}}$.

A shorthand notation for multipole index sums is used:

$$\sum_{n,m} \to \sum_{n=1}^{\infty} \sum_{m=-n}^{m=n} .$$

Standard conventions are used for differential operators : the del operator is represented by ∇.

1.3.1.2 Coordinate systems

There are two main coordinate systems used in this manuscript: the Cartesian (O, x, y, z) and Spherical (O, r, θ, ϕ) systems. The cartesian base coordinates and the spherical base coordinates are related using the standard convention in physics (see figure 1.9). We will also use the spherical base vectors, $\hat{\mathbf{e}_r}$, $\hat{\mathbf{e}_\theta}$ and $\hat{\mathbf{e}_\varphi}$:

$$\begin{aligned} \hat{\mathbf{e}_r} &= \hat{\mathbf{r}} = \sin\theta\cos\varphi\hat{\mathbf{x}} + \sin\theta\sin\varphi\hat{\mathbf{y}} + \cos\theta\hat{\mathbf{z}} \\ \hat{\mathbf{e}_\varphi} &= -\sin\varphi\hat{\mathbf{x}} + \cos\varphi\hat{\mathbf{y}} \\ \hat{\mathbf{e}_\theta} &= \hat{\mathbf{e}_\varphi} \times \hat{\mathbf{e}_r} \end{aligned}$$

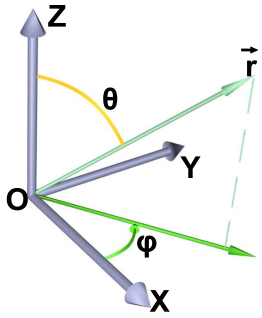

Figure 1.9: The two principal coordinate systems and how they are related : $\theta \in [0, \pi]$ is the polar angle from the (Oz) axis, $\phi \in [0, 2\pi]$ is the azimuth respectively to the (Ox) axis.

1.3.1.3 Particle labels, positions and particle-centered radii

The reference spherical coordinate system is centered on origin O. N is the number of scatterers of the considered system. In the equations, $i \in [1..N]$ is a label that refers to the i-th sphere. The position vector of the i-th sphere is written $\mathbf{u}_i$, and we define a "particle-centered radius", $\mathbf{r}_i \equiv \mathbf{r} - \mathbf{u}_i$ for each of the spheres.

1.3.1.4 Dimensionless quantities

We use normalized (dimensionless) quantities as often as possible. Normalized, dimensionless quantities are generally indicated by a tilde:

- $\widetilde{\alpha}_n^q = \frac{\alpha_n^q}{4\pi a^3}$ is the dimensionless polarizability of multipolar order n and electromagnetic type q
- Q_{scat}, Q_{abs}, Q_{abs} are the scattering, absorption and extinction efficiencies, respectively. They are computed from the corresponding cross-sections σ: $Q = \sigma / \left(\pi \sum_{\text{n=1}}^{N} a_n^2\right)$

- $\widetilde{\Gamma}_{\text{tot}}$, $\widetilde{\Gamma}_{\text{rad}}$, $\widetilde{\Gamma}_{\text{nr}}$ are the normalized total, radiative and non-radiative decay rates respectively. The normalization factor is the reference decay rate, Γ_0: $\widetilde{\Gamma} = \Gamma/\Gamma_0$

1.3.1.5 Harmonic fields

The complex notation for both the electric field and magnetic field is used in order to solve the Maxwell equations, meaning that the physical electric and magnetic fields correspond to the **real** part of their complex counterpart.

A time dependence of the electromagnetic fields in $\exp(-i\omega t)$ is assumed, where ω is the angular frequency. The wavelength in vacuum is written λ. The wavevector in a homogeneous medium of refractive index n_0 has a norm of $k = \frac{2\pi}{\lambda} n_0$. All calculations are related to harmonic fields and we do not consider nonlinear effects.

1.3.2 Multipole expansion of the fields

The multipole expansion of the electromagnetic fields is presented in detail in appendix A. Here we will only give the main equations, for future reference. Any scattered field, $\mathbf{E}_{\text{s}}(\mathbf{r})$, in a homogeneous medium and outside of a circumscribing sphere surrounding the scattering system, can be developed in terms of outgoing partial waves:

$$\mathbf{E}_{\text{s}}(\mathbf{r}) = \sum_{n,m} \left[\mathbf{M}^{\text{out}}_{n,m}(k\mathbf{r})\, f_{q=1,n,m} + \mathbf{N}^{\text{out}}_{n,m}(k\mathbf{r})\, f_{q=2,n,m} \right] , \tag{1.5}$$

where $\mathbf{M}^{\text{out}}_{n,m}$, $\mathbf{N}^{\text{out}}_{n,m}$, are the *outgoing* vector partial waves (VPWs) with outgoing boundary conditions, and the $f_{q,n,m}$ are the complex coefficients of the scattered field in the VPW basis (see appendix A.2).

Any incoming field on a part of the totality of the system, can be expressed in a very similar manner, using VPWs that satisfy incoming boundary conditions instead of outgoing ones (see appendix A.2):

$$\mathbf{E}_0(\mathbf{r}) = \sum_{n,m} \left[\mathbf{M}^{\text{inc}}_{n,m}(k\mathbf{r})\, e_{q=1,n,m} + \mathbf{N}^{\text{inc}}_{n,m}(k\mathbf{r})\, e_{q=2,n,m} \right] \tag{1.6}$$

where the coefficients fo the incoming field are the $e_{q,n,m}$ complex numbers. We henceforth adopt a compact matrix notation where the "scalar product" is a shorthand notation for the sums of VPWs in equations 1.5 and 1.6 (see appendix A.2.1):

$$\begin{aligned} \mathbf{E}_{\text{s}}(\mathbf{r}) &= [\mathbf{MN}]^{\text{out}}(\mathbf{r}) \cdot \mathbf{f} \\ \mathbf{E}_0(\mathbf{r}) &= [\mathbf{MN}]^{\text{inc}}(\mathbf{r}) \cdot \mathbf{e} \end{aligned}$$

1.3.3 Mie-Foldy-Lax Multiple scattering theory

The system under study is an ensemble of spheres, and the incoming electromagnetic field consists of a plane wave, a focused Gaussian beam, or an electric or magnetic dipole placed in the vicinity of the spheres. The system is solved and any physical

parameter (such as local field at a given point, cross sections, emitter's decay rates, radiation diagrams, *etc.*) can be computed. We will first discuss the case of a homogeneous sphere, then the case of an arbitrary, fixed ensemble of spheres.

1.3.3.1 Isolated spheres

Mie solved, in 1908, the scattering problem for a homogeneous sphere [Mie 1908]. We consider a homogeneous spherical particle of radius a, of permittivity ε_s, of permeability μ_s, embedded in a homogeneous background characterized by ε_b and μ_b. The wavevectors in the particle and background medium are $k_s = 2\pi n_s/\lambda$ and $k_b = 2\pi n_b/\lambda$ respectively. The electric (magnetic) coefficient of order n, a_n (b_n) can be cast (see Appendix B.1 for the definition of j_n, h_n, φ_n and $\varphi_n^{(3)}$):

$$a_n = \frac{j_n(ak_b)}{h_n(ak_b)} \frac{\varepsilon_s \varphi_n(ak_b) - \varepsilon_b \varphi_n(ak_s)}{\varepsilon_b \varphi_n(ak_s) - \varepsilon_s \varphi_n^{(3)}(ak_b)} \tag{1.7}$$

$$b_n = \frac{j_n(ak_b)}{h_n(ak_b)} \frac{\mu_s \varphi_n(ak_b) - \mu_b \varphi_n(ak_s)}{\mu_b \varphi_n(ak_s) - \mu_s \varphi_n^{(3)}(ak_b)} \tag{1.8}$$

Let $\mathbf{e}$ and $\mathbf{f}$ be the column matrices containing the incoming and scattered fields' coefficients in the multipolar basis, respectively, expressed at the particle center. In the GMT framework, the scattered field is then given by:

$$\begin{aligned} \mathbf{E}_s(\mathbf{r}) = & \sum_{p=1}^{\infty} \left[\mathbf{M}_p^{\text{out}}(k\mathbf{r}) f_{q=1,p} + \mathbf{N}_p^{\text{out}}(k\mathbf{r}) f_{q=2,p} \right] \\ = & \sum_{p=1}^{\infty} \left[\mathbf{M}_p^{\text{out}}(k\mathbf{r}) b_n e_{q=1,p} + \mathbf{N}_p^{\text{out}}(k\mathbf{r}) a_n e_{q=2,p} \right] \end{aligned}$$

because of the simple link between the incoming and scattered coefficients, namely, $f_{\text{q=1,p}} = b_{\text{n}} e_{\text{q=1,p}}$ and $f_{\text{q=2,p}} = a_{\text{n}} e_{\text{q=2,p}}$ respectively. This relation can be cast in a matrix form:

$$\mathbf{f} = \mathbf{T}\mathbf{e} \tag{1.9}$$

where $\mathbf{T}$ is called the "T-matrix" (which is diagonal in this case). The scattered field at a given point $\mathbf{r}$ outside the scatterer, $\mathbf{E}_{\text{s}}(\mathbf{r})$, can eventually be cast: (see appendix B.2)

$$\mathbf{E}_{\text{s}}(\mathbf{r}) = \quad [\mathbf{MN}]^{\text{out}}(\mathbf{r}) \cdot [\mathbf{T}\ \mathbf{e}] \tag{1.10}$$

The physical parameters of the system can be computed from the value of the total (incoming plus scattered) or scattered fields. See Appendix B.3 for the case of the computation of the field inside a scatterer. We shall now consider the case of multiple spherical scatterers.

1.3.3.2 T-matrix of an ensemble of spheres

When the system under study consists of an ensemble of N scatterers, each scatterer is assigned its own locally "incident" field, $\mathbf{E}_0$, decomposed into the multipole basis,

and the equation system 1.9 becomes a system of $2Np_{\max}$ lines which can still be cast: (see appendix C.2)

$$\mathbf{f} = \mathbf{T}\ \mathbf{e} \equiv \sum_{j=1}^{N} \mathbf{T}. \tag{1.11}$$

where we point out that $\mathbf{f}$ is now a column matrix containing a set of incoming field coefficients *for each scatterer*. $\mathbf{T}$ is now the multiple-particle T-matrix, that is no longer diagonal in the general case – even for homogeneous, identical scatterers. With an appropriate definition of the multiple-particle row-matrix of outgoing VPWs, $[\mathbf{MN}]^{\mathrm{out,N}}(\mathbf{r})$ (see appendix A.2.1), equation 1.10 is formally conserved as well:

$$\mathbf{E}_{\mathrm{s}}(\mathbf{r}) = [\mathbf{MN}]^{\mathrm{out,N}}(\mathbf{r}) \cdot [\mathbf{T}\ \mathbf{e}] \tag{1.12}$$

1.3.4 Figures of merit

In order to compare the performance of different designs, various figures of merit are commonly used throughout this thesis. Most of the time, as stated in section 1.3.1.4, those figures will be dimensionless numbers. Each of them represents a physical property of the designed nanoantenna, and we present them below (see appendix D for full derivations of the cross-sections and decay rates expressions).

1.3.4.1 Scattering and extinction efficiencies

The amount of scattering and absorption of an impeding plane wave by a particle (or ensemble of particles) are traditionally represented by a "cross-section", which has the dimension of an area : it represents a surface, normal to the plane wave's propagation direction, that intercepts the same amount of power as the power that is scattered or absorbed, respectively, by the particle. Extinction is the sum of scattering and absorption. In order to obtain a dimensionless parameter, we divide the cross sections by the geometric cross-section of the system (the sum of the areas of disks having the same diameters as the spheres in the system). We call these quantities scattering and absorption *efficiencies*.

With I_{inc} the radiance of the incoming plane wave, P, σ, Q the scattering/absorption/extinction power, cross section and efficiency, and for an ensemble of N spheres of radius $(a_n)_n$, we have:

$$\sigma = P/I_{\mathrm{inc}}$$
$$Q = \sigma/\left(\pi \sum_{\mathrm{n=1}}^{N} a_n^2\right)$$

See appendix D.1 for a derivation of the scattering and absorption cross-sections expressions in the GMT framework.

1.3.4.2 Decay rates enhancements and quantum efficiency

Appendix D.2 gives the derivation of the formulas that we use for the computation of the decay rates. The quantum efficiency of the emission is the fraction of power that is radiated compared to the total power dissipated at this wavelength. When calculating this energy balance, one should take into account the *initial* quantum efficiency η_0 of the emitter [Bharadwaj 2007]. If the initial emitter is perfect, or if the total decay rate enhancement is large compared to unity, the quantum efficiency reduces to the ratio of the radiated to the total decay rate enhancement, $\tilde{\Gamma}_{\text{rad}}/\tilde{\Gamma}_{\text{tot}}$.

$$\begin{aligned} \tilde{\Gamma}_{\text{tot}} &= \tilde{\Gamma}_{\text{rad}} + \tilde{\Gamma}_{\text{nr}} \\ \eta_{\text{eff}} &= \tilde{\Gamma}_{\text{rad}}/\left[\tilde{\Gamma}_{\text{tot}} + (1-\eta_0)/\eta_0\right] \\ \eta_{\text{eff}} &= \eta \equiv \tilde{\Gamma}_{\text{rad}}/\tilde{\Gamma}_{\text{tot}} \quad (\eta_0 = 1 \text{ or } \tilde{\Gamma}_{\text{tot}} \gg 1) \end{aligned}$$

1.3.4.3 (Normalized) Radiation diagrams

The shape of the radiation diagram is also modified by the emitter's electromagnetic environment. For more reliable radiation diagrams comparison, we always adopt the same normalization: 1 corresponds to the maximum radiant intensity achieved in the embedding dielectric matrix. In order to be able to perceive more details, some of the radiation diagrams will be drawn with a logarithmic scale (1 on natural scale equals 0 dB).

1.3.4.4 Directivity of the emission

In order to characterize the emission directivity, we use a figure of merit that comes from radio-wave antennas : the isotropic decibel (dBi). It represents the gain, in dB, of the maximal radiant intensity over the intensity of an isotropic source with the same total radiative power,

$$D_{\text{dBi}} = 10\log(4\pi P/\Gamma_{\text{rad}}) \tag{1.13}$$

where P is the power per steradian emitted in the direction of interest and Γ_{rad} is the total radiative power of the antenna.

1.3.4.5 Fluorescence Enhancement

Fluorescence enhancement is a major topic of nanoantennas. We consider the simple case of a three-level molecule, with one exciting wavelength and one (different) fluorescence emission wavelength, plus one non-radiative decay channel (see figure 1.6). We assume that the fluorescence signal, produced by molecules in solution, is collected by a microscope setup and reaches a photodiode. The photocurrent, I_{fluo} is thus the measured signal, and we assume it can be expressed in a general form:

$$I_{\text{fluo}} = \kappa \sum_{i \in M} K_{\text{coll}}(i)\Gamma_{\text{eff}}(i)$$

where:

- κ is the photon-to-current conversion efficiency of the setup
- M is the ensemble of the excited fluorescent molecules
- $K_{\text{coll}}(i)$ is the collection efficiency of the setup for the photons cast by the molecule labeled i
- $\Gamma_{\text{eff}}(i)$ is the photon emission rate of the molecule labeled i

The fluorescence enhancement factor is defined by the ratio:

$$F_{\text{enh}} = I_{\text{fluo}}/I_{\text{ref}}$$

where I_{ref} is a reference sample with the same experimental setup and excitation characteristics as the studied sample, typically a sample where the nanoantenna structure is absent. F_{enh} thus represents the signal enhancement provided by the nanoantenna structure.

In this section we present the principal mechanics of fluorescence enhancement. In order to introduce this concept in a simple way, we will consider a *nondispersive sample*, which consists of identical emitters (in terms of decay rates, excitation cross-sections and quantum efficiencies) that allow ensemble averages, and a *continuous wave excitation*. There are two main excitation regimes, the linear (low-power) and saturation (high-power) regimes. In the low-power excitation regime, the fluorescent molecule is able to release a photon, or deexcite non-radiatively, before another incoming photon is avaiable to excite it again. The rate of the molecule's photon emission is then proportionnal to the incoming power (*i.e.* incoming photons per unit of time), hence the name of "linear excitation regime". When the input power increases, the emitted power gradually tends towards a saturation regime, where the molecule is excited again as soon as it reaches the ground level. The maximal emitted power is then limited by the rate at which the molecule deexcites to the ground state once it is excited by an incoming photon.

Linear excitation regime : In the linear excitation regime, the photon emission rate is proportionnal to the excitation intensity, and the photocurrent can be expressed [Aouani 2011]:

$$I_{\text{lin}}(t) = \kappa \int_{Veff} I_{\text{exc}}(\mathbf{r}) K_{\text{coll}}(\mathbf{r}) C(\mathbf{r}) \sigma\eta \; d^3\mathbf{r}$$

where:

- $Veff$ is the effective volume that is excited
- I_{exc} is the excitation intensity at the excitation wavelength
- C is the concentration of the fluorescent molecule in the solution

- σ is the absorption cross-section of the molecule
- η is the effective quantum efficiency of the molecule

Thus we can cast, in the hypothesis that σ and C are the same between the studied and the reference samples:

$$F_{\text{enh}} = \frac{\int_{Veff} I_{\text{exc}}(\mathbf{r}) K_{\text{coll}}(\mathbf{r}) \eta \; d^3\mathbf{r}}{\int_{Veff} I_{\text{exc},0}(\mathbf{r}) K_{\text{coll},0}(\mathbf{r}) \eta_0 \; d^3\mathbf{r}}$$

Therefore, in this regime, the excitation intensity (which depends on both the microscope setup, and on the nanoantenna structure, provided there is one in the excited volume) is the main parameter which can increase the observed signal. This regime is thus particularly adapted to probe the excitation intensity of a given setup, and compare the excitation intensity enhancements of several setups, but it does not provide the highest output photon count rates. The other important parameters are the effective quantum efficiency η, which can be greatly modified by the antenna structure, and the collection efficiency K_{coll}, which can be controlled as well *via* a modification of the radiation diagram of the molecules.

Saturation regime : In the saturation regime, the fluorescent molecule has the highest possible output photon count rate, which is limited by its decay rate: it cannot emit a photon faster than its decay time. The photocurrent is written: [Aouani 2011]

$$I_{\text{sat}}(t) = \kappa \int_{Veff} K_{\text{coll}}(\mathbf{r}) C(\mathbf{r}) \Gamma_{\text{tot}} \eta \; d^3\mathbf{r}$$

Thus with the same hypothesis as in the linear excitation regime, we can cast:

$$F_{\text{enh}} = \frac{\int_{Veff} K_{\text{coll}}(\mathbf{r}) \Gamma_{\text{tot}} \eta \; d^3\mathbf{r}}{\int_{Veff} K_{\text{coll},0}(\mathbf{r}) \Gamma_{\text{tot},0} \eta_0 \; d^3\mathbf{r}}$$

In this regime, the main parameter is thus the decay rate enhancement provided by the nanoantenna structure. The collection efficiency and quantum efficiency still play the same role as in the linear excitation regime. This regime is thus adapted to probe the decay rate enhancements of different structures, and it provides the highest signal levels.

Chapter 2

From Light to Matter (elastic scattering, absorption)

"Light thinks it travels faster than anything but it is wrong. No matter how fast light travels, it finds the darkness has always got there first, and is waiting for it."
Terry Pratchett, English writer (1948–)

Contents

In this chapter, we will consider the case of a far-field illumination of the antenna structure. Even when the particle size is non negligible compared to the wavelength, an electric dipole-dipole coupling model with full retardation effects can give accurate results provided the multipole contribution in the structure are not too strong. Such a model is presented in section 2.1. This electric dipole model can easily be extended in order to take into account the magnetic induced dipole resonances of dielectric particles and of metallic structures like split ring resonators (SRRs); however, in this case the breaking of the central symmetry has a number of consequences. Some of those consequences, in the case of a SRR-shaped metallic resonator, are presented in section 2.2. Dipole coupling models help to better understand the physics underlying the behavior of coupled and isolated resonators alike, but some care must be taken when considering strongly coupled systems. The one-dimensionnal array of particles is a canonical example of a strongly coupled system, since multipoles can participate in the array coupling, even for separations between particle surfaces the order of the radius, as shown in section 2.3.

2.1 Effective polarizability of a metallic dimer

2.1.1 Full dynamics electric dipole-dipole coupling model for far-field illuminations

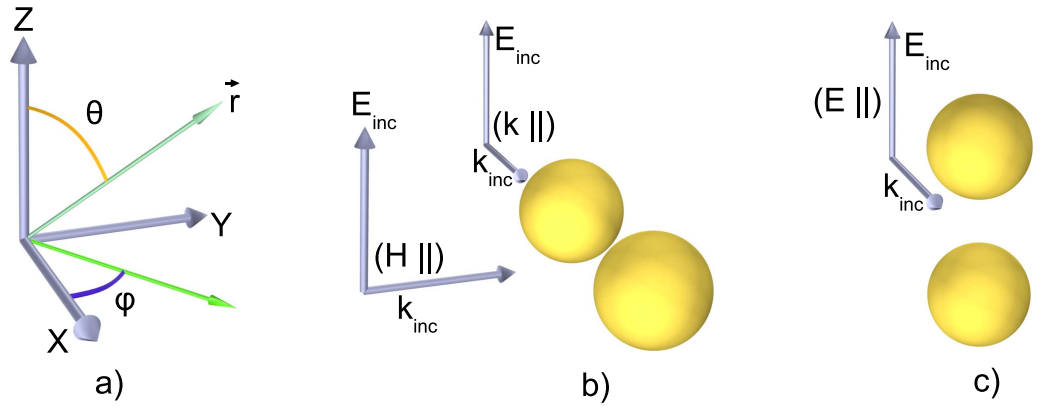

Figure 2.1: (a) Definition of the spherical coordinates; dimer illumination schematics for: (b) Transverse illuminations, and (c) Longitudinal illumination.

We consider the case of two electric dipole resonators coupled together and arbitrarily labeled 1 and 2. The general case of oblique incidences, non-scalar polarizabilities and/or distinct resonators can be treated with equations quite similar to those presented below, when adopting an adequate GMT formulation of the problem. We will consider the mathematically simpler case of two identical scatterers (the structure is henceforth called a dimer) with scalar polarizabilities, and three main cases of far-field illumination: incoming wavevector parallel to the dimer axis (which we name $k_{\|}$), and incoming wavevector perpendicular to the dimer axis, with the electric field ($E_{\|}$) or magnetic field ($H_{\|}$) parallel to the dimer axis. The resonators are separated by a center-to-center distance d. The coupling between the two resonators results in the multiple-scattering system of equations:

$$\mathbf{E}_{\text{exc}}^{(1)} = \mathbf{E}_{\text{inc}}^{(1)} + \mathbf{E}_{\text{scat}}^{2\to1}, \tag{2.1}$$

$$\mathbf{E}_{\text{exc}}^{(2)} = \mathbf{E}_{\text{inc}}^{(2)} + \mathbf{E}_{\text{scat}}^{1\to2}, \tag{2.2}$$

where $\mathbf{E}_{\text{inc}}$ is the incoming field, $\mathbf{E}_{\text{scat}}^{i\to j}$ is the field scattered by resonator i at the position of resonator j, and $E_{\text{exc}}^{(j)}$ is the exciting electric field associated with the particle j. Due to the symmetries, when the illumination is ($k_{\|}$), or ($H_{\|}$), both induced electric dipoles are transverse (T) to the dimer axis; and when the illumination is ($E_{\|}$), the induced dipoles are longitudinal (L) to the dimer axis. In both transverse cases, the coupling is itself identical, but in the $E_{\|}$ case the incoming fields are identical whereas in the $k_{\|}$ case they are out of phase because of the propagation on the distance d between the resonators. We thus place the two particles along

either the $\hat{\mathbf{x}}$-axis or the $\hat{\mathbf{z}}$-axis depending on the studied illumination conditions (see fig. 2.1). The particle orientations were chosen so that the incident electric field can be conveniently taken to lie along the $\hat{\mathbf{z}}$ axis throughout this study, *i.e.*:

$$\begin{aligned}\mathbf{E}_{\mathrm{inc,E}\parallel}(x) &= \mathbf{E}_{\mathrm{inc,k}\parallel}(x) = E_0\hat{\mathbf{z}}e^{ikx},\\ \mathbf{E}_{\mathrm{inc,H}\parallel}(y) &= E_0\hat{\mathbf{z}}e^{iky},\end{aligned} \tag{2.3}$$

where $k = (\omega/c)n_b$ is the wavenumber of the incoming plane wave in the background environment (refractive index n_b). The induced dipole moments of each particle are thus also aligned along the $\hat{\mathbf{z}}$-axis, and can be expressed:

$$\mathbf{p}^{(j)}(\omega) = \varepsilon_0\varepsilon_b\alpha(\omega)E^{(j)}_{\mathrm{exc}}(\omega)\hat{\mathbf{z}}. \tag{2.4}$$

We introduce an effective polarizability approach [Markel 1993, Gozhenko 2003, Pinchuk 2005, Khlebtsov 2006] wherein the multiple scattering phenomena occurring between the two spheres is assimilated into an "effective" polarizability (the term "dressed polarizability" is also used [Albella 2013]). The electric field produced by the electric dipole moment $\mathbf{p}^{(j)}$ can be expressed (from equation **??**):

$$\mathbf{E}^{(j)}_{\mathrm{scat}}(\mathbf{r}) = \frac{e^{ikr}}{4\pi\varepsilon_b\varepsilon_0 r^3}\left\{k^2r^2(\hat{\mathbf{r}}\times\mathbf{p}^{(j)})\times\hat{\mathbf{r}} + (1-ikr)\left[3(\hat{\mathbf{r}}\cdot\mathbf{p}^{(j)})\hat{\mathbf{r}} - \mathbf{p}^{(j)}\right]\right\}. \tag{2.5}$$

The excitation fields for spheres 1 and 2 can thus be written: (see demonstration in appendix E.1.1):

$$E^{(1)}_{\mathrm{exc}} = E^{(1)}_{\mathrm{inc}} + \gamma E^{(2)}_{\mathrm{exc}}, \tag{2.6a}$$

$$E^{(2)}_{\mathrm{exc}} = E^{(2)}_{\mathrm{inc}} + \gamma E^{(1)}_{\mathrm{exc}}, \tag{2.6b}$$

where γ is a coupling factor between the two induced dipoles:

$$\begin{aligned}\gamma_{\mathrm{T}} = \gamma_{\mathrm{k}\parallel} &= \gamma_{\mathrm{H}\parallel}\\ &\equiv e^{ikd}\frac{\alpha}{4\pi d^3}(k^2d^2 + ikd - 1),\end{aligned} \tag{2.7a}$$

$$\gamma_L \equiv \gamma_{\mathrm{E}\parallel} \equiv e^{ikd}\frac{\alpha}{2\pi d^3}(1-ikd). \tag{2.7b}$$

We remark in these expressions of the coupling factors, γ, that the propagation term e^{ikd}, is only *partly* responsible for the phase of the coupling factor, and we can readily surmise that the respective factors $(k^2d^2 + ikd - 1)$ and $(1 - ikd)$ play non-negligible roles, particularly at distances that are small or comparable to the wavelength.

The solution to the system of coupled equations (eqs. (2.6a) and (2.6b)), can be expressed in terms of the following effective polarizabilities (see demonstration in

appendix E.1.1): [Rolly 2011b]

$$\alpha^{(1)}_{\text{eff,k}\parallel} = \alpha \frac{1+\gamma_{\text{T}} e^{ikd}}{1-\gamma_{\text{T}}^2}, \tag{2.8a}$$

$$\alpha^{(2)}_{\text{eff,k}\parallel} = \alpha \frac{1+\gamma_{\text{T}}\, e^{-ikd}}{1-\gamma_{\text{T}}^2}, \tag{2.8b}$$

$$\alpha^{(1)}_{\text{eff,H}\parallel} = \alpha^{(2)}_{\text{eff,H}\parallel} = \frac{\alpha}{1-\gamma_{\text{T}}}, \tag{2.8c}$$

$$\alpha^{(1)}_{\text{eff,E}\parallel} = \alpha^{(2)}_{\text{eff,E}\parallel} = \frac{\alpha}{1-\gamma_{\text{L}}}, \tag{2.8d}$$

which express the induced dipole moment of each particle directly in terms of the incident field on that particle, *i.e.*:

$$\mathbf{p}^{(j)}(\omega) = \varepsilon_0 \varepsilon_b \alpha^{(j)}_{\text{eff}}(\omega) E^{(j)}_{\text{inc}}(\omega)\hat{\mathbf{z}}. \tag{2.9}$$

The effective polarizabilities are thus proportional to the single particle polarizability, and to a term involving the inter-particle coupling γ. We can cast the relative phase, ϕ, between the two induced dipoles in the $k_\parallel$ case:

$$\phi = \arg(p_2/p_1) = \arg(e^{ikd}\frac{1+\gamma_{\text{T}} e^{-ikd}}{1+\gamma_{\text{T}} e^{ikd}}). \tag{2.10}$$

Once the induced dipole moments are known, one can calculate the scattered electromagnetic fields and infer any physical parameter of the scattering process. We consider below, the scattering cross-sections of a sub-wavelength metallic dimer under the three different illuminations presented here.

2.1.2 Results on large subwavelength metallic dimers

When considering the cross sections of a dimer of metallic particles with sizes and gaps much smaller than the wavelength (*i.e.* total maximal size $< \lambda/10$), one can easily apply the plasmon hybridization model [Nordlander 2004]. This model predicts that the "brightest" mode (the one which scatters the most power) will appear when the polarization of the incident beam is longitudinal to the dimer and the induced dipoles are in phase ; on the other hand, when the dipoles are in opposite-phase, applying a quasi-static model results in a reduction of the net dipole moment, which leads to a "dark" mode (which scatters little light).

This model is very elegant, and, when we consider small particles (around 20 nm diameter in optics), quite accurate. But some authors tend to use the terminology of "bright" or "dark" modes for much larger particles, when the quasi-static approximation is no longer valid [Yang 2010]. In the following, we will demonstrate that when the quasi-static approximation fails, under certain circumstances, the brightest mode of a dimer may only occur, not when the incident polarization of light is longitudinal to the dimer and the induced dipoles are in-phase, but rather when the polarization is transverse and the induced dipoles out-of-phase (or even in opposite-phase).

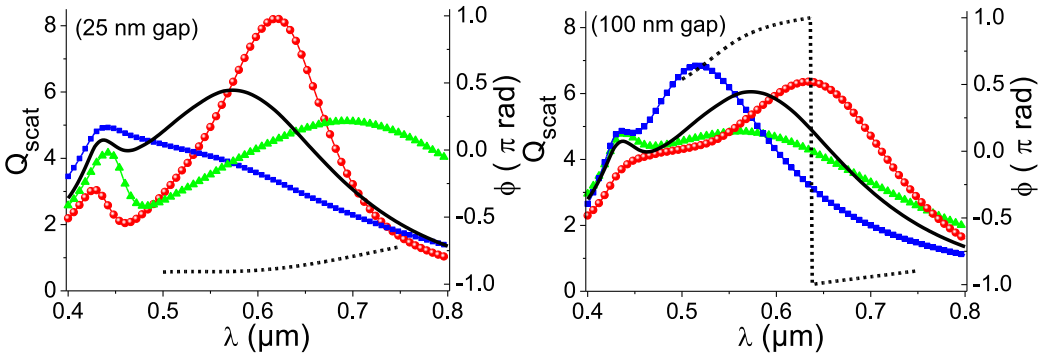

Figure 2.2: Scattering properties of a dimer of silver particles, $D = 110$ nm in diameter with respective nanogap sizes, $(d - D)$, of (left) 25nm and (right) 100 nm. The dimer is embedded in a matrix of refractive index $n_b = 1.5$. (full lines and symbols, left scale) Scattering efficiencies *per particle*, $Q_{\rm scat} \equiv \sigma_{\rm scat}/(2\pi a^2)$: (full black circles) $k_{\|}$, and (blue squares) $H_{\|}$, (green triangles) $E_{\|}$ illumination, (full lines) values for the monomer $(\sigma_{\rm scat}/(\pi a^2))$. (dashed black line, right scale) Relative phase of the induced dipoles, for the $k_{\|}$ illumination.

We consider a dimer of silver spherical particles (radius $a = 55$ nm, permittivity extrapolated from experimental values of Palik and Ghosh [Palik 1998]) in a polymer-like environment of refractive index $n_b = 1.5$. The generalized Mie theory is implemented in order to accurately calculate both the scattering cross-section and the electric field at the center of each metallic particle. We plot the relative phase of the two induced dipoles (for the $k_{\|}$ illumination) as a function of the incident wavelength together with the scattering cross-section of the dimer (fig. 2.2). We focus attention on wavelengths between 500 nm and 750 nm, where all dipole phenomena occur for the studied dimer. Hence the features of the cross-sections around $\lambda = 425$ nm, that are of multipolar nature (quadrupolar for the most part), will not be described here.

Symmetry dictates identical phases for the induced dipoles of a dimer in both $E_{\|}$ and $H_{\|}$ illuminations, but phase differences are important for a $k_{\|}$ illumination. It is noteworthy to remark that for the latter illumination, and nanogaps much smaller than the incident wavelength (like both 25 nm and 100 nm cases), the maximum of the scattering cross-section does not correspond to in-phase dipoles, but rather to strongly out-of-phase ones. In the case of a 100 nm nanogap, the two induced dipoles are even in opposite relative phase at the scattering cross-section maximum. Moreover, the nearly opposite phase mode observed for the 25 nm nanogap has a larger scattering efficiency than the in-phase mode observed for both other illuminations. Those counter-intuitive results can be explained with the help of the dipole-dipole coupling model derived in the previous section.

Indeed, using this model, we can show that the scattering cross sections of such a dimer of dipolar particles are closely linked to the square modulus of the effective po-

larizabilities, in a manner similar to the scattering efficiency of a monomer, which is directly proportional to the square modulus of its polarizability: (see demonstration in appendix E.1.2)

$$\begin{aligned}\sigma_{\mathrm{scat},k\parallel} = \frac{k^4}{6\pi}\Bigg[&\left|\alpha^{(1)}_{\mathrm{eff,k}\parallel}\right|^2 + \left|\alpha^{(2)}_{\mathrm{eff,k}\parallel}\right|^2 \\ &+ 2\Re(\alpha^{(1)}_{\mathrm{eff,k}\parallel}(\alpha^{(2)}_{\mathrm{eff,k}\parallel})^* e^{-ikd})\mathrm{A_T}\Bigg],\end{aligned} \tag{2.11a}$$

$$\sigma_{\mathrm{scat},H\parallel} = \frac{k^4}{3\pi}|\alpha_{\mathrm{eff,H}\parallel}|^2\Big(1+\mathrm{A_T}\Big), \tag{2.11b}$$

$$\sigma_{\mathrm{scat},E\parallel} = \frac{k^4}{3\pi}|\alpha_{\mathrm{eff,E}\parallel}|^2\Big(1+\mathrm{A_L}\Big), \tag{2.11c}$$

where the factors $\mathrm{A_{T,L}}$ are respectively defined to contain the radiative interference effects:

$$\begin{aligned}\mathrm{A_T} &\equiv 3\frac{(k^2d^2-1)\sin(kd)+kd\cos(kd)}{2(kd)^3}, \\ \mathrm{A_L} &\equiv 3\frac{\sin(kd)-kd\cos(kd)}{(kd)^3}.\end{aligned} \tag{2.12}$$

The radiative interference terms, $\mathrm{A_{T,L}}$, can both be replaced by 1 in the limit of $kd \to 0$ (to the 3rd order in kd), and decrease only slowly with increasing kd. Consequently, their kd dependence can be safely ignored during this study.

The normalized *per sphere* scattering efficiencies, Q_{scat} are plotted in fig. 2.3 for all three illuminations as functions of λ and d using both the above analytic model and full electromagnetic calculations (generalized Mie theory with $n_{max} = 20$ maximum multipole order). The monomer resonance frequency is indicated in all graphs by a dashed white line. One can see that the analytic dipole formalism remarkably predicts that: (i) transverse couplings can produce larger scattering cross-sections than longitudinal couplings and that, (ii) for in-phase dipoles modes ($E_\parallel$ and $H_\parallel$ illuminations), the maxima are not obtained when the separation is minimal ($d - D \to 0$), but rather for separations of $d = 450$nm and $d = 300$nm respectively.

If we neglect the influence of the numerator in eqs. (2.8a) and (2.8b), and define $\mathrm{K_T} \equiv |\gamma_\mathrm{T}|$, $\mathrm{K_L} \equiv |\gamma_L|$, $\Theta_\mathrm{T} \equiv \arg(\gamma_\mathrm{T})$ and $\Theta_\mathrm{L} \equiv \arg(\gamma_\mathrm{L})$, we deduce from eqs. (2.8a)

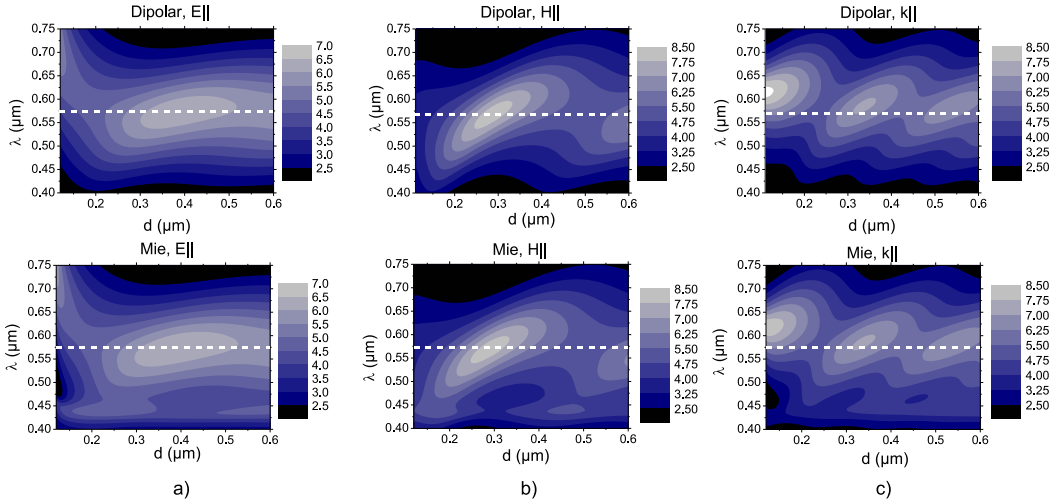

Figure 2.3: (top row) Scattering efficiency calculated with the dipolar model, versus the center-to-center separation, d (abscissa), and the vacuum wavelength, λ (ordinate), for a dimer of silver spherical particles 110 nm in diameter. (a) $E_{\parallel}$ illumination, (b) $H_{\parallel}$ illumination and (c) $k_{\parallel}$ illumination. Bottow row : same plots using the generalized Mie theory.

to (2.8d):

$$\begin{aligned}
\left|\alpha_{\mathrm{eff},k\parallel}\right|^2 &\cong \frac{|\alpha|^2}{\left|1-(\mathrm{K_T}\, e^{i\Theta_\mathrm{T}})^2\right|^2} \\
&= \frac{|\alpha|^2}{1+\mathrm{K_T^4}-2\mathrm{K_T^2}\cos(2\Theta_\mathrm{T})}, \qquad (2.13a)\\
\left|\alpha_{\mathrm{eff},H\parallel}\right|^2 &= \frac{|\alpha|^2}{|1-\mathrm{K_T}\, e^{i\Theta_\mathrm{T}}|^2} \\
&= \frac{|\alpha|^2}{1+\mathrm{K_T^2}-2\mathrm{K_T}\cos\Theta_\mathrm{T}}, \qquad (2.13b)\\
\left|\alpha_{\mathrm{eff},E\parallel}\right|^2 &= \frac{|\alpha|^2}{|1-\mathrm{K_L} e^{i\Theta_\mathrm{L}}|^2} \\
&= \frac{|\alpha|^2}{1+\mathrm{K_L^2}-2\mathrm{K_L}\cos\Theta_\mathrm{L}}. \qquad (2.13c)
\end{aligned}$$

This set of equations can predict which nanogap separations and wavelengths produce scattering efficiencies maxima. We cast the 'resonant' values, Θ_R, of the coupling phase (i.e. that minimize the respective denominators in eqs. (2.13a) to (2.13c):

$$\Theta_{\mathrm{R},k\parallel} = 0[2\pi] \text{ or } \pi[2\pi], \tag{2.14a}$$
$$\Theta_{\mathrm{R},H\parallel} = 0[2\pi], \tag{2.14b}$$
$$\Theta_{\mathrm{R},E\parallel} = 0[2\pi]. \tag{2.14c}$$

The effect of the inter-particle scattering term in the coupling of two particle resonators has been neglected in some previous works since the involved distances are much smaller than the incident wavelength, but the terms $k^2d^2 + ikd - 1$ and $1 - ikd$ in eqs. (2.7a) and (2.7b) are of fundamental importance in order to explain the counter-intuitive results of figure 2.3. From eqs. (2.7a) and (2.7b) the phase of the polarizabilities of the isolated particles can be expressed:

$$\arg(\alpha) = \Theta_{\mathrm{T}} - kd - \arg(k^2d^2 + ikd - 1), \tag{2.15a}$$
$$\arg(\alpha) = \Theta_{\mathrm{L}} - kd - \arg(1 - ikd). \tag{2.15b}$$

As we see in eq. (2.13), the effective polarizabilities, which are directly linked to the scattering efficiencies, are proportional to both the polarizability of the monomer α, and to a denominator whose resonance conditions are given in eq. (2.14). For a passive particle (the material is not a gain medium), the possible values of the argument of the polarizability lies between 0 and π (α has a positive imaginary part). The resonance of the polarizability of the monomer under study (see inset in fig. 2.4) occurs at a vacuum wavelength $\lambda_0 = 575\mathrm{nm}$, and at this wavelength the argument of the polarizability has a value $\approx 0.42\pi$, close to the quasi-static predicted value of $\pi/2$. For wavelengths blue-shifted from this resonance, the argument increases toward π, and reciprocally it decreases to 0 for red-shifted wavelengths.

There is no direct link between the particle polarizability resonances and that of the coupling. Hence, usually the resonance of the scattering efficiencies will consist in a compromise between the (monomer) polarizability resonance and the coupling resonance factor. In order to illustrate this, let us plot (fig. 2.4) the evolution of $\arg(\alpha)$ as a function of kd (using eq. (2.15)) required so that $\Theta = \Theta_{\mathrm{R}}$ as defined in equation 2.14. This figure is of fundamental importance for the understanding of the aforementioned results: it represents the argument that the polarizability *should* have in order to obtain a resonance of the coupling term, for a given distance parameter kd.

We first look at in-phase modes using the quasi-static approximation, *i.e.* $kd \to 0$. We remark that the redshift of the (longitudinal) bonding mode and the blueshift of the (transverse) anti-bonding modes (correctly predicted by the hybridization model) are also described by the non quasi-static model presented in this study. Maximizing the scattering couplings in the $kd \to 0$ limit requires a polarizability phase tending towards zero for the longitudinal (bonding) mode and π for the transverse (anti-bonding) mode. While both those conditions cannot be achieved simultaneously at a polarizability resonance (which requires $\arg(\alpha) \approx \pi/2$), a compromise between the coupling resonance and the polarizability of the monomer

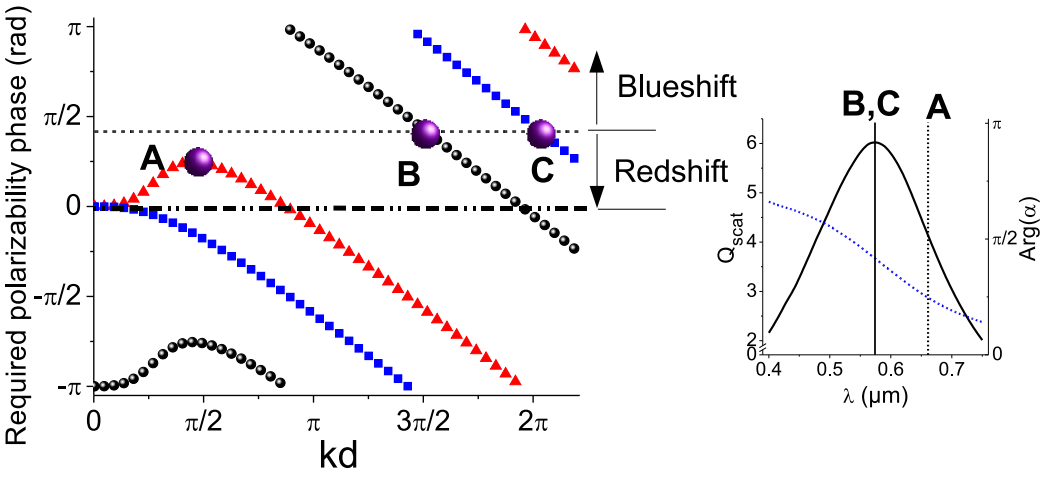

Figure 2.4: (left) Phase of the polarizability fulfilling the respective coupled resonance conditions : $k_{\|}$ illumination (red triangles), $H_{\|}$ and $k_{\|}$ illuminations (black circles), and $E_{\|}$ illumination (blue squares). (right inset) Scattering efficiency (solid black line, left scale) and phase of the polarizability (dashed blue line, right scale) of a $2a = 110$nm silver sphere embedded in a dielectric medium of refractive index $n_m = 1.5$. Vertical lines are plotted for a phase equal to that of point A (dashed line) and points B and C (full line) in the left figure.

results in a shift of the resonance toward red (bonding) or blue (anti-bonding) wavelengths respectively, compared to the resonance of the monomer.

For the more dephased excitations obtained with a $k_{\|}$ illumination, a study of point A in fig. 2.4 shows that the coupling term can be optimized near $kd = \sqrt{2} \approx \pi/2$, i.e. near the contact situation (contact being described at $\lambda \cong 615$nm by $kd \approx 1.68 \approx \pi/2$), if the polarizability phase is $\approx \pi/4$ (which implies a redshift compared to the monomer resonance). From the inset, we can see that the polarizability amplitude at this phase remains non-negligible. As predicted, we do remark in fig. 2.3 a red-shifted resonance under the $k_{\|}$ illumination. In general, the scattering efficiency of the $k_{\|}$ configuration is expected to produce local maxima when either the black or red curves in fig. 2.4 pass through the dotted line because the polarizability and the coupling are thus simultaneously optimized. Counting the point **A** as the first local maxima we can see that this condition is satisfied with a period of approximately π respectively to kd, which explains the $\lambda/2$ periodicity of the scattering efficiency maxima in fig. 2.3.

Similar considerations also predict that the $H_{\|}$ and $E_{\|}$ illuminations will be brightest respectively around $kd \approx 3\pi/2$, and $kd \approx 2\pi$ (points **B** and **C**). In these respective cases, when kd increases, the required $\arg(\alpha)$ for a resonant coupling will vary from π to 0, inducing blue then redshifts of the scattering efficiency maximum when kd increases around its optimum value. Let us recall that the coupling term is rapidly decreasing with respect to d (see eqs. (2.7a) and (2.7b)) so that its influence

on the wavelength of the scattering efficiency maximum will be small when compared to the resonant polarizability of the particles. The values we obtained in fig. 2.3 ($\lambda \cong$ 569nm, $d \cong$ 290nm, i.e. $kd \cong 1.53\pi$ for the $H_{\|}$ illumination, and $\lambda \cong$ 571nm, $d \cong$ 387nm, i.e. $kd \cong 2.03\pi$ for the $E_{\|}$ illumination) agree with these predictions. The dimer illuminated upon the $H_{\|}$ and $E_{\|}$ illuminations will be brightest when black and blue lines respectively will cross the 0.42π ordinate, explaining the twice larger periodicity of the scattering efficiency observed in fig. 2.3.a-b than that observed in fig. 2.3.c for the $k_{\|}$ illumination.

The dipole coupling model we derived in this section is accurate and helps to comprehend some complex coupling phenomena, but it needs to be extended if one wants to treat dielectric particles, for instance, or specially designed metallic structures like split ring resonators, for which the magnetic induced dipoles must be taken into account. The model can be extended to electric and magnetic dipoles with ease [Rolly 2012c]. There is a supplemental degree of complexity of the equations, though, especially when considering scatterers that are non-centrosymmetric, because in most cases their polarizability is not a scalar.

As a matter of fact, we will see in the next section that, even when the sizes of the resonators are less than a tenth of the wavelength, the central symmetry breaking in shapes like split ring resonators give rise to corrections that are required in order to accurately compute the induced electric and magnetic dipole moments.

2.2 Geometry effects illustrated on a SRR geometry

In this section, we will treat the case of a metallic resonator that exhibits a substantial magnetic dipole resonance. This type of resonance is highly desirated for a number of applications, in meta-materials [Sersic 2009] and in near-field spectroscopy [Noginova 2008] for instance. In order for metallic particles to exhibit such resonances, they require to have non-spherical shapes. We consider in particular the well-know split ring resonator (SRR) shape, and discuss the effects of "breaking" the spherical geometry on the dipole polarizability tensor of the scatterer.

2.2.1 Some central symmetry breaking effects

Thanks to their central symmetry, the T-matrices of spherically-symmetric scatterers are diagonal in p, which implies that the only way to excite the $\mathbf{N}^{\text{out}}_{n_0,m_0}$ outgoing Vector Partial Wave (see appendix A.2) from the particle, is to have a nonzero f_{e,n_0,m_0} exciting field on the particle, for the same multipole expansion numbers n_0 and m_0. Subsequently, the coupling between electric and magnetic resonances of the scatterer is not possible.

When the central symmetry is broken, however, the T-matrix of the scatterer is no longer diagonal. One may then excite, for instance, an electric dipole moment on the $\hat{\mathbf{z}}$ axis, $\mathbf{p}_z \neq 0$, even though the incident field is null on the same axis, $\mathbf{E}_{\text{inc}} \cdot \hat{\mathbf{z}} = 0$. This dipole moment $\mathbf{p}_z$ can be induced by a coupling with either the incident electric field on the other Cartesian axes, or with the incident magnetic

field, or even both at the same time. A simple example using a dielectric dimer of nonzero electric and magnetic polarizability is illustrated in figure 2.5.

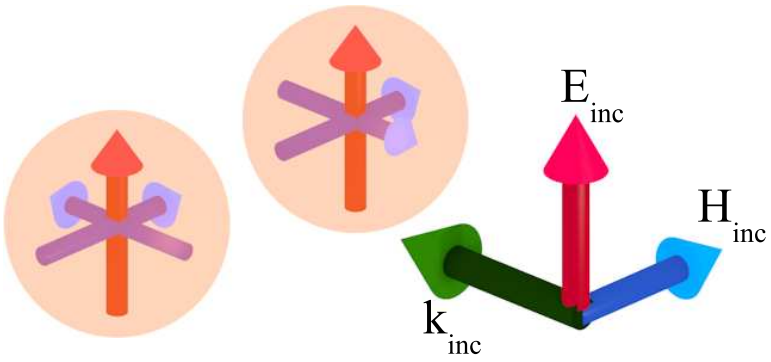

Figure 2.5: A dielectric dimer is illuminated by a plane wave, with incident magnetic field parallel to its axis. The plane wave excites induced dipoles of the same type and on the same axes as the incident fields in each of the spheres, and a third induced dipole, of magnetic nature, appears as well in each sphere (in the same direction as k_{inc}): it is excited by the magnetic field coming from the transverse electric induced dipoles (in red). As can be deduced from the symmetries of the system, those induced dipoles are in opposite relative phase.

Consequently, the polarizability tensor $\bar{\bar{\alpha}}$ of an (electric and magnetic) isolated dipole resonator illuminated by an electromagnetic field ($\mathbf{E}^0$,$\mathbf{H}^0$) is generally cast [Lindell 1994, Varault 2013]:

$$\begin{bmatrix} \mathbf{p} \\ \mathbf{m} \end{bmatrix} = \underbrace{\begin{bmatrix} \bar{\bar{\alpha}}^{ee} & \bar{\bar{\alpha}}^{em} \\ \bar{\bar{\alpha}}^{me} & \bar{\bar{\alpha}}^{mm} \end{bmatrix}}_{\bar{\bar{\alpha}}} \begin{bmatrix} \mathbf{E}^0 \\ \mathbf{H}^0 \end{bmatrix} \tag{2.16}$$

where $\bar{\bar{\alpha}}^{ee}$ and $\bar{\bar{\alpha}}^{mm}$ describe direct electric and magnetic effects while $\bar{\bar{\alpha}}^{em}$ and $\bar{\bar{\alpha}}^{me}$ refer to the electro-magnetic and magneto-electric coupling polarizability tensors.

2.2.2 Model for the dipole moments induced by a plane wave

Equation (2.16) predicts a linear dependence on the local incident field components, a property which is true when moments of a given angular momentum order are only induced by excitation fields of the same order. This situation is usually satisfied for highly symmetric particles, but proves questionable in full multipolar theory for particles of arbitrary form, wherein spatial derivatives of the excitation field can also contribute to the dipolar responses through [Mazur 1953, Raab 2005]:

$$\begin{aligned} p_i &= \alpha_{ij}^{ee} E_j^0 + a_{ijk} \nabla_k E_j^0 + \alpha_{ij}^{em} H_j^0 + b_{ijk} \nabla_k H_j^0 + \cdots \\ m_i &= \alpha_{ij}^{me} E_j^0 + c_{ijk} \nabla_k E_j^0 + \alpha_{ij}^{mm} H_j^0 + d_{ijk} \nabla_k H_j^0 + \cdots \end{aligned} \tag{2.17}$$

where each subscript i, j, and k corresponds to one space coordinate x, y , or z, and where the dipolar (resp. quadrupolar) coupling terms are given by the tensors $\bar{\bar{\alpha}}^{ee}$, $\bar{\bar{\alpha}}^{mm}$, $\bar{\bar{\alpha}}^{em}$, and $\bar{\bar{\alpha}}^{me}$ (resp. $\bar{\bar{a}}$, $\bar{\bar{b}}$,$\bar{\bar{c}}$, and $\bar{\bar{d}}$). Equation (2.17) introduces a dependence on the wavevector orientation appearing along any non-symmetric direction of the particle or nano-cluster. In terms of the T-matrix coefficients of the SRR, these effects are traduced by nonzero non-diagonal terms, $t_{p_1,p_2} \neq 0$ with $p_1 \neq p_2$.

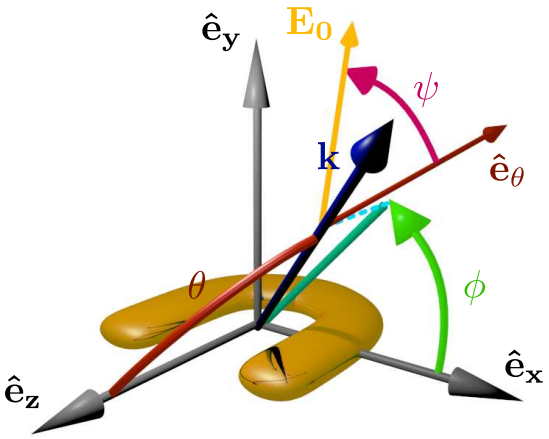

Figure 2.6: Schematic of the studied U-shaped resonator and definition of the referential cartesian coordinate system. The U-shaped resonator is made of gold[Johnson 1972] and is embedded in air. The resonator has equal lateral dimensions l_x and l_z of 200nm and a thickness l_y of 25nm, while the gap width is set to 60nm.

In [Varault 2013] we illustrated how multipolar couplings affect the induced dipole moments for U-shaped resonators such as described in Fig. 2.6, even for particle sizes as small as $\approx \lambda/10$. Using an appropriate formulation of the Finite Element Method (FEM), the induced electric and magnetic dipole moments, $\mathbf{p}$ and $\mathbf{m}$, can be calculated for each illumination configuration. Symmetry considerations as well as numerical values confirm that one can approximate, for the studied metallic magneto-electric scatterer and at the wavelength $\lambda = 1375$ nm, the polarizability tensor of equation 2.16 by a tensor that depends on the projection $\cos(\theta)$ of the incoming wavevector on the $\hat{\mathbf{z}}$ axis, which bears the asymmetry of the structure (see figure 2.6): [Varault 2013]

$$\bar{\bar{\alpha}}_{cor} = \begin{bmatrix} \alpha_{xx}^{ee} + a_{xxz}\cos\theta & 0 & 0 & 0 & \alpha_{xy}^{em} + b_{xyz}\cos\theta & 0 \\ 0 & 0 & 0 & 0 & 0 & 0 \\ 0 & 0 & \alpha_{zz}^{ee} & 0 & 0 & 0 \\ 0 & 0 & 0 & 0 & 0 & 0 \\ \alpha_{yx}^{me} + c_{yxz}\cos\theta & 0 & 0 & 0 & \alpha_{yy}^{mm} + d_{yyz}\cos\theta & 0 \\ 0 & 0 & 0 & 0 & 0 & 0 \end{bmatrix} \tag{2.18}$$

In the latter expression, each component is constant for the considered wavelength: all the modifications induced by the incidence angle are properly described by the $\cos(\theta)$ dependence. This $\cos(\theta)$ dependence comes from the ∇_k derivatives in equation 2.17, in other words, they are due to the first-order retardation effects of the incident electromagnetic fields on the scattered fields, which are not symmetric respectively to the $\hat{\mathbf{z}}$ axis.

This model, that is deduced from the computation of the induced dipole moments when the incidence lies either in the (yOz) plane (with the electric field on the $\hat{\mathbf{x}}$ axis) or the (xOz) plane (with the magnetic field on the $\hat{\mathbf{y}}$ axis), is then confirmed by checking that it gives the correct predictions of dipole moments with some oblique incidences. Those oblique incidences also reveal that the corrected form of equation 2.18 are mandatory in order to obtain the correct values of the dipole moments in the studied structure. [Varault 2013]

2.3 Long range coupling effects in 1D periodic arrays

Since the discovery of (natural) diffraction gratings in the late 17^{th} century by James Gregory, the diffraction of light by periodic structures has been thoroughly studied and a remarkable amount of applications were found, *e.g.* monochromators, spectrometers, and chirped pulse amplification systems. Today a number of methods allow to calculate the diffraction and absorption of EMWs by periodic structures, the choice of one technique over another being guided by the practical domain of application of a given method, or by the user's preference.

In the following, we will present a method, detailed in [Rolly 2012b], that allows one to readily calculate the "leaky modes" of 1-dimensional periodic arrangements of sub-wavelength spheres (each sphere being homogeneous and identical to its neighbors) in a homogeneous embedding medium. Since the method is based on the resolution of a periodic Green's function, it can actually retrieve not only the leaky modes, but also the eigenvectors, the near- or far-fields, *etc.*

2.3.1 Electric dipole couplings in 1D arrays of resonators

The problem under study consist in an infinite line of identical sub-wavelength sized spherical resonators aligned along the z axis with center-to-center separation d. The principal characteristic of the individual chain elements is that their material properties produce a resonant electric dipole response in sub-wavelength particles (*e.g.* noble metal particles in the visible spectrum). See fig. 2.7.

We want to compute what we shall henceforth call "leaky modes" of the array, characterized by a complex-valued $\beta(\omega)$ parameter which, based on the assumptions of equations 2.20 and 2.21 below, induces a resonant behavior of the excitation fields of the resonators. In section 2.3.2 we will discuss the physical meaning and consequences of the equations cast below; here we derive the mathematical model and the algorithms that allow us to find the adequate $\beta(\omega)$ complex values.

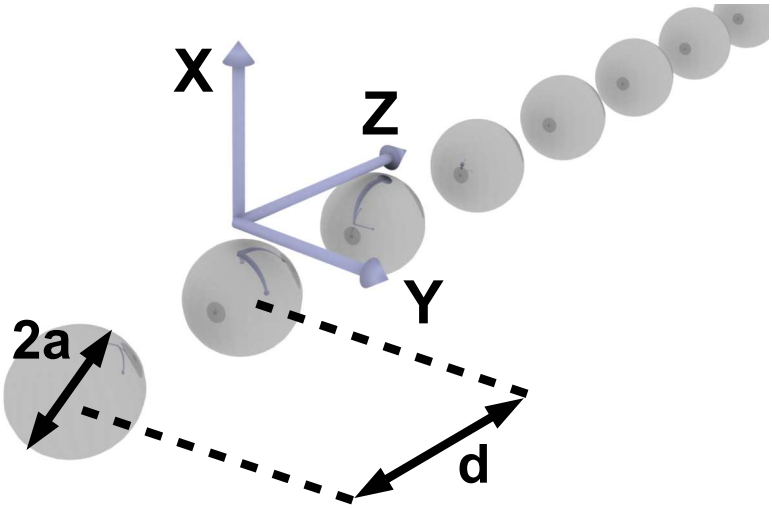

Figure 2.7: Schematic of the studied one-dimensionnal array of spherical particles. The chain lies along the z axis and is characterized by the material of the scatterers, their radius a, and the center-to-center distance d between them.

We recall that the electric field radiated by a point dipole of moment $\mathbf{p}$, immersed in an embedding "matrix'' of permittivity ε_m, is given by equation 1.2:

$$\mathbf{E}_{\mathrm{s}}(\mathbf{r},\omega) = \frac{e^{ikr}}{4\pi\varepsilon_b\varepsilon_0 r^3}\left\{(1-ikr)\left[3\hat{\mathbf{r}}\left(\hat{\mathbf{r}}\cdot\mathbf{p}\right)-\mathbf{p}\right]+k^2r^2\left(\left(\hat{\mathbf{r}}\times\mathbf{p}\right)\times\hat{\mathbf{r}}\right)\right\}\ , \tag{2.19}$$

where the spherical position vector $\mathbf{r} = r\hat{\mathbf{r}}$ is centered on the dipole, and $k \equiv (\omega/c)\sqrt{\varepsilon_b}$ is the wavenumber of the background medium. In the equations below we use the dimensionless polarizability $\tilde{\alpha}$:

$$\begin{aligned}\tilde{\alpha}(\omega) &\equiv \alpha(\omega)/(4\pi a^3)\\ \mathbf{p}(\omega) &= 4\pi a^3\varepsilon_0\varepsilon_b\tilde{\alpha}(\omega)\mathbf{E}_{\mathrm{exc}}(\omega)\end{aligned} \tag{2.20}$$

The incident, excitation and total fields are all assumed to satisfy the quasi-periodic phase condition on the wavevector component along the z axis, henceforth denoted β :

$$\begin{aligned}\beta &\equiv \mathbf{k}\cdot\hat{\mathbf{z}},\\ \mathbf{E}_{\mathrm{inc,exc,tot}}(z+d) &= e^{i\beta d}\mathbf{E}_{\mathrm{inc,exc,tot}}(z).\end{aligned} \tag{2.21}$$

If the incident field is a plane wave, then β is the projection of its wavevector, $\mathbf{k}_{\mathrm{inc}}$, along the z axis, which constrains $|\beta| \leq k$, but in general, propagating modes only need to satisfy the condition $\mathrm{Re}(\beta) \leq 2\pi/d$, imposed by the lattice spacing.

The Foldy-Lax excitation field for an arbitrary particle is the superposition of the incident field and the field scattered by all the other particles in the line. Using eq. 2.20 for the dipole moments of the particles, and eq.(2.19) for their scattered fields,

the transverse and longitudinal excitation fields (*i.e.* "transverse" and "parallel" with respect to the line) are respectively:

$$E_{\mathrm{e},\perp} = E_{\mathrm{i},\perp} - \left(\frac{a}{d}\right)^3 \widetilde{\alpha} \sum_{j\in\mathbb{Z}^*} \frac{e^{i(|j|kd+j\beta d)}}{|j|^3} \left(1 - i\,|j|\,kd - (jkd)^2\right) E_{\mathrm{e},\perp}$$
$$E_{\mathrm{e},\parallel} = E_{\mathrm{i},\parallel} + \left(\frac{a}{d}\right)^3 \widetilde{\alpha} \sum_{j\in\mathbb{Z}^*} \frac{2e^{i(|j|kd+j\beta d)}}{|j|^3} \left(1 - i\,|j|\,kd\right) E_{\mathrm{e},\parallel}.$$

The above relations can both be generically written:

$$E_{\mathrm{e}} = E_{\mathrm{i}} + \Sigma\left(\omega,\beta\right) \widetilde{\alpha} E_{\mathrm{e}} \ . \tag{2.22}$$

where Σ is a "self" employed by some authors [Koenderink 2006, Conforti 2010], that represents the sum of the array couplings (henceforth called "lattice sum") $\zeta(j, kd, \beta d)$ between two particles separated by jd:

$$\begin{aligned} \zeta_{\perp}\left(j,kd,\beta d\right) &\equiv -\frac{1}{(kd)^3}\left(\frac{1}{|j|^3} - ikd\frac{1}{j^2} - (kd)^2\frac{1}{|j|}\right) e^{i(|j|kd+j\beta d)} \\ \zeta_{\parallel}\left(j,kd,\beta d\right) &\equiv \frac{2}{(kd)^3}\left(\frac{1}{|j|^3} - ikd\frac{1}{j^2}\right) e^{i(|j|kd+j\beta d)} \ . \end{aligned} \tag{2.23}$$

$$\Sigma\left(\omega,\beta\right) \equiv (ka)^3 \sum_{j\in\mathbb{Z}^*} \zeta\left(j,kd,\beta d\right) \ , \tag{2.24}$$

The solution for the excitation field for either polarization is then:

$$E_{\mathrm{e}} = \frac{E_{\mathrm{i}}}{1 - \widetilde{\alpha}\Sigma\left(\omega,\beta\right)} \ , \tag{2.25}$$

and the dispersion relations of the quasi-modes are obtained by solving:

$$1 - \widetilde{\alpha}\Sigma\left(\omega,\beta\right) = 0 \ , \tag{2.26}$$

which is the required condition for a non-zero excitation field to exist in the absence of an incident field.

Inspection of eqs.(2.23)-(2.24) shows that all terms in the lattice sum of Σ can be expressed in terms of polylogarithm functions which are defined by [Abramowitz 1972]:

$$\mathrm{Li}_n\left(z\right) = \sum_{j=1}^{\infty} \frac{z^j}{j^n} \ ,$$

whereby the selfs of eq.(2.24) can be expressed using polylogarithm functions (see also [Koenderink 2006, Linton 2009, Conforti 2010, Campione 2011] and references

there-within):

$$\begin{aligned}\Sigma_{\perp}(\omega,\beta,d) =& -(\frac{a}{d})^3\{[\mathrm{Li}_3(e^{i(k-\beta)d})+\mathrm{Li}_3(e^{i(k+\beta)d})]\\ &-ikd[\mathrm{Li}_2(e^{i(k-\beta)d})+\mathrm{Li}_2(e^{i(k+\beta)d})]\\ &-(kd)^2[\mathrm{Li}_1(e^{i(k-\beta)d})+\mathrm{Li}_1(e^{i(k+\beta)d})]\}\\ \Sigma_{\parallel}(\omega,\beta,d) =& 2(\frac{a}{d})^3\{[\mathrm{Li}_3(e^{i(k-\beta)d})+\mathrm{Li}_3(e^{i(k+\beta)d})]\\ &-ikd[\mathrm{Li}_2(e^{i(k-\beta)d})+\mathrm{Li}_2(e^{i(k+\beta)d})]\}\end{aligned} \tag{2.27}$$

Strictly speaking, the polylogarithm series $\mathrm{Li}_n(z)$ of positive order n that appear in equation 2.27 only converge for $|z|<1$, but they can be analytically continued onto the complex plane with a branch cut on the real line, for $x\in]1,\infty[$; for a real argument strictly greater than 1, the series grossly diverge. A recursive numerical algorithm allows to compute the polylogarithms in a fast and accurate manner (worst-case scenario of 1 precision bit per loop) [Crandall 2006].

2.3.2 Discussion on the physical meaning of "leaky modes"

Upon injecting equation 2.26 into 2.22, one obtains:

$$E_{\mathrm{inc}}=0. \tag{2.28}$$

It ensues that this model does not seem to be able to provide a concrete way of exciting the so-called leaky modes. We discuss this assumption below after some further developments of the model. To the best of our knowledge, there is no known analytical solution to equation 2.26, and thus a numerical resolution is required. Equation 2.26 is scalar, because a coupling type (transverse or longitudinal) has been chosen, but in a general form it can be cast: [Rolly 2012b]

$$\mathbf{Id}-t\mathbf{\Sigma}(\omega,\beta)=0 \tag{2.29}$$

where t is the T-matrix of an isolated resonator, and $\Sigma(\omega,\beta)$ can be cast with the same polylogarithm functions as in equation 2.27 (see next section). With the appropriate algorithms (in the multipole formulation case, a commercially available Singular Value Decomposition algorithm, followed by a dichotomy method based on the analytical properties of the functions used in equation 2.29 relatively to β; in the electric dipole case, only the dichotomy algorithm is used) we can compute both the eigenvector and eigenvalue of the matrix on the left hand side of equation 2.29 (henceforth named $\mathbf{B}(\omega,\alpha,\beta)$). The inverse of $\mathbf{B}(\omega,\alpha,\beta)$ can be cast:

$$\mathbf{A}(\omega,\widetilde{\alpha},\beta)=[\mathbf{Id}-\widetilde{\alpha}\Sigma(\omega,\beta)]^{-1}. \tag{2.30}$$

From equation 2.25, we can see that $\mathbf{A}$ verifies:

$$\mathbf{e}_{\mathrm{exc}}=\mathbf{A}(\omega,\widetilde{\alpha},\beta)\mathbf{e}_{\mathrm{inc}}, \tag{2.31}$$

with $\mathbf{e}_{\text{exc}}$ and $\mathbf{e}_{\text{inc}}$ respectively the vector of the exciting, and incoming fields. When solving equation 2.26 at a fixed frequency ω_0, we equivalently solve $|\mathbf{A}| \to \infty$. Since the resolution is numerical, we do not get the exact solutions in the general case. We thus check that the corresponding complex eigenvalue $\lambda(\omega_0, \widetilde{\alpha}, \beta)$ of $\mathbf{B}(\omega, \widetilde{\alpha}, \beta)$ verifies:

$$|\mathbf{B}(\omega, \alpha, \beta).\mathbf{E}_\lambda| \leq |\lambda(\omega_0, \widetilde{\alpha}, \beta)||\mathbf{E}_\lambda| \tag{2.32}$$

for the eigenvector $\mathbf{E}_\lambda$ of each eigenvalue $\lambda(\omega_0, \widetilde{\alpha}, \beta)$, with $0 < |\lambda(\omega_0, \beta)| < \varepsilon_{\max}$ whose modulus is lower than $\varepsilon_{\max} = 10^{-15}$, typically as low as 10^{-17}.

Accordingly, if we consider incoming fields described by the corresponding eigenvectors of the inverse matrix $\mathbf{A}(\omega_0, \widetilde{\alpha}, \beta)$, the resulting exaltation of the modulus of the excitation fields (compared to the incoming fields) would be as high as 10^{15} and over. Because such exaltations seem rather unphysical at first glance, it should be noted that the corresponding incoming fields described by the quasi-periodic relation of equation 2.21 are certainly unphysical themselves, since they grow exponentially in the $\pm z$ direction (according to sign$[\Re(\beta)]$) and thus their modulus diverges in this direction. A more realistic way of excitation of the leaky modes is to use an incident beam that has the required shape as dictated by equation 2.21, but with a finite extension in the spatial and/or in the time domain.

2.3.3 Multipole formulation of the chain coupling

In [Rolly 2012b] we further develop the model in order to take into account the effect of multipole contributions to the values $\beta(\omega_0)$ of the leaky modes' incident wavevector values at a given frequency ω_0. The selfs of equation 2.24 become coupling matrices $\mathbf{\Omega}(\omega, \beta)$ whose coefficients have the following expression:

$$[\Omega]_{q,p;q'p'} = \sum_l C_l\left(p, q; p', q'\right) l_l\left(\omega, \beta\right), \tag{2.33}$$

where the sum over the l index is finite and analytic expressions exist for the $C_l\left(p, q; p', q'\right)$ coefficients [Tsang 1985, Chew 1990, Stout 2002]. The line sums l_n, of the spherical Hankel functions along the z axis are defined by [Linton 2009]:

$$l_n\left(\omega, \beta\right) \equiv \sum_{j \in \mathbb{Z}^*} \mathcal{H}_{n,0}\left(jkd\hat{z}\right) e^{ij\beta d} = \sqrt{\frac{2n+1}{4\pi}} \sum_{j=1}^{\infty} h_n\left(jkd\right)\left[e^{ij\beta d} + (-1)^n e^{-ij\beta d}\right], \tag{2.34}$$

with $\mathbf{H}\left(\mathbf{x}\right)$ denoting the irregular translation-addition matrix corresponding to a displacement vector $\mathbf{x}$.

One can then define a modified (array-equivalent) *multiple-scattering* T-matrix, denoted here by $\mathbf{T}$, which takes into account all multiple-scattering effects. For an infinite periodic system of identical particles, T is defined to yield the scattered field coefficients $f^{(j)}$ directly in terms of the incident field coefficients on that particle, *i.e.*:

$$\mathbf{f}^{(j)} \equiv \mathbf{T}\mathbf{a}^{(j)},$$

where $a^{(j)}$ is the vector containing the coefficients of the incoming field, expressed at the position of the j^{th} scatterer. The Foldy-Lax multiple-scattering formalism yields a matrix equation for the multiple-scattering T matrix: [Rolly 2012b]

$$\mathbf{T} = \mathbf{t} + \mathbf{t}\boldsymbol{\Omega}\left(\omega, \beta\right)\mathbf{T} \ , \tag{2.35}$$

where the multiple-scattering multipole expression of $\boldsymbol{\Omega}(\omega, \beta)$ has been defined above in equation 2.33. The solution to eq.(2.35) for the multiple-scattering T matrix is:

$$\mathbf{T} = \left[\mathbf{t}^{-1} - \boldsymbol{\Omega}\right]^{-1} \ , \tag{2.36}$$

while the wavenumbers of propagating leaky modes of the chain correspond to values of β, for which the matrix inside the brackets has a zero eigenvector ν :

$$\left[t^{-1} - \Omega\right]\nu = 0 \ . \tag{2.37}$$

A direct calculation of matrix inversion of eq.(2.36) is delicate since the matrix is generally ill-conditioned. This difficulty can be generally overcome by analytical matrix balancing as described in [Rolly 2012b].

2.3.4 Multipole effects on the leaky modes

For the illustration of our multipole resolution of the leaky modes computation, we adopt the same parameters for a plasmonic chain as Conforti and Guasoni.[Conforti 2010] Namely, we consider an infinite chain of identical 50nm diameter silver particles separated by a center-to-center distance $d = 75$ nm. The system is immersed in a non-magnetic medium with relative permittivity $\varepsilon = 2.25$ ($n_m = 1.5$). There is no universally accepted permittivity function for silver, we thus adopted here an experimental fit for the permittivity of silver proposed by Tanabe [Tanabe 2008], given in [Rolly 2012b], which provides at least 6 significant digits.

The figures are plotted with normalized frequencies and wave-vectors:

$$\tilde{\omega} \equiv \frac{\omega d}{2\pi c} = \frac{d}{\lambda_{\mathrm{v}}} \qquad \tilde{\beta} \equiv \frac{\beta d}{2\pi}$$

where λ_{v} is the vacuum wavelength. The light line for these parameters is given by $\tilde{\omega} = \frac{\tilde{\beta}}{n_{\mathrm{med}}}$. The dispersion relations of the principal propagating modes are calculated in the electric dipole approximation by numerically solving equation (2.26) and are plotted in figure 2.8 (dashed curves). They are then compared with fully converged $n_{\max} = 10$ calculations of these dispersion relations (solid line) in this same figure by solving eq.(2.37). The imaginary part of the dispersion relations for dipolar and converged multipole calculations are given in figure 2.9.

It is immediately clear that the dipole approximation provides an accurate prediction of dispersion relations only over a narrow range of frequencies for which the imaginary part of the propagating wavevector is rather small, and the real part is near the light line. One should also remind that symmetry dictates that if a given

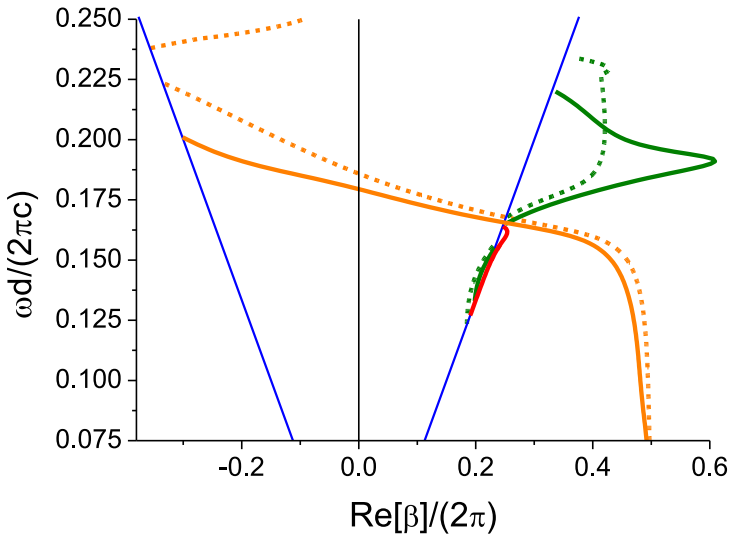

Figure 2.8: Real part of the dispersion relations in the dipole approximation (dashed curves), and fully converged multipole calculations with $n_{\max} = 10$ (full lines). (green) Longitudinal mode with positive imaginary part; (red) "T1" mode with positive imaginary part; (orange) "T2" transverse mode with negative imaginary part; (blue) light line.

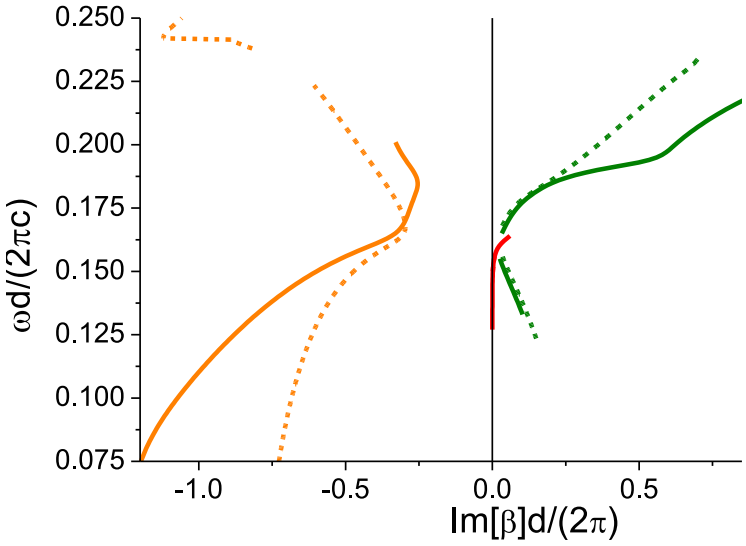

Figure 2.9: Imaginary part (b) of the dispersion relations with the dipole approximation (dashed curves), and with fully converged multipole calculations $n_{\max} = 10$ (full lines). (green) Longitudinal mode with positive imaginary part; (red) "T1" mode with positive imaginary part; (orange) "T2" transverse mode with negative imaginary part.

value of β corresponds to a mode at a given frequency, then by symmetry, $-\beta$ is also a solution to these equations. For the sake of clarity, these symmetric modes are not presented in these figures.

Like Conforti and Guasoni [Conforti 2010], we found a transverse mode, labeled "T2" whose imaginary part of β is opposite in sign with its real part. It is interesting to remark that this T2 mode tends toward the edge of the Brillouin zone at low frequencies. Our dipole predictions for the longitudinal mode are quite similar to that of [Conforti 2010] wherein the dipole prediction is that the mode "folds back" before reaching the edge of the Brillouin zone. The full multipole calculations on the other hand predict that the longitudinal mode goes to the edge of the Brillouin zone, and that the "fold back" only occurs after it has gone "beyond" the edge of the Brillouin zone. Our dipole calculations of the "T1" mode with positive imaginary part give quite similar results in the dipole and multipole cases, except that we only found that the full multipole solution predicted both extremities of the T1 mode to lie on the light line. We point out some strange behavior of the modes in the electric dipole approximation at high frequencies. For instance, at around $\widetilde{\omega} = 0.225$ a "kink" appears in the longitudinal mode, and a spurious T2 solution emerges from the light line. We carried out mode calculations with various multipole cutoffs and found that such kinks and spurious solutions were relatively commonplace (at high or low frequencies) when low numbers of multipoles are used in the simulations; and such behavior disappears when higher multipole orders are used (the computation times are much higher though, in the multipole formulation). It is also worth remarking that for high order simulations, the $\mathrm{Re}[\beta]$ of the modes terminate at either the light line, or the edge of the Brillouin zone; but when the calculations are carried out at lower multipolar orders, some modes seem to terminate at arbitrary points in the (ω, β) space.

Chapter 3

From Matter to light (local excitation)

"I regard consciousness as fundamental. I regard matter as derivative from consciousness. We cannot get behind consciousness. Everything that we talk about, everything that we regard as existing, postulates consciousness."
Max Planck, German physicist (1858-1918)

Contents

In this chapter, we will discuss the case of a local excitation of a photonic structure, and show the decay rates and directivity enhancements of a few structures. We assume that the emitter, placed in the optical antenna structure, can be treated as an (electric or magnetic) point-dipole. In section 3.1, we will introduce fast algorithms for the decay rate computations; we will also study a dimer gap antenna design of (metallic or dielectric) particles, that allows orders of magnitude enhancements of the decay rates, and present the results of our collaboration with Sébastien Bidault and Michaël Busson from Institut Langevin, Paris. In section 3.2, we will discuss the use of both electric and magnetic induced dipoles in dielectric spheres for increasing the directivity of the radiation pattern. We will then present some hybrid, metallo-dielectric structures that are able to greatly enhance both the decay rates and directivity of an electric dipole emitters (section 3.3).

3.1 Enhancing the decay rates

3.1.1 Decay rates formulas in the GMT framework

Stout *et al.* gave in 2011 fast GMT based algorithms for the computation of the decay rates [Stout 2011]. For an extended derivation, see appendix D.2. The normalized decay rates can be cast:

$$\widetilde{\Gamma}_{\mathrm{t}} \equiv \frac{\Gamma_{\mathrm{t}}}{\Gamma_{\mathrm{t},0}} = 1 + \frac{\mathrm{Re}\left\{6\pi k_b \sum_{j,l=1}^{N} \mathbf{f}^{\dagger}\, \mathbf{H}^{(e,j)}\, \mathbf{T}^{(j,l)}\, \mathbf{H}^{(l,e)}\, \mathbf{f}\right\}}{\mathrm{Re}\left\{k_b\right\}} \tag{3.1}$$

$$\begin{aligned}\widetilde{\Gamma}_{\mathrm{r}} \equiv \frac{\Gamma_{\mathrm{r}}}{\Gamma_0} &= 1 + 6\pi \sum_{i,j,k,l=1}^{N} \mathbf{f}^{\dagger} \left[\mathbf{T}^{(j,i)}\mathbf{H}^{(i,e)}\right]^{\dagger} \mathbf{J}^{(j,k)}\, \mathbf{T}^{(k,l)}\, \mathbf{H}^{(l,e)}\, \mathbf{f} \\ &\quad + 12\pi\, \mathrm{Re}\left[\sum_{j,l=1}^{N} \mathbf{f}^{\dagger}\, \mathbf{J}^{(e,j)}\, \mathbf{T}^{(j,l)}\, \mathbf{H}^{(l,e)}\, f\right]\end{aligned} \tag{3.2}$$

where $\mathbf{J}$ and $\mathbf{H}$ are regular and irregular translation matrices, respectively (see appendix C.1). The multiple-scattering results of eqs.(3.1) and (3.2) simplify considerably when a single antenna particle is present:

$$\widetilde{\Gamma}_{\mathrm{t}} = 1 + \frac{\mathrm{Re}\left\{6\pi k_b f^{\dagger}\, H^{(e,j)}\, t\, H^{(j,e)}\, f\right\}}{\mathrm{Re}\{k_b\}} \tag{3.3}$$

$$\widetilde{\Gamma}_{\mathrm{r}} = 1 + 6\pi \left[H^{(j,e)}\, f\right]^{\dagger} t^{\dagger}\, t\, H^{(j,e)}\, f + 12\pi\, \mathrm{Re}\left[f^{\dagger}\, J^{(e,j)}\, t\, H^{(j,e)}\, f\right] \tag{3.4}$$

where t is the single-particle T-matrix. If the T-matrix is that of a spherical (Mie) scatterer, then eqs.(3.3) and (3.4) are equivalent to expressions that were derived previously for Mie scatterers.[Kerker 1980, Ruppin 1982, Kim 1988, Carminati 2006, Colas des Francs 2008]

Similarly, equations 3.1 and 3.2 also take a simpler form when one considers multiple scatterers, but neglects multipole effects. The rather simple induced dipole formalism can give fast approximations of the decay rates variations of systems where the multipole effects are present, but not predominant. In practice, one can use the formulas of equations 3.1 and 3.2 in an induced dipole approximation that consists in choosing a maximal multipole expansion number $n_{\max} = 1$, which gives simple, dipolar formulas (see [Stout 2011] for the case of a Yagi-Uda design, for instance).

3.1.2 Metallic gap antennas for electric dipoles

As seen in the introduction chapter (in section 1.2.1), an efficient way of enhancing the decay rates of an electric dipole is to use a nanogap dimer structure, that we call a "super-emitter" (see section 1.2.1). The orientation of the dipole moment relatively to the dimer axis influence the decay rates and the quantum efficiency. The longitudinal coupling (orientation along the dimer axis) generally yields the highest decay rates enhancements, as well as the best possible quantum efficiencies. [Liaw 2010]

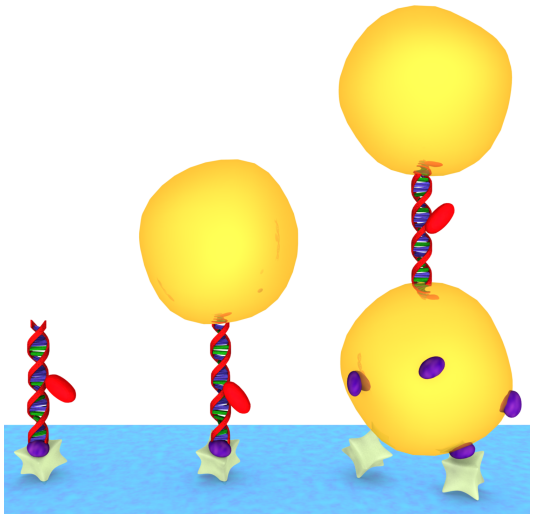

Figure 3.1: Sketch of the analysed samples: from left to right, the "isolated" ATTO647N fluorophore linked to a DNA strand; the fluorophore linked to a gold monomer; the fluorophore placed at the centre of a gold dimer.

Michaël Busson and Sébastien Bidault from Institut Langevin, Paris, and coworkers successfully synthesized DNA-templated gold dimers, 36 nm in diameter, a size which is sufficient to observe significant scattering. They used a bottom-up technique that consists in grafting complementary DNA strands to two separate monomer suspensions before mixing them in order to obtain the DNA hybridization that links two monomers together. This method is highly reproducible, and adapted to large-scale production. We calculated theoretical scattering cross-sections that helped characterize the geometrical properties of the dimers, in terms of size and inter-particle distance, which can be tuned in the $\approx 6-20$ nm range using different lengths of the DNA linker between the particles (30 or 50 base pairs – bp). In particular, the nanogap lengths were independently measured, via the agreement between our theoretical scattering cross-section computations, and the spectra obtained from dark-field spectroscopy on the one hand; and direct observation via TEM images, on the other hand. Both of the experiments were realized on extended samples, and were rendered feasible thanks to an automatization of the measures. [Busson 2011]

In a second step, M. Busson and S. Bidault reproduced the same synthesizing protocol, but they used DNA linkers on which a single ATTO647N emitter was grafted per linker. In order to provide theoretical support, we calculated the theoretical decay rate enhancements of the 3 different sample types, see figure 3.1, with two different emitter-particle distance for monomers and dimers ($d = 6$ or 8 nm, that correspond to the nanogaps of the 30 bp and 50 bp linkers respectively, as estimated in [Busson 2011]), a total of 5 different configurations. Those decay rate enhancements are displayed in figure 3.2a-b as a function of the orientation of the emitting dipole moment with respect to the dimer axis. We remark that both the total and

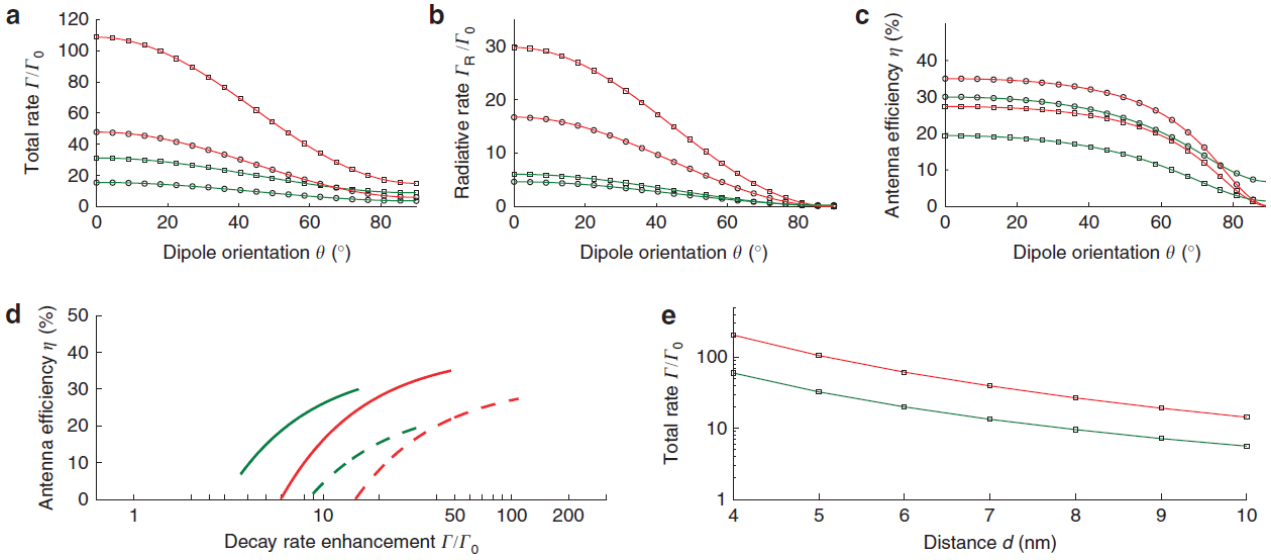

Figure 3.2: Theoretical decay rates and antenna efficiencies provided by 36 nm diameter gold (green solid lines) monomers and (red solid lines) dimers.(a) Total, (b) radiative decay rate enhancements, (c) antenna efficiency, as a function of the emission dipole orientation, θ, for a fixed emitter-particle distance, d. (open squares) $d = 6$ nm, (open circles) d=8 nm. The markers correspond to Mie theory calculations and the solid lines to a $A+B\cos^2\theta$ fit of the decay rates. (d) Evolution of the antenna efficiency $\eta = \Gamma_{\text{rad}}/\Gamma_{\text{tot}}$, as a function of Γ_{tot} for (green lines) monomers and (red lines) dimers, obtained by combining sub-figures a-c. The dashed lines correspond to $d = 6$ nm and the solid lines to $d = 8$ nm. (e) Same as sub-figure a, but for a fixed orientation $\theta = \pi/4$ and a varying emitter-particle distance d.

radiative decay rate enhancements can be well approximated by a $A + B\cos^2\theta$ fit, where θ is the angle between the dipole moment and the dimer axis. To a given value of $\tilde{\Gamma}_{\text{tot}}$, one can thus assign a unique value of $\tilde{\Gamma}_{\text{rad}}$ obtained at the same emitter orientation θ, and thus a unique value of $\eta = \tilde{\Gamma}_{\text{rad}}/\tilde{\Gamma}_{\text{tot}}$; this allows to cast the quantum efficiency η as a function of $\tilde{\Gamma}_{\text{tot}}$ in figure 3.2d. We can see that orientations parallel to the dimer have substantially higher efficiency: they correspond to the rightmost and uppermost part of the curves in this figure. As a matter of fact, longitudinal couplings are known to provide both the highest radiative decay rates and quantum efficiencies in monomer[Carminati 2006] and dimer [Liaw 2010] configurations. We also computed the theoretical decay rates for an emitter orientation of $\theta = \pi/4$ with a varying emitter-sphere distance, figure 3.2e. [Busson 2012a]

The fluorescence lifetime are measured in a pulsed excitation regime, using time-correlated single photon counting, 420 samples were measured. The instrument response is 75 ± 5 ps, and allowed to estimate lifetimes as low as 35 ± 5 ps in a particular dimer sample, a 90-fold enhancement of the initial decay rate ($3200 \pm 150ps$). Figure 3.3 shows a comparison between the experimentally measured decay rates

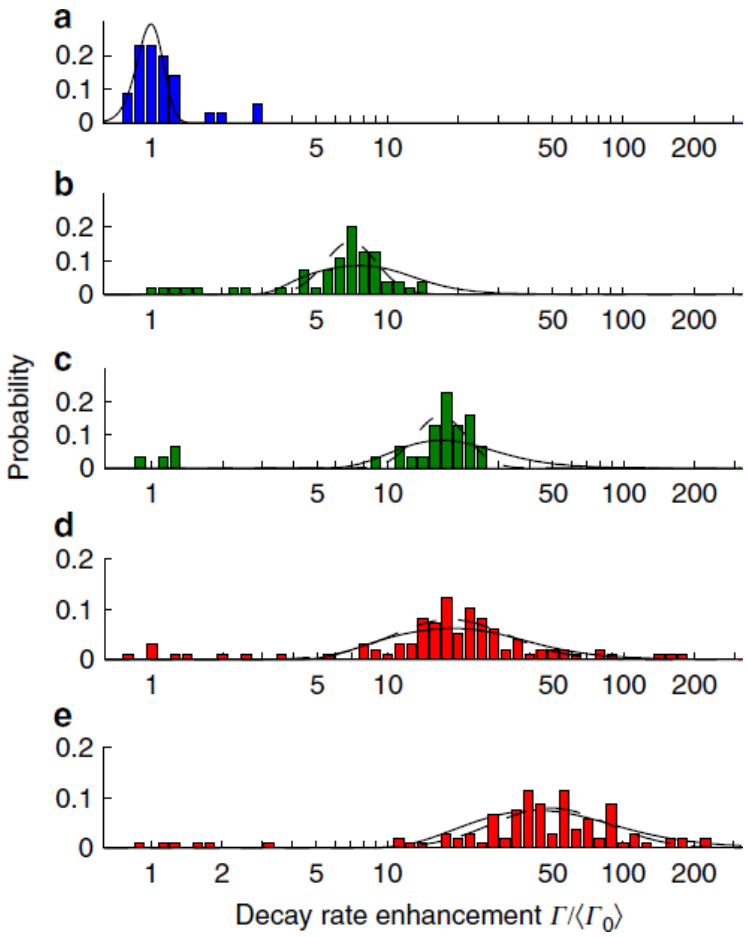

Figure 3.3: Distributions of decay rate enhancements $\Gamma/ < \Gamma_0 >$. (a) Isolated ATTO647N molecules, monomers with (b) 50 and (c) 30 DNA base pair linkers, dimers with (d) 50 and (e) 30 base pair linkers. The solid black line in (a) is a Gaussian fit of the experimental $\Gamma_0/ < \Gamma_0 >$ distribution. Solid and dashed lines in (b-e) : see text.

and the theoretical predictions using two separate sets of assumptions, that are related to both of the previously shown calculations (figure 3.2d-e) and considers the 5 configurations : single emitter, and 30 bp and 50 bp DNA linker monomer and dimer. The first set of assumptions is: for each of the 4 samples, a fixed distance d (as estimated from [Busson 2011]) and an isotropic distribution of the orientation of the emitter, θ, relatively to the dimer axis. The second set of assumptions is: a fixed emitter orientation $\theta = \pi/4$ and a Gaussian distribution of distances with a ± 1 nm standard deviation (± 0.5 nm for monomers). The theoretical values of decay rates are then convoluted to the distribution of the decay rates observed within the isolated fluorophores sample, in order to obtain the theoretical values in figures 3.3b-e: solid black lines are the results using the first set of assumptions, and dashed black lines are the results using the second set. We can see that both sets of assump-

tions (fixed distance, isotropic orientation; fixed orientation, Gaussian distribution of the distance) agree quite well with the experimental data. In practice, there is a distribution of both the distance and the emitter orientation, and the highly satisfactory agreement between the theoretical calculations and the experimental values indicates that the actual positioning uncertainty of the dye molecule inside the gap of the dimers is probably the order of ≈ 1 nm, a scale unreachable with top-down lithography techniques. [Busson 2012a]

The dye-grafted dimer antennas can be considered as artificial, hybrid metal-organic antennas. They can be put in solution and characterized like classical organic molecules, using FCS techniques. The 30 bp DNA linker dimer is able to enhance the fluorescence signal by 35% in the linear regime, compared to the isolated DNA-grafted ATTO647N emitter; and to reduce the mean excited state lifetime by a factor 66, in excellent agreement with our theoretical predictions. [Busson 2012b]

There are two main perspectives for those "hybrid metal-organic chromophores". Firstly, they can be further engineered in order to better tune the dimer plasmonic resonance to the fluorophore emission wavelength, by carefully choosing the radius of the particles and the nanogap size, and/or by selecting another fluorophore. Secondly, in order to have bright, identical chromophores, the orientation of the fluorophore's electric dipole moment needs to be controlled somehow, and preferably fixed to lie along the dimer axis, in order to obtain the highest values of both the radiative decay rate and quantum efficiency of the emission.

3.1.3 Dielectric particle and gap antennas for electric and magnetic dipoles

3.1.3.1 General formulas from the GMT

Single-particle and dimer gap antennas can also be made of a dielectric materials, and these can be used to enhance the decay rates of both electric and magnetic dipoles. They can also be used to promote the magnetic dipole transition rates compared to those of the electric dipole. [Rolly 2012a] Magnetic dipole transitions occur naturally, *e.g.* in some lanthanide ions [Weber 1973, Karaveli 2011], when allowed by quantum selection rules; most of the time, though, those magnetic dipole transitions compete with dominant electric dipole transitions, *e.g.* because they share the same initial excited state. The typical prevalence of the magnetic dipole transition rates versus those of the electric dipole varies with the embedding medium or surrounding crystalline structure, with values around 10 to 40%. [Karaveli 2011]. The enhancement of magnetic dipole transitions has many possible applications, such as the tuning of the spectral emission of lanthanide ions [Karaveli 2011], left-handedness in erbium-doped crystals [Thommen 2006], and magnetic field-enhanced spectroscopy [Albella 2013], for instance.

We consider a dielectric sphere characterized by its electric dipole, magnetic dipole, electric quadrupole and magnetic quadrupole Mie coefficients written respectively c_1^e, c_1^m, c_2^e and c_2^m. The quadrupole resonances are considered, since,

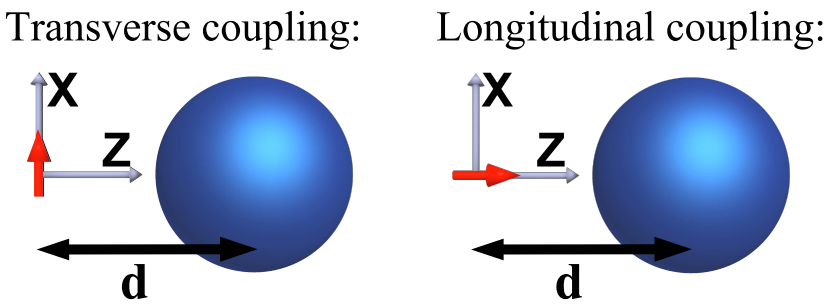

Figure 3.4: Sketch of the (left) Transverse and (right) Longitudinal couplings

on the one hand, they do not dissipate the emitter's power in the case they are lossless dielectrics (as opposed to metals that can strongly quench the emission [Thomas 2004, Carminati 2006, Liaw 2010]); on the other hand, their moderate quality factor are compatible with broadened emission lines, as opposed to multipoles of higher order, see section 1.1.2. An electric or magnetic dipole emitter is placed at a center-to-center distance d from the resonator. Using equation 3.1, the total decay rate enhancements can be cast: (see demonstration in appendix E.2)

$$\tilde{\Gamma}_{\text{tot}}^{L,u} = 1 + \text{Re}\left[-9\frac{e^{2ikd}}{(kd)^6}(1-ikd)^2 c_1^u + 45\frac{e^{2ikd}}{(kd)^8}(ik^2d^2-3kd-3i)^2 c_2^u\right] \tag{3.5}$$

$$\begin{aligned}\tilde{\Gamma}_{\text{tot}}^{T,u} = 1 + \text{Re}\big[&-\frac{9e^{2ikd}}{4(kd)^6}(1-ikd-k^2d^2)^2 c_1^u + \frac{15e^{2ikd}}{4(kd)^8}(-k^3d^3-3ik^2d^2+6kd+6i)^2 c_2^u \\ &+\frac{9e^{2ikd}}{4(kd)^4}(kd+i)^2 c_1^v - \frac{15e^{2ikd}}{(kd)^6}(-k^2d^2-3ikd+3)^2 c_2^v\big],\end{aligned} \tag{3.6}$$

where T and L refer to transverse (emitter perpendicular to the emitter-sphere axis) or longitudinal (emitter directed towards the sphere) couplings respectively (see figure 3.4), and $(u = e, v = m)$ for an electric, $(u = m, v = e)$ for a magnetic dipole emitter.

We can see in the above formulas that for a longitudinal coupling, only the resonances of the same type as the emitter are excited (owing to the fact that there is no longitudinal magnetic field for an electric dipole, and vice versa). Since the longitudinal couplings give the highest decay rates, it is thus possible to promote magnetic transition rates over electric ones, by using a longitudinal coupling of the emitter to the sphere. Nevertheless, in the case of an uncontrolled emitter orientation, the isotropically averaged values can favor the magnetic dipole transitions (see below). We illustrate below in sections 3.1.3.2 and 3.1.3.3 the use of high refractive index dielectric resonators, that support magnetic dipoles and multipoles, in order to enhance the electric or magnetic LDOS. We chose to consider Si spheres, a common material with negligible losses inthe near infrared (IR), and we aim at enhancing *e.g.* the ${}^4I_{13/2} \rightarrow {}^4I_{15/2}$ MD transition of Er^{3+} that occurs around $\lambda_0 = 1540$ nm [Weber 1973]. Because of the negligible losses of Si in the near IR, the radiative and total decay rates are assumed to be equal.

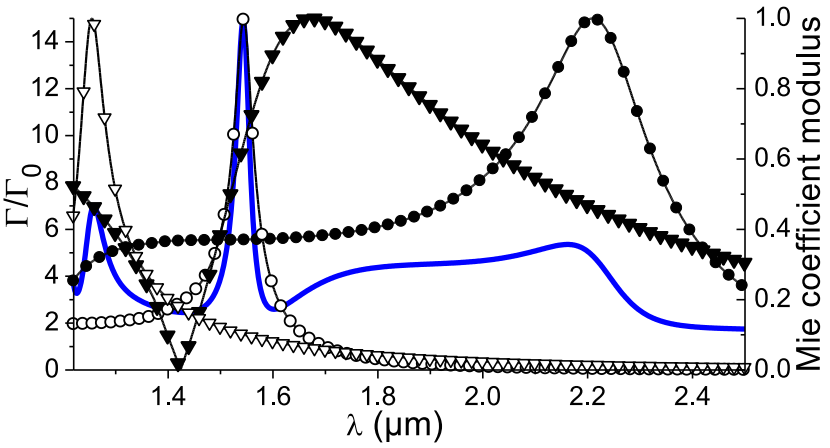

Figure 3.5: (Left scale, thick blue line) Decay rates for a magnetic dipole transversely coupled to a 2a = 615 nm diameter sphere as a function of the wavelength. (Right scale) Modulus of the Mie coefficients of the sphere: (full circles) magnetic dipole, b1; (full triangles) electric dipole, a1; (open circles) magnetic quadrupole, b2; (open triangles) electric quadrupole, a2.

3.1.3.2 Single Si resonator

We first consider a surrounding medium made of air, and a single Si sphere. The diameter of the sphere, $2a = 615$ nm, is chosen in order to optimize the decay rates of the magnetic dipole transition near $\lambda = 1540$ nm using a quadrupolar magnetic Mie resonance (see figure 3.5: the resonances of both the transverse coupling decay rate and the magnetic quadrupole are simultaneous, at $\lambda_0 = 1544$ nm). The results, displayed in Fig.3.6, show that a single dielectric sphere significantly enhances the normalized decay rates $\tilde{\Gamma} = \Gamma/\Gamma_0$ of a magnetic dipole emitter. The maximum decay rate enhancements occur with longitudinal couplings, and it can reach two orders of magnitude (e.g. at $\lambda = 1546$ nm) for a magnetic dipole emitter whereas it is limited to 25 for an electric dipole transition. As expected, for a longitudinal coupling, the magnetic and electric transitions have decay rate enhancement factors that are spectrally well separated (because each emitter type is only favored by the resonances of the same type in the sphere), whereas for a transverse coupling, both electric and magnetic emitters exhibit common maxima (because each resonance can enhance both emitter types). The isotropic average over the orientation of the dipolar moment ($\tilde{\Gamma}_{iso} = 1/3\tilde{\Gamma}_{//} + 2/3\tilde{\Gamma}_{\perp}$) is plotted in Fig.3.6c in the same wavelength window and confirms that the MD transitions are favored over ED transitions, on average, by coupling the emitter to the quadrupolar resonance of the dielectric resonator. The magnetic decay rates reaches 40 near $\lambda = 1540$ nm and is 4 times higher than the electric decay rates.

Multipolar resonances have not been considered for the enhancement of radiative decay rates using metallic nanoantennas because they have high losses, and thus do not radiate efficiently in the far-field. However, the situation is different with

dielectrics: negligible ohmic losses mean that the electromagnetic energy emitted by the dipole source can be stored in multipole Mie resonances with higher quality factors before being fully radiated in the far-field. The drawback is a selective spectral window (e.g. approx. 30 nm full-width half-maximum (FWHM) for the magnetic quadrupole resonance in the longitudinal case here) which would be inadequate for the homogeneously broadened fluorescence spectra of organic dyes at room temperature, but matches the narrow emission bands of lanthanide ions such as trivalent erbium at 1540 nm.

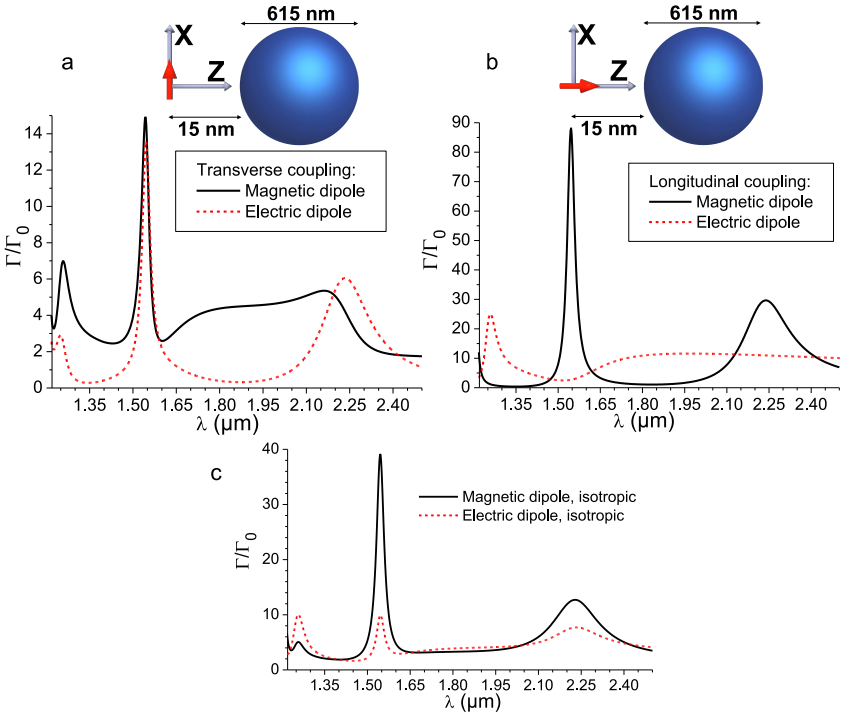

Figure 3.6: Normalized decay rates Γ/Γ_0, as a function of the wavelength, for an emitter placed 15 nm away from the surface of a 615 nm diameter Si sphere. (a) Transverse coupling, (b) longitudinal coupling, (c) isotropic averaged values over dipole orientations.

3.1.3.3 Si dimer embedded in a glass matrix

Mie magnetic resonances require a high index contrast that is not always compatible with experimental requirements. If the lanthanide ions must be hosted in a solid environment, e.g. silica, the decrease of the refractive index contrast will spoil the magnetic response of the dielectric antenna. In low refractive index contrasts, magnetic emission can still be promoted for most dipole orientations by using a dielectric nanogap antenna, i.e. a dimer of spheres made of silicon, and by considering higher order multipolar resonances with higher quality factors. Figure 3.7 shows the radiative decay rates calculated using the GMT when a magnetic dipole emitter

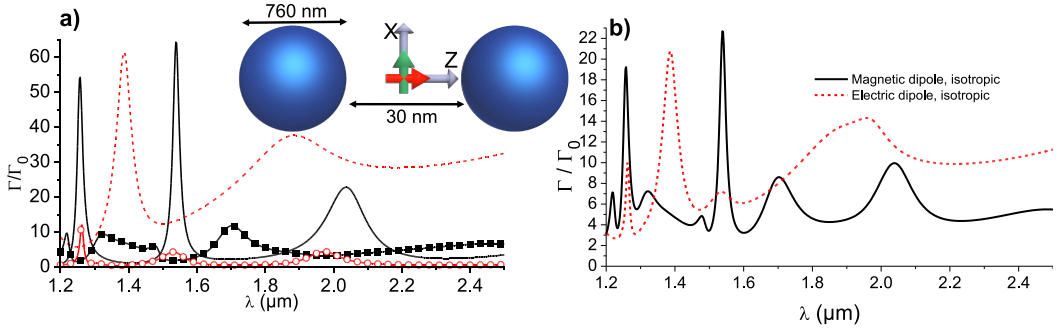

Figure 3.7: Normalized decay rates for a dimer of Si spheres, diameter 760 nm, nanogap length 30 nm, embedded in a dielectric background of refractive index n = 1.45. (a) Longitudinal coupling: (full black line) magnetic dipole, (dashed red line) electric dipole. Transverse coupling: (full black squares) magnetic dipole, (open red circles) electric dipole. Inset: sketch of the dimer configuration. The red and green arrows indicate the dipole orientation in longitudinal and transverse coupling, respectively. (b) Isotropic averages: (full black line) magnetic dipole, (dashed red line) electric dipole.

is located in the centre of a 30 nm nanogap separating two 760 nm diameter silicon spheres placed in a silica host (n=1.45). In this configuration, the longitudinal magnetic dipole is resonant with the octupoles of the particles ($n = 3$ in the GMM formalism) at $\lambda = 1.538$ μm. The normalized decay rate reaches a peak of 64.5 with a 24 nm FWHM for the magnetic emitter, while the electric emitter decay rate is enhanced by 14.6 (both values are taken in longitudinal coupling at $\lambda = 1.538$ μm). For transverse coupling configuration, both electric and magnetic decay rates are weakly enhanced (4.19 for an electric dipole emitter and 1.91 for a magnetic dipole emitter at $\lambda = 1.538$ μm). The isotropic averaged values at this wavelength are 22.7 and 7.18 for the magnetic and electric dipolar emitters, respectively.

In conclusion, subwavelength-sized particles made of lossless, high-index materials (typically semiconductors for a photon energy below their band gap) can be used to redistribute the transition rate probabilities of nearby quantum emitters that present both ED and MD type transitions, such as lanthanide ions in the visible and near infra-red bands. The process relies on the magnetic dipoles and multipoles created within the particles, albeit they are made of non-magnetic ($\mu_r = 1$) materials. In longitudinal coupling, the modification of the LDOS can promote one type of electromagnetic transition by around two orders of magnitude, while keeping the other nearly unchanged.

3.2 Using induced dipoles for enhancing emission directivity

The aim of this section is to study how a nearby spherical nanoparticle modifies the angular distribution of light emitted by an ED emitter. In particular, we provide a thorough study of the relative phase between the source dipole and the dipole that is induced in the particle. We emphasize that this relative phase must take into account the optical path between the emitter and the particle in addition to the polarizability of the particle. We show that when the phase difference between the exciting and induced dipoles is strictly equal to π, an equal part of the energy is radiated into each of the half spaces surrounding the emitter (the separation plane being perpendicular to the axis containing the dipoles). We then explain why a dipolar metallic particle placed nearby an electric dipole emitter cannot efficiently collect the radiation of the emitter.

We then study how dielectric particles of moderate- to high-refractive index influence the radiation pattern of an electric dipole. We show that, contrary to metallic particles, and thanks to the induced magnetic dipoles of such particles (introduced in section 1.1.2), they are not limitated to the role of reflectors when placed nearby the emitter. Finally we cast the near-field "Kerker conditions" that allow such particles to behave as either good collectors, or good reflectors, when coupled with an electric dipole, within a dipole approximation. We will then show that spheres made of a moderately high refractive index ($n = 2.45$) allow to reach even higher directivity gains, because they simultaneously support simultaneously significant induced electric and magnetic dipoles and quadripoles.

3.2.1 A Canonical case: single particle metallic antenna

In this section we study the effect of a nearby metallic resonator on the radiation diagram of an electric dipole. In order to illustrate our reasoning, we use a silver sphere. We thus consider an electric dipole emitter transversely coupled to a silver sphere 80 nm in diameter. The radiation patterns in figure 3.8 b and d, which are reconstructed with the rigorous GMT (multipole order $n_{\max} = 30$), show the drastic modification of the radiation directionality with a minute modification of only 10 nm in the distance between the emitter and the metallic surface of a 80 nm diameter silver sphere. When the emitter is placed at 9 nm from the surface of the sphere, we observe that the emission is strongly reflected by the sphere towards the $-x$ direction; if the emitter is displaced 10 nm away from the particle, the radiation diagram appears to be symmetric with respect to the origin, even though the electromagnetic environment of the emitter is highly asymmetric.

These results are of crucial importance for optical antenna applications and we now aim to explain, with an analytical model, the physical mechanisms involved in this high sensitivity of the emission directivity on the position of the emitter. Therefore, we focus on the interaction between a single metallic particle and an electric dipole emitter, and we only consider the transverse coupling geometry, which pro-

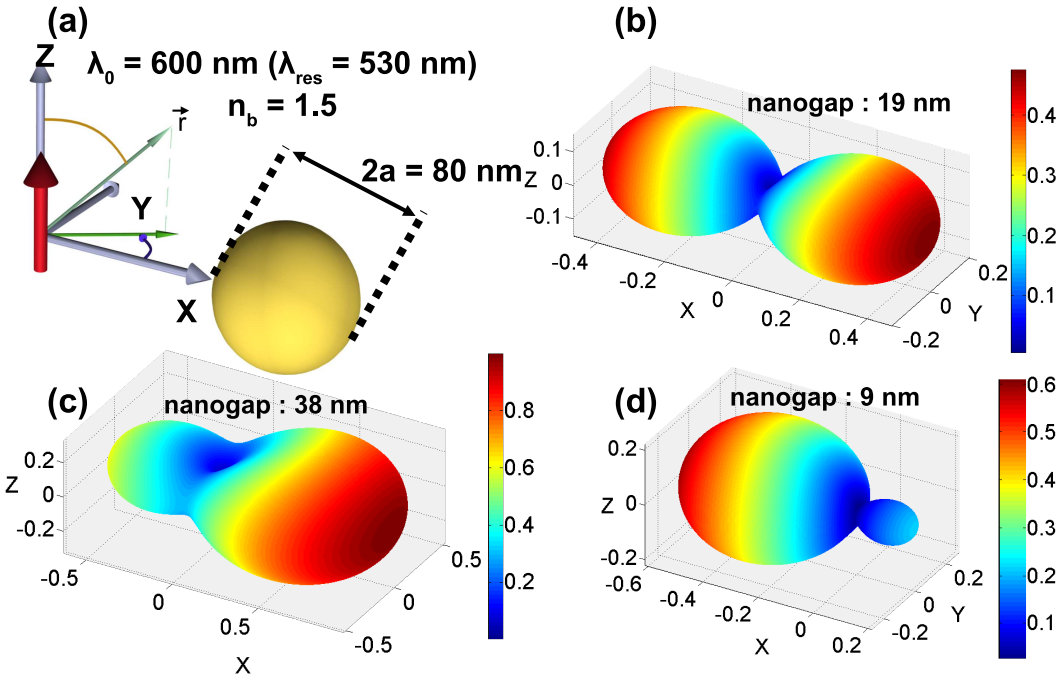

Figure 3.8: (a) An electric dipole emitter oriented along the z-axis is coupled to a silver sphere (radius $a = 40$ nm) whose center is at a distance $d = d_{\text{gap}} + a$ along the x-axis. (b-d) Radiation diagrams at $\lambda_0 = 600$ nm when the nanogap d_{gap} is (b) 19 nm, (c) 38 nm, (d) 9 nm.

vides significant emission directionality. We make the assumption that the response of the metallic sphere can be characterized by its induced dipole; the qualitative reflecting/collecting properties of the resonator are well described within this dipole approximation [Rolly 2011a]. In order to accurately compute the fluorescence decay rates, for instance, one generally requires to take into account higher order multipole terms; but for lossy metals (which is always the case in optics), multipoles mainly dissipate energy by Joule effect and do not radiate significantly into the far-field [Mertens 2007], hence they only have a minor effect on the radiation diagram of the antenna.

We orient the emitter along the z-axis ($\mathbf{p}_{\text{em}} = \hat{\mathbf{z}}$) and place the center of the metallic sphere at a distance d along the x-axis (see figure 3.8a). The antenna is embedded in a surrounding dielectric matrix with refractive index $n_b = 1.5$. We recall that the excitation field produced by the electric dipole emitter at the position of the metallic sphere can be cast 1.2:

$$\begin{aligned}\mathbf{E}_{\text{inc}}(d\hat{\mathbf{x}}) &= \frac{e^{ikd}}{4\pi\varepsilon_m\varepsilon_0 d^3}\left[k^2d^2(\hat{\mathbf{x}}\times\mathbf{p}_{\text{em}})\times\hat{\mathbf{x}} + (1-ikd)(3(\hat{\mathbf{x}}\cdot\mathbf{p}_{\text{em}})\hat{\mathbf{x}} - \mathbf{p}_{\text{em}})\right] \\ &= -\frac{e^{ikd}}{4\pi\varepsilon_m\varepsilon_0 d^3}(1-ikd-k^2d^2)\hat{\mathbf{z}} \end{aligned} \tag{3.7}$$

and the induced dipolar moment in the sphere is thus:

$$\mathbf{p}_{\text{in}} = -\alpha \frac{e^{ikd}}{4\pi d^3}(1 - ikd - k^2d^2)\hat{\mathbf{z}},$$

where the electric dipole polarizability α of the metallic sphere is computed using the Mie theory.

In order to determine the influence of the induced dipole moment of the metallic nanoparticle on the emission pattern of the emitter, we cast for $\cos\varphi > 0$ and $r \gg d$, the Poynting vector $\mathbf{P}$ of the field emitted by two transversally-coupled dipoles (denoted $\mathbf{p}_1 = p_1\hat{\mathbf{z}}$ and $\mathbf{p}_2 = p_2\hat{\mathbf{z}}$), and then add the Poynting vector symmetric with respect to the origin [Bonod 2010]:

$$\begin{aligned}
\mathbf{P}(r,\theta,\varphi) &= \frac{\omega^3 k}{32\pi^2\varepsilon_0 c^2 r^2}\left[|p_1| + |p_2| + 2\Re(p_1 p_2^* \mathrm{e}^{ikd\sin\theta\cos\varphi})\right] \\
\mathbf{\Delta P}(r,\theta,\varphi) &= \mathbf{P}(r,\theta,\varphi) + \mathbf{P}(r,\pi-\theta,\pi+\varphi) \\
&= \frac{\omega^3 k|p_1||p_2|}{8\pi^2\varepsilon_0 c^2 r^2}\left\{\sin\phi\sin[kd\sin\theta\cos\varphi]\right\}\sin^2\theta\,\mathbf{e_r}
\end{aligned}$$

where $\phi = \arg(p_1/p_2)$ is the relative phase between the two dipoles. This expression confirms that for small kd, the directivity is directly linked to the sign of $\sin(\phi)$, i.e. to the capacitive or inductive behavior of the dipolar metallic particle [Li 2007]. For emissions along the x-axis, $\sin\theta = \cos\varphi = 1$, and the last expression simplifies to:

$$\mathbf{\Delta P}(x,d) = \frac{\omega^3 k|p_1||p_2|}{8\pi^2\varepsilon_0 c^2 x^2}\sin\phi\sin(kd)\widehat{\mathbf{x}}$$

If the relative phase, ϕ, between the two dipoles was simply equal to kd as far-field reasoning would suggest, this last expression would predict that the collector/reflector behavior of the nanoparticle oscillates with separation distance as $\sin^2(kd)$. In this case, the strong changes in emission directivity for minute distance variations observed in Fig. (3.8) would remain unexplained. However, the phase difference, ϕ, between the emitter ($\mathbf{p}_{\text{em}}\cdot\hat{\mathbf{z}} = 1$) and the induced dipole ($\mathbf{p}_{\text{in}}\cdot\hat{\mathbf{z}} = -\alpha\frac{e^{ikd}}{4\pi d^3}(1 - ikd - k^2d^2)$) is a non-linear function of kd:

$$\phi\,(kd) \equiv \arg\left(\frac{\mathbf{p}_{\text{in}}\cdot\hat{\mathbf{z}}}{\mathbf{p}_{\text{em}}\cdot\hat{\mathbf{z}}}\right) = \arg\left[-\alpha e^{ikd}(1 - ikd - k^2d^2)\right]$$

The phase due to the distance between the dipoles is:

$$\phi_d \equiv \phi - \arg(\alpha) = \arg\left[-e^{ikd}(1 - ikd - k^2d^2)\right] \tag{3.8}$$

Two different terms determine ϕ_d: the well known propagative or 'far-field' phase term, kd, in the exponential, and the phase of the dipolar field term (*i.e.* the argument of $k^2d^2 + ikd - 1$). For small distances, *i.e.* $kd \leq \pi/4$, the distance dependent phase shift is dominated by the dipolar contribution (see figure 3.9). When $kd \to 0$, $\phi_d \to \pi$; this is the expected phase difference for a near-field electrostatic interaction dominated by the $1/d^3$ term in Eq.(E.7). Consequently, $\sin\phi \to -\sin[\arg(\alpha)]$ which

is negative since $0 \leq \arg(\alpha) \leq \pi$ for passive materials, and thus $\triangle \mathbf{P} < 0$, meaning that the particle behaves as a reflector. In other words, the directivity property of an electric dipolar particle cannot be reversed by modifying its size or shape when $kd \to 0$: it can only act as a reflector.

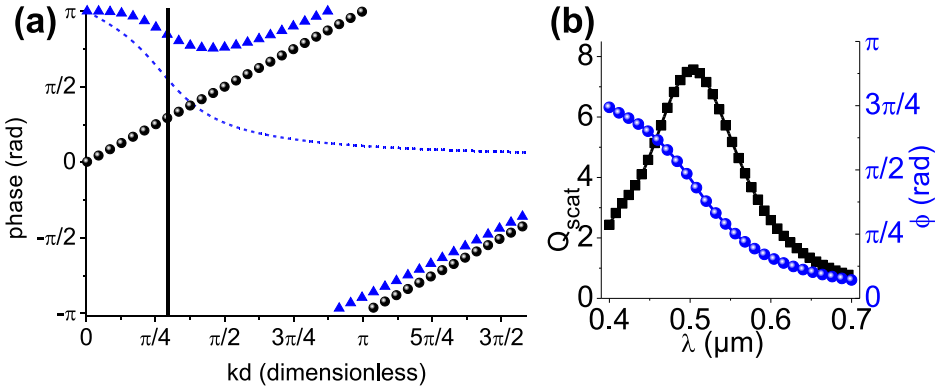

Figure 3.9: (a) (blue triangles) ϕ_d for an emitter transversely coupled to a spherical scatterer as a function of kd, (black circles) far-field term contribution, (blue dashed line) "dipolar" contribution. Vertical line marks the $kd = 0.565$ abscissa. (b) (Circles, left scale) Polarizability phase, $\mathrm{Arg}(\alpha)$, and (Squares, right scale) scattering efficiency, $Q_{\mathrm{scat}} = \sigma_s/\pi a^2$, of a 50 nm diameter silver sphere, both as a function of the vacuum wavelength.

Let us now discuss the situation where kd is small but not vanishing. The phase contribution from the dipolar field term decreases rapidly with respect to kd while the far-field term increases linearly. Consequently, for small distances, ϕ_d decreases with respect to kd. One can see in Fig. (3.9) that a minimum of $\phi_d \simeq 3\pi/4$ occurs at $kd = \sqrt{2}$. This means that the particle can behave as a collector, $\mathbf{\Delta P} > 0$, provided that $\phi_\alpha \equiv \arg(\alpha) < \pi/4$. This condition is generally fulfilled for wavelengths significantly larger than the particle plasmon resonance frequency (see figure 3.9b).

This combination ($kd \simeq \sqrt{2}$, $\phi_\alpha < \pi/4$) is the only possibility for a transversally-coupled metallic particle to act as a collector at "small" distances ($kd < 3\pi/4$). In other words, for a 'large' metallic particle ($\arg(\alpha) > \pi/4$) at small distances ($kd < 3\pi/4$), the condition $\mathbf{\Delta P} = 0$ cannot be achieved and thus the directional property cannot be reversed by varying the phase of the dipolar term (the particle can only be a reflector). In such a case, using the separation distance to tune from a reflecting to a collecting behavior of the nanoparticle requires working with larger separations, for which the far-field term kd of Eq.(3.8) dominates. In practice, Fig. (3.9.a) demonstrates a clear transition between the electrostatic approximation ($kd \to 0$, $\phi_d = \pi$) and the far-field approximation (circles in Fig. (3.9)). In this transition region, the dipolar field phase term strongly influences the antenna behavior around $kd = \pi/4$ where its slope versus kd is highest (dashed blue line on Fig. 3.9).

Using this dipolar model, we are able to explain the surprising phenomena shown

in Fig. (3.8) using rigorous generalized Mie theory. With $\lambda_{em} = 600$ nm and $d = 36$ nm, we have $kd \cong 0.565$, which gives $\phi_d = 3.01$rad (see the vertical line in Fig.3.9). The phase of the polarizability of the silver particle at this wavelength is 0.13rad (see inset). The total relative phase between the exciting and induced dipoles is then $\phi = 3.14$ rad $\cong \pi$ rad which results in $\sin\phi \cong 0$, *i.e.* a symmetric emission pattern ($\Delta\mathbf{P} = 0$). For $d < 36$ nm, ϕ_d increases resulting in $\sin\phi < 0$, thus explaining the reflective behavior of the sphere placed at a center-to center distance of 30 nm. Respectively, a slight increase of d results in $\sin\phi > 0$ and a collector behavior for the sphere.

3.2.2 Using both electric and magnetic Mie resonances of dielectric particles

We have seen in the last section why electric dipole resonators are not the best candidates for acting as light collectors. In the visible spectrum, metals present losses that prevent their electric quadrupoles to scatter lignificant light; and they do not present any significant magnetic resonances for spherical shapes. In order to reach high directivity gains using spherical particles, one thus requires to use an array of collectors, thus increasing the antenna size. Lossless dielectrics, on the other hand, present significant magnetic resonances when their size and refractive index are high enough. In this section, we will show that using the combined electric and magnetic dipole resonances of a sub-wavelength sphere made of a lossless dielectric of high refractive index ($n_s \approx 3.5$), allows one to design a compact collector. We will also cast the conditions for the scatterer to be a good collector, or reflector, of an electric dipole radiation.

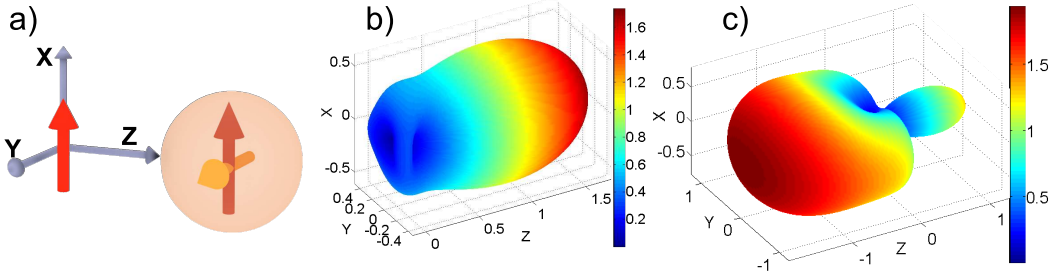

Figure 3.10: (a) Sketch of the configuration. (b,c) Radiation diagrams for a 85 nm radius GaP sphere behaving as (b) a collector, distance to the emitter 10 nm and (c) a reflector, distance to the emitter 100 nm. The electric dipole emitter is oriented along the x axis, the sphere is placed in the +z direction. The refractive index of the embedding medium is n = 1.45 and the emission wavelength in vacuum is $\lambda = 550$ nm

We thus study the coupling of an electric dipole to a sub-wavelength dielectric resonator, wherein we can make use of both the induced electric and magnetic dipoles. We will show that the coherent scattering of both induced dipoles can

increase the directivity of the emission as compared to the case of a single induced electric dipole. In the induced (electric and magnetic) dipole approximation, the Poynting vector resulting from the coupling of an x-oriented electric dipole, to a dielectric sphere placed at a center-to-center distance d on the z axis (see figure 3.10a), can be cast: (see demonstration in appendix E.3)

$$\begin{aligned}
\gamma_e &\equiv -e^{ikd}\frac{a^3}{d^3}(1-ikd-k^2d^2) \\
\gamma_m &\equiv e^{ikd}\frac{a^3}{d^3}(ikd+k^2d^2) \\
\mathbf{P}(x,y,z) &= \frac{\omega k^3}{32\pi^2 r^2 \varepsilon_0 \varepsilon_m}\Big\{(1-x^2)|1+\gamma_e\tilde{\alpha}e^{-ikdz}|^2+(1-y^2)|\gamma_m\tilde{\beta}|^2 \\
&\quad +2z\Re[\gamma_m^*\tilde{\beta}^*e^{ikdz}(1+\gamma_e\tilde{\alpha}e^{-ikdz})]\Big\}\hat{\mathbf{r}},
\end{aligned} \tag{3.9}$$

with $\tilde{\alpha}$ and $\tilde{\beta}$ the electric and magnetic dimensionless polarizabilities, and (x,y,z) the Cartesian coordinates of the unit radial vector $\hat{\mathbf{r}}$. γ_e and γ_m are the coupling factors of the emitter with the induced electric and magnetic dipoles of the sphere, respectively.

In equation 3.9, the first term in the brackets on the right-hand side results from the emission and interference in the far field region between the two electric dipoles, both being oriented along the x axis (see figure 3.10a). The second term originates from the emission of the magnetic induced dipole (oriented on the y axis), while the last term corresponds to the interference between the induced magnetic dipole and the two electric dipoles. This latter term is null in the $z=0$ plane since the electric and magnetic fields produced by the magnetic dipole on the one hand, and the two electric dipoles on the other hand, are orthogonal in this plane.

The collector behavior of the dielectric antenna will usually be optimized when the Poynting vector $\mathbf{P}(0,0,-r)$ directed towards the $-z$ direction is minimized :

$$\begin{aligned}
\mathbf{P}(0,0,-r) &\cong \frac{\omega}{32\pi^2\varepsilon_m\varepsilon_0 r^2}k^3(|\gamma_m\tilde{\beta}|^2+|1+\gamma_e\tilde{\alpha}e^{ikd}|^2 \\
&\quad -2|\gamma_m\tilde{\beta}||1+\gamma_e\tilde{\alpha}e^{ikd}|)\hat{\mathbf{r}}
\end{aligned}$$

which occurs when the following condition is satisfied:

$$e^{-ikd}+\gamma_e\tilde{\alpha}=\gamma_m\tilde{\beta}\rightarrow\mathbf{P}(0,0,-r)=0 \tag{3.10}$$

This explains why a maximum of the collecting efficiency can be observed when the 170 nm diameter GaP dielectric antenna is placed at 10 nm from the emitter : $\arg(\gamma_m\tilde{\beta})=-0.65\pi$, $\arg(e^{-ikd}+\gamma_e\tilde{\alpha})=-0.66\pi$, $|\gamma_m\tilde{\beta}|=0.972$, $|1+\gamma_e\tilde{\alpha}e^{ikd}|=1.42$. While the condition of equation 3.10 on the modulus of the quantities is not fully verified, the condition on the phases is well satisfied, and the radiation pattern in Fig.3.10(a) shows a sharp minimum in the backward direction, which disappears if the induced magnetic dipole is not radiating [Rolly 2012c]. The condition in Eq.3.10 is that of a total destructive interference of the fields radiated by the two

electric dipoles and the magnetic dipole in the $-z$ direction. In the case of plane wave scattering, the zero backscattering condition is called the first Kerker condition [Kerker 1983, Gomez-Medina 2011]. In the present caseof a local excitation of the sphere, the backward emission originating from the emitter must be cancelled, which is not the case when considering plane wave excitations. Canceling the forward scattering would require the fulfillment of the condition:

$$e^{ikd} + \gamma_e \tilde{\alpha} \cong -\gamma_m \tilde{\beta} \rightarrow \mathbf{P}(0, 0, +r) = 0, \tag{3.11}$$

This condition is the analogue, for the case of a localized excitation, of the generalized second Kerker condition (the condition of minimal forward-scattered power – compared to the total scattered power – when the sphere is illuminated by a plane wave)[Gomez-Medina 2011]. This condition (Eq. 3.11) is not satisfied here, indeed, we see in Fig.3.10(b) that the forward scattering is not eliminated. Nevertheless, the GaP spherical antenna does move from a collector behavior to a reflector behavior, when the distance to the emitter is increased from 10 to 100 nm.

3.2.3 Using combined dipole and quadripole resonances of dielectrics

In this section, we show that the use of moderately high refractive index, lossless dielectric materials, as collectors or reflectors of the radiation coming from an electric dipole, is a promising alternative to the use of metals and high refractive index dielectrics. We consider a moderate refractive index ($n_s = 2.45$) of the sphere, in order to obtain a regime where the Mie coefficients of the sphere (and therefore the polarizabilities) corresponding to the electric and magnetic dipoles and quadripoles, are simultaneously non-negligible in a given range of frequencies, *i.e.* approximately between the smallest and largest frequencies of those resonances (see below, figure 3.11e). If the refractive index of the sphere is too high, then those resonances become narrower, and they end up being well separated for a refractive index of 4 and a radius of 200 nm, as shown in figure 1.5 in introduction. In addition, for fabrication purposes, moderate refractive index materials are much more common than materials with $n_s \geq 3$ (as in the last section) for instance.

This theoretical study is backed with experimental data, the experiment was carried out in the GHz frequency regime, in an anechoic chamber at the CCRM, Marseille (see figure 3.11a), by our colleagues Redha Abdeddaim and Jean-Michel Geffrin. We couple an electric dipole emitter with a single dielectric sphere, made of an Eccostock HIK (Emmerson & Cumming) material of permittivity 6 (refractive index $n \approx 2.45$), presenting low losses ($\tan\delta \leq 0.02$). The diameter of the sphere is $2a = 19$ mm and we see, (figure 3.11e) that its first four Mie coefficients simultaneously have significant values in the frequency band $\approx 8 - 10$ GHz. As in the two last sections, we consider a transverse coupling in order to be able to observe significant enhancements of the directivity of the emission. The experimental emitter is a two-arm electric dipole emitter (see the photography, figure 3.11b). By controling the emitter-to-particle distance, d, at a subwavelength scale, we report

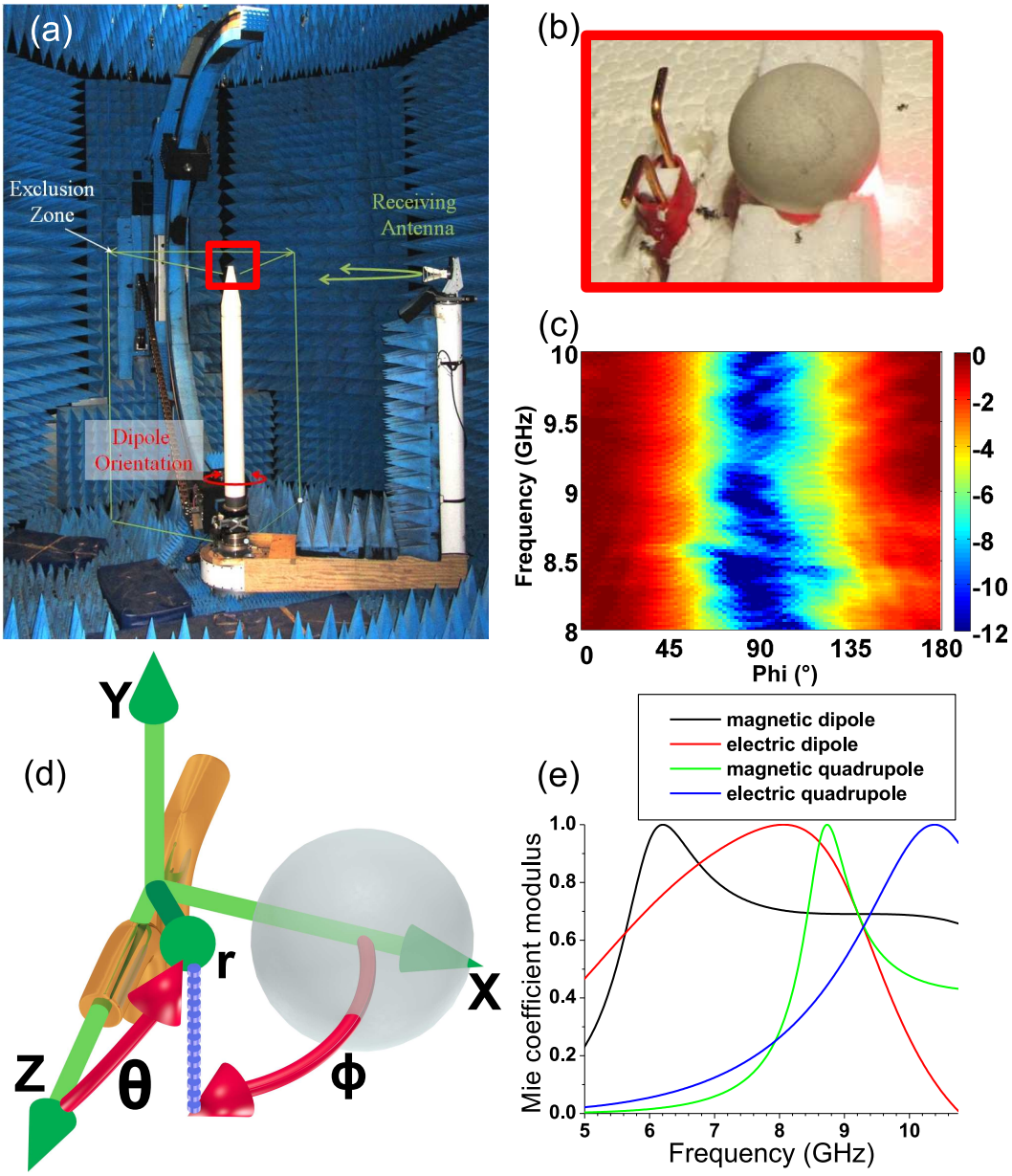

Figure 3.11: (a) Photography of the experiment in the anechoic chamber: the dipole-sphere antenna is placed on a polystyrene mast at the center of an anechoic chamber. The receiver antenna (ARA DRG 118) can rotate around the Oy axis (see Fig 1.d) except in an exclusion zone in the angle range $[-130, 130]$ due to the presence of the vertical arch. (b) Close-up of the dipole-sphere antenna and of the polystyrene holders. (c) Norm of the electric field emitted by the isolated dipole antenna as a function of the frequency and angle ϕ in the E-plane (Oxz plane) in dB. At each frequency, the field is normalized by its maximum in the E-plane. (d) Sketch of the experiment with spherical coordinate axes and angles. (e) Norm of the Mie coefficients $|c_j^{\mathrm{e(m)}}|$ with respect to frequency in GHz. Black line: magnetic dipole $|c_1^{\mathrm{m}}|$; red line: electric dipole $|c_1^{\mathrm{e}}|$; green line: magnetic quadrupole $|c_2^{\mathrm{m}}|$; blue line: electric quadrupole $|c_2^{\mathrm{e}}|$.

on the possibility to choose the emission direction by tuning the frequency from 8.7 GHz to 9.74 GHz.

The anechoic chamber of CCRM, Marseille, is dedicated to amplitude and phase measurements of the electric fields with a receiver antenna rotating along a circular arm 4 m in diameter, centered on the feed [Geffrin 2012]. Each arm of the emitter is 9 mm long, which results in a total length smaller than the wavelength, even at the highest operating frequency. The characterization of the dipole in its E-plane (Fig. 3.11c) shows a classical dipole-like radiation pattern, with comparable front and backward radiated amplitude (respectively 0° and 180°), and negligible emission in the 90° direction. The distance between the dipole and the sphere is controled at a submillimeter scale, via an expanded polystyrene holder (which is equivalent to air at the operating frequencies – see Fig.3.11a-b). Measurements have been performed with emitter-to-sphere distances of 5, 10 and 20 mm and frequencies ranging from 8 to 10 GHz with a step of 20 MHz, which corresponds to a total of 300 emission pattern measurements. The squared modulus of the electric field in the E-plane ($\theta = 0$) is displayed in Fig. 3.12 with respect to the frequency and angle ϕ ranging from to 0 to 180°, *i.e.* in a half plane containing one emitter arm. At every frequency, the intensity is normalized by the maximum measured in the [0;180°] range, and the results are displayed in dB. It can be observed that the radiation pattern is highly sensitive to a modification of the emitter-to-particle distance, at a scale much smaller than the emission wavelength. Importantly, we observe that this Mie antenna can either emit in forward (around 8.75 GHz) or backward (around 9.5 GHz) direction for a 10 mm distance.

In order to demonstrate the essential contribution of the first four Mie coefficients of the sphere, in this tunability of the emission directivity, we now derive the theoretical formula of the far-field of the antenna. For this purpose, the fields are derived in the spherical vector basis, $[\hat{\mathbf{e}}_r, \hat{\mathbf{e}}_\theta, \hat{\mathbf{e}}_\phi]$. The dipole emitter is considered to lie on the $\hat{\mathbf{z}}$ axis and placed at the origin of the coordinate system; the particle is placed at a distance d on the $\hat{\mathbf{x}}$ axis, $\mathbf{u}_1 = d\hat{\mathbf{x}}$ (see figure 3.11d) The normalized far-field irradiance can be cast (see appendix E.4):

$$
\begin{aligned}
I(\theta,\phi) \quad = \quad & \Big| \sin(\theta)\hat{\mathbf{e}_\theta} \\
& + e^{i\Phi}\gamma_1^e\tilde{\alpha}_1^e \sin(\theta)\hat{\mathbf{e}_\theta} \\
& + e^{i\Phi}\gamma_1^m\tilde{\alpha}_1^m(\cos(\phi)\hat{\mathbf{e}_\theta} - \sin(\phi)\cos(\theta)\hat{\mathbf{e}_\phi}) \\
& + e^{i\Phi}\gamma_2^e\tilde{\alpha}_2^e(\cos(\phi)\cos(2\theta)\hat{\mathbf{e}_\theta} - \sin(\phi)\cos(\theta)\hat{\mathbf{e}_\phi}) \\
& + e^{i\Phi}\gamma_2^m\tilde{\alpha}_2^m(\cos(2\phi)\sin(\theta)\hat{\mathbf{e}_\theta} - \frac{\sin(2\phi)\sin(2\theta)}{2}\hat{\mathbf{e}_\phi}) \Big|^2
\end{aligned}
\tag{3.12}
$$

where $e^{i\Phi} \equiv \exp(-ikd\sin(\theta)\cos(\varphi))$ is a far-field phase shift, and each subsequent line stands for the field produced by the emitter, and the induced electric dipole, magnetic dipole, electric quadrupole, and magnetic quadrupole respectively. The coupling coefficients between the emitter and the first 2 electric and magnetic modes

of the sphere are written:

$$\begin{aligned}
\gamma_1^e &\equiv e^{ikd}(1-ikd-k^2d^2)/d^3 \\
\gamma_1^m &\equiv e^{ikd}(ikd+k^2d^2)/d^3 \\
\gamma_2^e &\equiv e^{ikd}(k^3d^3+3ik^2d^2-6kd-6i)\frac{5}{3kd^4} \\
\gamma_2^m &\equiv e^{ikd}(k^2d^2+3ikd-3)\frac{5}{3d^3}\ .
\end{aligned}$$

We readily verify that the induced dipoles and quadripoles assumption is verified, by plotting the electric field in the E-plane when using both equation 3.12, or a more accurate calculation based on the GMT with maximal multipolarity index $n_{\max} = 20$ (figure 3.12, middle and bottom rows). While the actual values somewhat differ at some points, one can see that all of the features of the bottom row (GMT, $n_{\max} = 20$) are reproduced in the quadripole assumption, in the middle row (obtained from equation 3.12).

The measured intensities are also displayed in figure 3.12 (top row) and a good agreement between theory and experiments can be observed for the three emitter-to-particle distances, apart from a small frequency shift, that is likely due to an imperfect knowledge of the permittivity of the sphere (the real part is given at +/- 5% and the imaginary part is set to 0 in the model) and to the spatial extension of the source – the theoretical expression considering a point dipole. Both the model and the experiments indicate that, for a 10 mm gap, the privileged direction of emission of the antenna can be controlled efficiently by tuning the emission frequency. This feature is highlighted in figures 3.13ab, where the data at the selected frequencies of 8.7 GHz and 9.74 GHz are plotted in polar coordinates. Moreover, the theory predicts directivity values of 7.01 dBi at 8.66 GHz and 5.17 dBi at 9.58 GHz in the front- and backward directions respectively. We also point out that the electric field measured in the privileged direction is 3.4 and 2.4 times stronger than without the sphere, respectively, at 8.7 GHz and 9.74 GHz.

The theoretical emission patterns are plotted in figure 3.13c at f=8.7 GHz, when considering dipoles or quadrupoles only (full black and red lines respectively). We observe that neither dipole nor quadrupole excitations taken alone suffice to explain the directivity. When the sphere behaves as induced dipoles only, light is emitted towards the backward direction while it is emitted in the forward direction with a low gain in directivity when the sphere behaves as induced quadrupoles. A similar filtering method in figure 3.13d shows that neither electric nor magnetic multipoles, taken separately, allow to obtain a forward directivity and gain as high as obtained with the full equation 3.12. Comparison with GMT with $n_{\max} = 20$ reveals the high accuracy of the quadrupolar model in this case.

The emission pattern thus results from an efficient coupling between the electric and magnetic modes, of dipole and quadrupole orders, allowed by the broad Mie resonances displayed in figure 3.11e. The high sensitivity of the emission pattern with respect to the emission frequency is thus explained by a strong modulation of 3 of those modes between $8-10$ GHz.

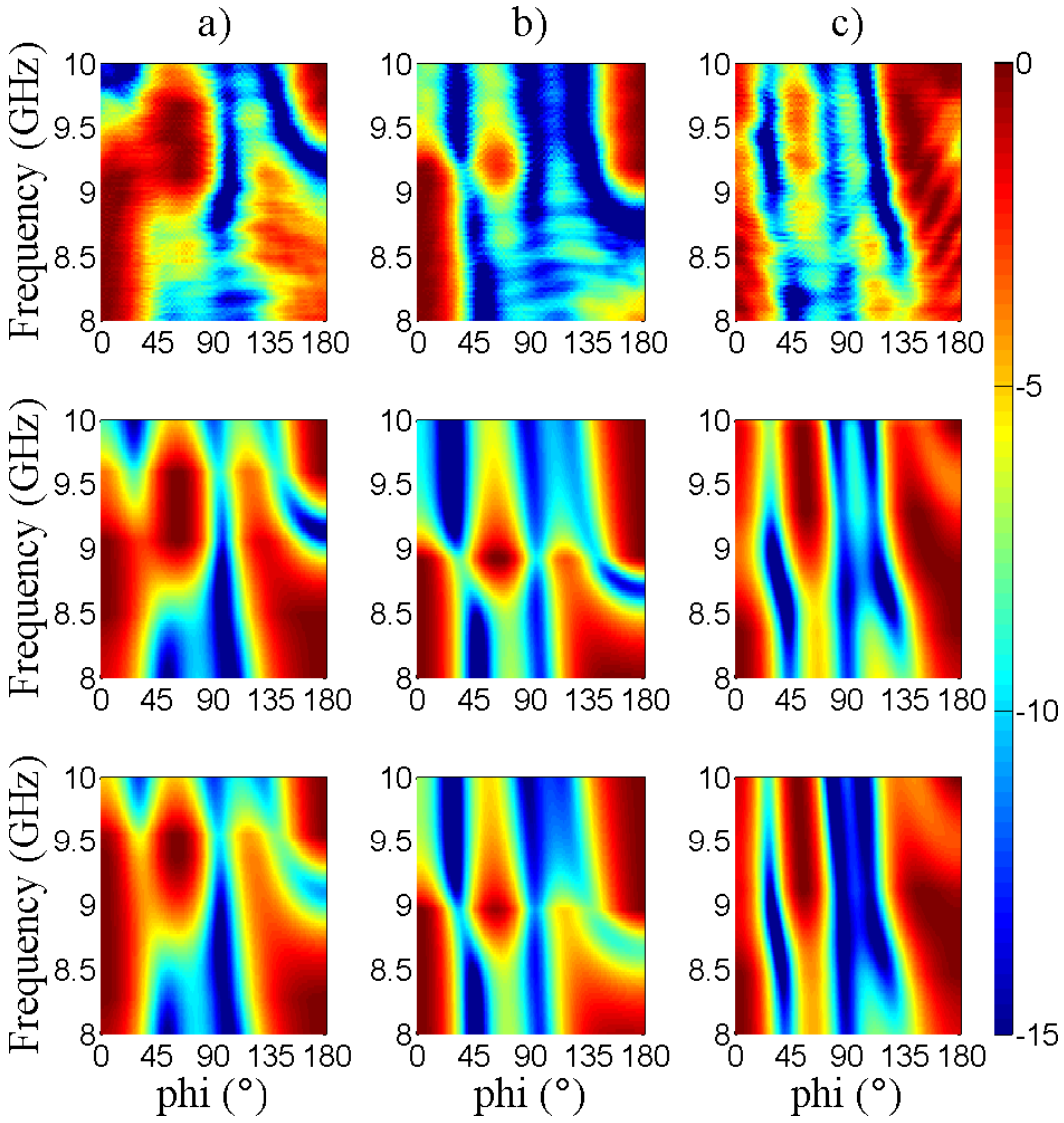

Figure 3.12: Square norm of the electric field in the E-plane, measured (top row) and simulated (middle and bottom row), as functions of the antenna receiver angle ϕ in degrees (in abscissa) and emitting frequency in GHz (in ordinate). At each frequency, the intensity is normalized by its maximum in the E-plane. The emitter-to-sphere gaps, $d - a$, are (a) 5 mm, (b) 10 mm and (c) 20 mm. The middle row is obtained from equation 3.12 while the bottom row uses Mie theory with $n_{\max} = 20$

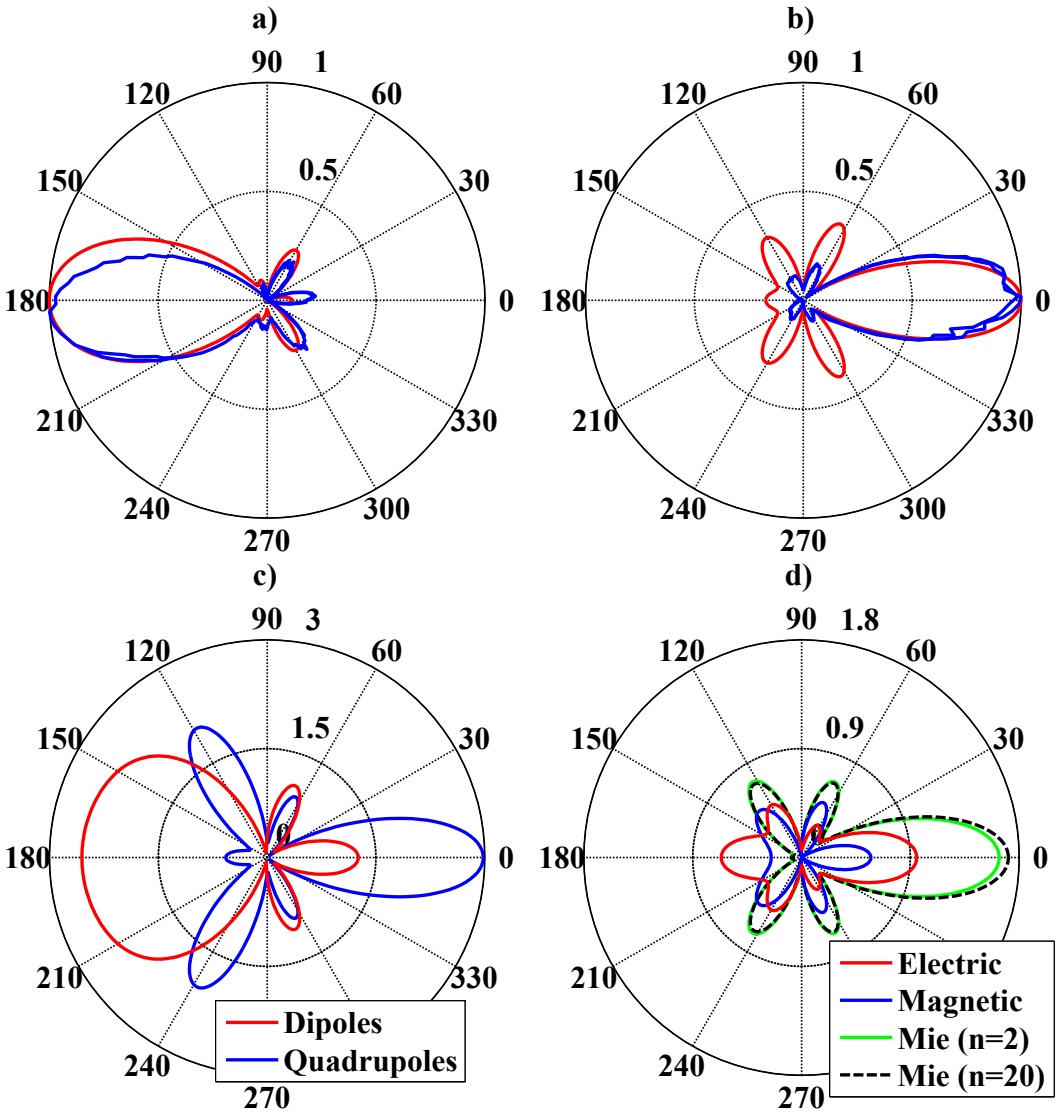

Figure 3.13: (a,b) Square norm of the total electric far-field, in the E-plane and as a function of ϕ in °, for an emitter-to-particle gap of 10 mm, (red line) simulations with maximal multipolarity order $n_{\max} = 20$ and (blue) measurements. (a) Strong back-scattering observed at 9.74 GHz, (b) strong forward-scattering observed at 8.7 GHz. (c) Emission pattern given by equation 3.12 when considering the induced dipoles (red line) or quadrupoles (blue line) only. (d) Emission pattern obtained with: the Mie theory, $n_{\max} = 20$ (dashed black line); or by using equation 3.12 and considering: the full equation (green line), electric (red line) or magnetic (blue line) dipoles and quadrupoles.

3.3 Hybrid designs: bright and directive

From a theoretical viewpoint, probably the best way to build a nanoantenna that is compact (maximal size $\approx \lambda n_b/2$), bright (radiative decay rates $\Gamma_{\text{rad}}/\Gamma_0 \geq 100$), efficient (quantum efficiency $\eta \geq 50\%$) and directive (directivity $D_{\text{dBi}} \geq 6$ dBi), all at the same time, and with a bandwidth compatible with the broadened spectral emissions at room temperature (a few tens of nm wavelength linewidth), is to assemble hybrid, metallo-dielectric antennas. Such antennas can take advantage of the high decay rate enhancements offered by relatively small metallic particles (*e.g.* using a nanogap dimer) as well as the low-losses and collection properties of moderate- or high-index dielectrics. Such "optoplasmonic" structures have a number of applications; they were theoretically studied in 2006 as Surface-Enhanced Raman scattering structures[Zou 2006], owing to the very large excitation enhancement that they can provide (theoretically, around 10^6). The studies of hybrid structures, such as the one presented below, for the decay rate enhancement and directivity increase of single emitters, dates a few years back [Devilez 2010].

We now present such a compact, bright, efficient, and directive antenna design. The antenna is composed of a GaP collector sphere, 150 nm in diameter, coupled with a quantum emitter located in the 8 nm nanogap of a silver dimer with radii 30 nm. The emission pattern of the emitter coupled to the sole dimer remains similar to that of the isolated emitter, only with increased intensity. The emitter is separated by 30 nm from the surface of the dielectric particle, and the embedding medium has a refractive index of 1.45 (Fig. 3.14(a)). Figure 3.14(b) displays the emission pattern and confirms the high directivity offered by this hybrid metallo-dielectric antenna. Figure 3.14(c) shows that the lossless magneto-electric collector permits to further enhance the radiative decay rates over a wide range of wavelengths (as compared to the isolated metallic dimer antenna, see Fig. 3.14(c)). This compact hybrid antenna exhibits a gain in directivity higher than 6 dBi, a radiative decay rate enhancement factor larger than 10^3, and a quantum efficiency above 55% over a wide range of wavelengths, with all three properties being satisfied for a 30 nm range, centered around 530 nm.

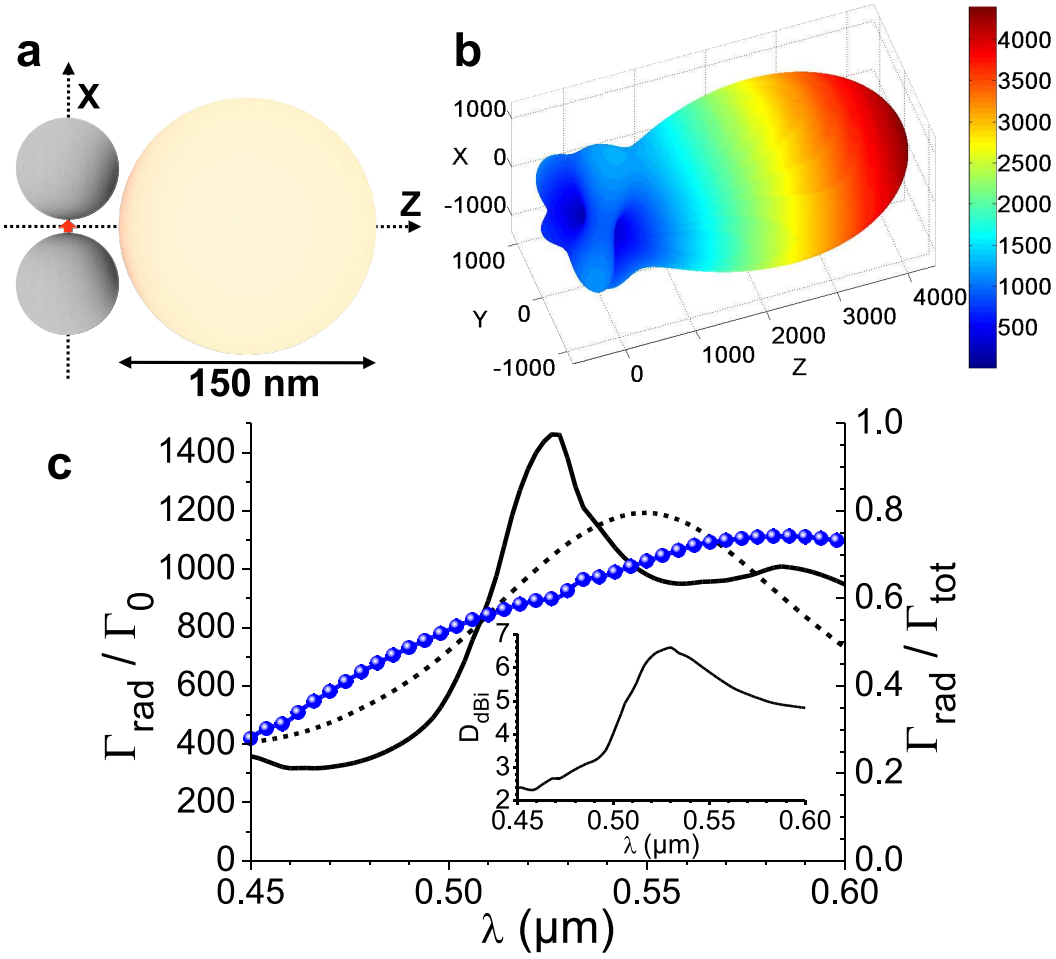

Figure 3.14: (a) Schematic of a hybrid antenna with an electric dipolar emitter longitudinally coupled to a silver dimer (particles 30 nm in radius and nanogap length of 8 nm), and transversely coupled to a GaP sphere (75 nm in radius, surface 30 nm away from the emitter). (b) Radiation diagram at the vacuum wavelength $\lambda_0 = 526$ nm, at which the decay rate enhancement is maximal. (c) (left scale) Radiative decay rate enhancement (full black line) of the hybrid nanoantenna and (dashed line) of the metallic dimer antenna alone. (Right scale, full blue circles) Quantum efficiency of the hybrid nanoantenna. (Inset) Gain in directivity of the hybrid antenna.

Chapter 4

Conclusion

"The art of concluding from experience and observation consists in evaluating probabilities, in estimating if they are high or numerous enough to constitute proof. This type of calculation is more complicated and more difficult than one might think. It demands a great sagacity generally above the power of common people. The success of charlatans, sorcerers, and alchemists – and all those who abuse public credulity – is founded on errors in this type of calculation."

Benjamin Franklin, U.S.A. polymath (1706-1790)
and Antoine Lavoisier, French chemist (1743-1794)

This thesis was aimed at finding efficient ways to enhance light-matter interactions using sub-wavelength resonators. The emission properties (decay rates, far-field radiation diagram) of emitters (atoms, molecules, dyes, quantum dots, color centres, ...) depend on their electromagnetic environment; using carefully designed sub-wavelength resonators allows to enhance those properties by orders of magnitudes, while not being restricted to the narrower resonances of larger structures.

The excitation of a fluorescent atom or molecule is often realized using a far-field illumination. In order to design adapted structures, one thus requires to have a good understanding of the individual response, and of the couplings, of the resonators when they are illuminated from the far-field. When the multipole effects are not significant in the system, induced dipole models are intuitive and convenient tools that allow to describe the structure. In chapter 2, we considered the response of optical antennas when illuminated from the far-field. We shown that an induced dipole model can successfully predict the scattering response of a simple dimer structure, well beyond the quasi-static approximation that is often associated with those models: the scattering cross-sections of a gold dimer of spheres 110 nm in diameter can be accurately calculated with such a model. The key point is to exclude quasi-static approximations of the individual polarizabilities in the one hand, and of the near-field coupling between the two scatterers on the other hand. The model yields accurate results as long as the inter-particle distance as well as the wavelength are not too small (in this case, nanogaps $\geq$ 10 nm and wavelengths $\geq$ 450 nm $\approx$ 4 times the particle diameter). Dipolar models that take into account both electric and magnetic resonances, can also be used to predict the far-field illumination response of particles more complex than spheres, like split-ring resonators; however, in this case, the polarizability tensor is not a scalar quantity, and we showed that one might have to include corrections that arise from the lack of central symmetry of the structure, even when the maximal size of the resonator is small compared to the wavelength.

However, they rely on rather strong assumptions that must be carefully verified; in the case of one-dimensional arrays of particles, we showed that they fail to predict the "leaky modes" dispersion relations, even when the inter-particle distance is equal to the radius of the scatterers.

In chapter 3, we studied the response of the antenna when it is excited by an electric of magnetic point dipole placed nearby. When the emitter is in an excited state, from which it will spontaneously decay, the rate at which it decays can be modified by its coupling to nearby structures, and this modification should, in principle, be calculated with rigorous quantum mechanical computations; but in a weak atom-field coupling regime, the decay rate can easily be calculated with a Green function formulation or a related method. Formulas of the decay rates in the GMT framework allow to compute in a fast manner the decay rates of ensembles of resonators, at the condition of knowing the individual T-matrices of the scatterers. We applied those formulas in order to cast the explicit analytical decay rate enhancements provided by single spherical resonators in an induced dipole and quadrupole assumption, in the case of an excitation consisting in either an electric or a magnetic dipole. The different couplings and resonances can be used to selectively promote either electric or magnetic dipoles placed in their neighborhood. We also proposed to use lossless dielectric particle dimers of high refractive index material in order to enhance the electric or magnetic dipole decay rates, even when the system is embedded in a polymer environment. The radiation diagram of the emitter also depends on its coupling with nearby structures. We showed that for transverse couplings and for short emitter-particle separations, the collector or reflector behavior of a single metallic resonator can be strongly dependent on the separation on a ≈ 10 nm scale. An induced dipole model allows to explain the reasons of such a sensitivity; it also explains why electric dipole resonators generally are inefficient collectors. In the case of lossless, moderate- to high- refractive index dielectrics, the situation is different; we showed that the collective electric and magnetic dipole and quadrupole resonances allowed sub-wavelength dielectric spheres to collect the radiation from an electric dipole efficiently. We also proposed a compact, bright, efficient, and directive hybrid design, the idea based on an earlier concept of combining a metallic dimer gap antenna with a dielectric particle [Devilez 2010], but the use of a high refractive material (like GaP or Si) allows a more compact design.

We collaborated with the group of Sébastien Bidault at Institut Langevin, Paris, who succeeded in fabricating DNA-templated gold nanoparticle dimers of diameter ≈ 36 nm by chemical synthesis, a bottom-up technique that is both reproducible and adapted to large production scales. Our numerical simulations of the scattering cross-sections were in well satisfactory agreement with the characterization experiments. They subsequently grafted dye molecules inside the dimer nanogap of $\approx 6 - 20$ nm, and our numerical simulations allowed to infer that the emitter can be placed at the centre of the (tunable) gap with a precision of ≈ 1 nm, a scale impossible to reach using state-of-the-art top-down fabrication techniques.

In order to make models that can better compare with experiments, substrate effects should be taken into account: free-standing systems are easier to consider theoretically, but the vast majority of the actual experiments, and potential applications, include a substrate, which effect is not always negligible. Analytical models like that of [Gozhenko 2003], but that takes into account retardation effects, would allow an accurate analytical treatment of the substrate effects. A way of including non-spherical scatterers into the GMT would also be a critical step for the domain of applicability of the formalism, and this appears to be possible [Evlyukhin 2011, Khlebtsov 2013]. Concerning the experimental prospects, the compact, hybrid designs are promising; a French Agence Nationale de la Recherche project entitled "TWINS" aiming at an experimental realization is underway, in collaboration between Institut Fresnel, Institut Langevin, and the Université de Technologie de Troyes. The monomer and dimer of high refractive index particles aimed at enhancing electric and/or magnetic dipoles, is also promised to a bright future, with potential applications in field-enhanced spectroscopy for instance [Albella 2013].

Appendix A

Multipole expansion of the fields

A.1 Multipole expansion numbers, and coefficients ordering

The multipolar basis is an infinite set of base vectors in which any arbitrary 3-dimensional vector electromagnetic field, that satisfies the Maxwell equations in a homogeneous medium, can be expressed. The basis is indexed by the multipole expansion numbers, n and m, or by a combined p index [Stout 2008, Tsang 1980]:

$$\begin{aligned} p \equiv &\quad n(n+1)+m \\ n \equiv &\quad \text{floor}(\sqrt{p}) \\ m \equiv &\quad p-n(n+1) \end{aligned}$$

The n index is called "moltipolarity order" and corresponds to the order of the expanded field in the following fashion: $n=1$ corresponds to a dipole field, $n=2$ to a quadrupole field, $n=j$ to a 2^j-pole. n can take any positive integer value, $n \in \mathbb{N}^*$, hence the infinite rank of the multipolar basis. In order to carry out the numerical computations, the multipolar basis is truncated at the order $n=n_{\max}$; the accuracy of the result generally increases with $n_{\max}$. The m index characterizes the orientation of the (n-th order) field. It can take integer values $m \in [-n, n]$. The p index thus ranges from 1 to $n_{\max}(n_{\max}+2)$. Finally, the q index is used in order to differentiate multipoles of magnetic ($q=1$ or $'m'$) and electric ($q=2$ or $'e'$) nature.

In order to produce compact matrix forms of the equations of the scattering problem, we need to adopt a convention on the way we arrange the (incoming or scattered) field coefficients, each of which is to be assigned its corresponding Vector Partial Wave. Throughout this thesis, the following order is used: when a particular maximal multipolar order $n_{\max}$ is chosen, the first $p_{\max}=n_{\max}(n_{\max}+2)$ coefficients will be the $u_{q=1,n,m}$ coefficients of the "magnetic" part of the field, the following $p_{\max}$ will be the $u_{q=2,n,m}$ – each half being ordered with increasing p. This means the coefficients start at $n=1, m=-1$ and continue with increasing m until it reaches 1, then increasing n and starting with $m=-n$ until n, the process being repeated until $n=m=n_{\max}$. When no maximal order $n_{\max}$ is chosen, the base vectors are still arranged by increasing p, and there are, formally, two sets of coefficients, one for each value of q; for matrices, there are four blocks, that correspond to $(q_1,q_2)=(1,1),\ (1,2),\ (2,1)$ and $(2,2)$ respectively.

The same order stands for the matrices' lines and columns, and for better clarity we cast below the (q,m,n) or (q_1,q_2,p_1,p_2) numbers corresponding to the coeffi-

cients of a vector $\mathbf{u}$ or a matrix $\mathbf{A}$ (p_m stands for $p_{\max}$):

$$\mathbf{u} = \begin{bmatrix} u_{q=1,n=1,m=-1} \\ u_{q=1,n=1,m=0} \\ u_{q=1,n=1,m=1} \\ u_{q=1,n=2,m=-2} \\ u_{q=1,n=2,m=-1} \\ \vdots \\ u_{q=1,n=n_{\max},m=n_{\mathrm{m}}} \\ u_{q=2,n=1,m=-1} \\ \vdots \\ u_{q=2,n=n_{\max},m=n_{\mathrm{m}}} \end{bmatrix} = \begin{bmatrix} u_{q=1,p=1} \\ u_{q=1,p=2} \\ \vdots \\ u_{q=1,p=p_{\mathrm{m}}} \\ u_{q=2,p=1} \\ \vdots \\ u_{q=2,p=p_{\mathrm{m}}} \end{bmatrix}$$

$\mathbf{A} = A_{q_1,q_2,p_1,p_2}$

$$(q_1,q_2,p_1,p_2) = \begin{bmatrix} 1,1,1,1 & \cdots & 1,1,1,p_{\mathrm{m}} & 1,2,1,1 & \cdots & 1,2,1,p_{\mathrm{m}} \\ \vdots & \ddots & \vdots & \vdots & \ddots & \vdots \\ 1,1,p_{\mathrm{m}},1 & \cdots & 1,1,p_{\mathrm{m}},p_{\mathrm{m}} & 1,2,p_{\mathrm{m}},1 & \cdots & 1,2,p_{\mathrm{m}},p_{\mathrm{m}} \\ 2,1,1,1 & \cdots & 2,1,1,p_{\mathrm{m}} & 2,2,1,1 & \cdots & 2,2,1,p_{\mathrm{m}} \\ \vdots & \ddots & \vdots & \vdots & \ddots & \vdots \\ 2,1,p_{\mathrm{m}},1 & \cdots & 2,1,p_{\mathrm{m}},p_{\mathrm{m}} & 2,2,p_{\mathrm{m}},1 & \cdots & 2,2,p_{\mathrm{m}},p_{\mathrm{m}} \end{bmatrix}$$

This coefficient ordering is appropriate when considering a single scatterer; when there are N scatterers in the system, indexed by $i \in [1..N]$, each scatterer is assigned its own local incoming field set, as well as its own scattered field coefficient set. The matrices describing the whole system thus consist in $2Np_{\max}$ coefficients per line or column (for a total of $4N^2p_{\max}^2$ coefficients in square matrices). The coefficient sets are then ordered by sets of $2p_{\max}$ coefficients, as earlier, with increasing scatterer index i. We cast below the general form of the resulting column and square matrices, each $\mathbf{u}^{(i)}$ representing a column matrix associated with the scatterer labelled i, and each $\mathbf{A}^{(i,j)}$ representing the effect of the scatterer i ($i = j$, diagonal blocks) or an interaction between scatterers i and j (non-diagonal blocks):

$$\mathbf{u}^{\mathrm{syst}} = \begin{bmatrix} \mathbf{u}^{(1)} \\ \vdots \\ \mathbf{u}^{(N)} \end{bmatrix}$$

$$\mathbf{A}^{\mathrm{syst}} = \begin{bmatrix} \mathbf{A}^{1,1} & \cdots & \mathbf{A}^{1,N} \\ \vdots & \ddots & \vdots \\ \mathbf{A}^{N,1} & \cdots & \mathbf{A}^{N,N} \end{bmatrix}$$

A.2 Vector Partial Waves: M and N

The time harmonic Maxwell equations in an absorption free host medium can take the form of a second order differential equation :

$$\nabla \times \nabla \times \mathbf{E}(\mathbf{r}) - k^2 \mathbf{E}(\mathbf{r}) = 0 \ , \tag{A.1}$$

with $k = \sqrt{\varepsilon_b \mu_b}\sqrt{\varepsilon_0 \mu_0}\omega = n_b \omega / c$, where (ε_0, μ_0) are the permittivity and permeability of the vacuum, and ε_b and μ_b are the relative permittivity and permeability of the "background" dielectric medium. The Vector Partial Waves (VPWs) are a set of spherical waves centered on a given origin and which form a complete basis set of solutions to eq.(A.1). [Stout 2012]

Any scattered field, $\mathbf{E}_\mathrm{s}(\mathbf{r})$, in the homogeneous medium and outside of a circumscribing sphere surrounding the scattering system can be developed in terms of outgoing partial waves, that describe the fields resulting from an ensemble of sources inside the system,*i.e.*:

$$\mathbf{E}_\mathrm{s}(\mathbf{r}) = \sum_{n,m} \left[\mathbf{M}^{\mathrm{out}}_{n,m}(k\mathbf{r}) f_{h,n,m} + \mathbf{N}^{\mathrm{out}}_{n,m}(k\mathbf{r}) f_{e,n,m} \right] \ , \tag{A.2}$$

where $\mathbf{M}^{\mathrm{out}}_{n,m}$, $\mathbf{N}^{\mathrm{out}}_{n,m}$, are the *outgoing* VPWs which satisfy eq.(A.1) with outgoing boundary conditions, and the $f_{q,n,m}$ are the complex coefficients of the scattered field in the VPW basis. They can be analytically expressed in spherical coordinates as:

$$\begin{aligned} \mathbf{M}^{\mathrm{out}}_{n,m}(k\mathbf{r}) &\equiv h_n(kr)\, \mathbf{X}_{nm}(\theta,\phi) \\ \mathbf{N}^{\mathrm{out}}_{n,m}(k\mathbf{r}) &\equiv \sqrt{n(n+1)} \frac{h_n(kr)}{kr} \mathbf{Y}_{nm}(\theta,\phi) + \frac{[krh_n(kr)]'}{kr} \mathbf{Z}_{nm}(\theta,\phi) \ , \end{aligned} \tag{A.3}$$

where h_n are the spherical Hankel functions of the first kind and $[krh_n(kr)]'$ is the derivative of $krh_n(kr)$ with respect to kr. In this definition, we use orthonormal vector spherical harmonics denoted $\mathbf{X}$, $\mathbf{Y}$, and $\mathbf{Z}$ respectively, which are defined in the next section.

On the other hand, any incoming field $\mathbf{E}_0(\mathbf{r})$ can be developed in a very similar manner, with the help of *regular* VPWs, which are the regular counterpart of the outgoing VPWs. Their expression is also very similar to the outgoing VPWs, the difference being that one replaces the spherical Hankel functions h_n by spherical Bessel functions j_n, thus obtaining the base vectors for a sourceless field (*i.e.* no sources are present inside the system):

$$\mathbf{E}_0(\mathbf{r}) = \sum_{n,m} \left[\mathbf{M}^{\mathrm{in}}_{n,m}(k\mathbf{r})\, e_{q=1,n,m} + \mathbf{N}^{\mathrm{in}}_{n,m}(k\mathbf{r})\, e_{q=2,n,m} \right] \tag{A.4}$$

$$\begin{aligned} \mathbf{M}^{\mathrm{in}}_{n,m}(k\mathbf{r}) &\equiv j_n(kr)\, \mathbf{X}_{nm}(\theta,\phi) \\ \mathbf{N}^{\mathrm{in}}_{n,m}(k\mathbf{r}) &\equiv \sqrt{n(n+1)} \frac{j_n(kr)}{kr} \mathbf{Y}_{nm}(\theta,\phi) + \frac{[krh_n(kr)]'}{kr} \mathbf{Z}_{nm}(\theta,\phi) \ , \end{aligned} \tag{A.5}$$

where the coefficients fo the incoming field are the $e_{q,n,m}$ complex numbers.

A.2.1 Compact matrix notations

In order to describe the scattering process using a compact matrix notation, we further introduce the "row-matrices" of the $2 \times p_{\max}$ outgoing and ingoing VPWs, respectively $[\mathbf{MN}]^{\text{out}}(\mathbf{r})$ and $[\mathbf{MN}]^{\text{in}}(\mathbf{r})$, which are defined by:

$$[\mathbf{MN}]^{\text{out,in}}(\mathbf{r}) \equiv \begin{bmatrix} \mathbf{M}_{p=1}^{\text{out,in}}(k_{\text{b}}\mathbf{r}) \\ \vdots \\ \mathbf{M}_{p=p_{\max}}^{\text{out,in}}(k_{\text{b}}\mathbf{r}) \\ \mathbf{N}_{p=1}^{\text{out,in}}(k_{\text{b}}\mathbf{r}) \\ \vdots \\ \mathbf{N}_{p=p_{\max}}^{\text{out,in}}(k_{\text{b}}\mathbf{r}) \end{bmatrix}^t$$

where each of the elements of $[\mathbf{MN}]^{\text{out,in}}(\mathbf{r})$ is a VPW, *i.e.* a 3-D vector expressed in the spherical basis. The equations that yield the scattered and incident fields, A.2 and A.4, can thus be written:

$$\mathbf{E}_{\text{s}}(\mathbf{r}) = [\mathbf{MN}]^{\text{out}}(\mathbf{r}) \cdot \mathbf{f} \tag{A.6}$$

$$\mathbf{E}_{0}(\mathbf{r}) = [\mathbf{MN}]^{\text{in}}(\mathbf{r}) \cdot \mathbf{e}, \tag{A.7}$$

where the "scalar product" is a shorthand notation for the sums of VPWs in equations A.2 and A.4.

We now define the compact notation of the scattered field in the case of a system that consists in an ensemble of N scatterers. Let $(\mathbf{u}_i)_{\text{i}\in[1..\text{N}]}$ be the set of vectors defining the position of each scatterer. Given a position $\mathbf{r}$ outside of each of the scatterers, where we want to express the total scattered field, we define the relative radius vectors with respect to the center of each scatterer, $\mathbf{r}_i = \mathbf{r} - \mathbf{u}_i$. We then build a $[\mathbf{MN}]^{\text{out,N}}(\mathbf{r})$ row-matrix that consist of $N \times 2p_{\max}$ VPWs, $2p_{\max}$ per scatterer:

$$[\mathbf{MN}]^{\text{out,N}}(\mathbf{r}) \equiv \begin{bmatrix} [\mathbf{MN}]^{\text{out}}(\mathbf{r}-\mathbf{u}_1) \\ [\mathbf{MN}]^{\text{out}}(\mathbf{r}-\mathbf{u}_2) \\ \vdots \\ [\mathbf{MN}]^{\text{out}}(\mathbf{r}-\mathbf{u}_N) \end{bmatrix}^t = \begin{bmatrix} [\mathbf{MN}]^{\text{out}}(\mathbf{r}_1) \\ [\mathbf{MN}]^{\text{out}}(\mathbf{r}_2) \\ \vdots \\ [\mathbf{MN}]^{\text{out}}(\mathbf{r}_N) \end{bmatrix}^t = \begin{bmatrix} \mathbf{M}_1(k_b\mathbf{r}_1) \\ \vdots \\ \mathbf{M}_{p_{max}}(k_b\mathbf{r}_1) \\ \mathbf{N}_1(k_b\mathbf{r}_1) \\ \vdots \\ \mathbf{N}_{p_{max}}(k_b\mathbf{r}_1) \\ \mathbf{M}_1(k_b\mathbf{r}_2) \\ \vdots \\ \mathbf{N}_{p_{max}}(k_b\mathbf{r}_N) \end{bmatrix}^t .$$

The field that is coherently scattered by the ensemble of N scatterers can then be written with the same shorthand notation:

$$\mathbf{E}_{\text{s}}(\mathbf{r}) = [\mathbf{MN}]^{\text{out,N}}(\mathbf{r}) \cdot \mathbf{f}. \tag{A.8}$$

A.3 Spherical vector harmonics: X, Y and Z

The Spherical Vector Harmonics (SVHs) contain the variation of the VPWs that do not depend on the radius. Throughout the whole thesis, we use orthonormal (over angular integration) SVHs, meaning that the following relation is verified:

$$\int_0^{\pi} \sin\theta d\theta \int_0^{2\pi} d\phi \, \mathbf{A}^*_{\nu,\mu}(\theta,\phi)\cdot\mathbf{B}_{n,m}(\theta,\phi) = \delta_{\nu,n}\delta_{\mu,m}\delta_{A,B} \ , \tag{A.9}$$

with A and $B \in [X,Y,Z]$.

They are built from a "source" term $Y^{\mathrm{src}}_{n,m}$, that corresponds to the radial part of the fields satisfying Maxwell equations in a homogeneous medium (which is thus non-propagative in the far-field). One can cast the SVHs in a compact fashion:

$$\begin{aligned}
\mathbf{Y}_{n,m}(\theta,\phi) &\equiv \hat{\mathbf{r}} Y^{\mathrm{src}}_{n,m}(\theta,\phi) \\
\mathbf{Z}_{n,m}(\theta,\phi) &\equiv r\frac{\overrightarrow{\nabla} Y^{\mathrm{src}}_{n,m}(\theta,\phi)}{\sqrt{n(n+1)}} \\
\mathbf{X}_{n,m}(\theta,\phi) &\equiv \mathbf{Z}_{n,m}(\theta,\phi)\times\hat{\mathbf{r}}
\end{aligned}$$

For the practical numerical computing of the "source" term and of the VPWs and SVHs, we use the algorithm described below.

A.3.1 Numerical algorithm: precursor functions

In order to compute the SVHs, we use algorithms that are based on recurrences on the multipole expansion numbers. In the definitions below, it is assumed that invalid values of the m or n expansion numbers give a null result: $f(n,m,z) \equiv 0$ if $(|m| > n)$ or $(n < 0)$, with f being any of the functions defined below. The multiple-cases definitions are to be considered sequentially (*i.e.* if the first condition is not fullfulled, then the next one is checked, and so on until the last one, which covers all the remaining cases).

$$\underset{n\in\mathbb{N},z\in\mathbb{C}}{\nu_{\mathrm{eq}}(n,z)} \equiv \begin{cases} -\sqrt{3/(16\pi)} & \text{if } n=0 \\ -\sqrt{\frac{n(2n+1)(1-z^2)}{2(n+1)(n-1)}}\nu_{\mathrm{eq}}(n-1,z) & \text{if } n>0 \end{cases}$$

$$\underset{n,m\in\mathbb{N},z\in\mathbb{C}}{\nu_{\mathrm{pos}}(n,m,z)} \equiv \begin{cases} 0 & \text{if } (n=0) \text{ or } (n=1 \text{ and } m=0) \\ \nu_{\mathrm{eq}}(n,z) & \text{if } m=n \\ z\sqrt{\frac{(n-1)(2n+1)}{n+1}}\nu_{\mathrm{eq}}(n-1,z) & \text{if } m=n-1 \\ \text{else (see below)} & \end{cases}$$

$$\underset{\text{other cases}}{\nu_{\mathrm{pos}}(n,m,z)} = \sqrt{\frac{(n-1)(2n+1)}{(n+1)(n^2-m^2)}} \times \ldots$$

$$\left(z\sqrt{2n-1}\nu_{\mathrm{pos}}(n-1,m,z) - \sqrt{\frac{(n-2)((n-1)^2-m^2)}{n(2n-3)}}\nu_{\mathrm{pos}}(n-2,m,z) \right)$$

$$\underset{n\in\mathbb{N},m\in\mathbb{Z},z\in\mathbb{C}}{\nu_{\mathrm{f}}(n,m,z)} \equiv \begin{cases} \nu_{\mathrm{pos}}(n,m,z) \text{ if } m \geq 0 \\ (-1)^{m+1}\nu_{\mathrm{pos}}(n,-m,z) \text{ if } m < 0 \end{cases}$$

$$\underset{n,m\in\mathbb{N},z\in\mathbb{C}}{ns_{\mathrm{pos}}(n,m,z)} \equiv \begin{cases} 0 \text{ if } m < 0 \\ z\nu_{\mathrm{f}}(n,n,z) \text{ if } m = n \\ \text{else } z\nu_{\mathrm{f}}(n,m,z) + \frac{\sqrt{(n-m)(n+m+1)(1-z^2)}}{m+1} \end{cases}$$

$$\underset{n,m\in\mathbb{N},z\in\mathbb{C}}{sf_{\mathrm{pos}}(n,m,z)} \equiv z\nu_{\mathrm{f}}(n,m,z) + \sqrt{\frac{(n+m+1)(n-m)}{m+1}}\sqrt{1-z^2}\ \nu_{\mathrm{f}}(n,m+1,z)$$

$$\underset{n\in\mathbb{N},m\in\mathbb{Z},z\in\mathbb{C}}{ns_{\mathrm{f}}(n,m,z)} \equiv \begin{cases} (-1)^m sf_{\mathrm{pos}}(n,-m,z) \text{ if } m < 0 \\ sf_{\mathrm{pos}}(n,m,z) \text{ if } m \geq 0 \end{cases}$$

$$n_{\mathrm{pl}}(0,0,z) \equiv \sqrt{1/(4\pi)}$$
$$n_{\mathrm{pl}}(1,-1,z) \equiv \sqrt{\frac{3(1-z^2)}{8\pi}}$$
$$n_{\mathrm{pl}}(1,0,z) \equiv z\sqrt{\frac{3}{4\pi}}$$
$$n_{\mathrm{pl}}(1,1,z) \equiv -\sqrt{\frac{3(1-z^2)}{8\pi}}$$
$$\underset{n\in\mathbb{N},m\in\mathbb{Z},z\in\mathbb{C}}{n_{\mathrm{pl}}(n,m,z)} \equiv \begin{cases} \text{(see above) if } n = 0 \text{ or } n = 1 \\ \frac{1}{n}\left(z\sqrt{4n^2-1}n_{\mathrm{pl}}(n-1,0,z) - (n-1)\sqrt{\frac{2n+1}{2n-3}}n_{\mathrm{pl}}(n-2,0,z)\right) \text{ if } m = 0 \\ \text{else } \sqrt{n(n+1)(1-z^2)}\frac{\nu_{\mathrm{f}}(n,m,z)}{m} \end{cases}$$

$$\underset{n\in\mathbb{N},z\in\mathbb{C}}{n_{\mathrm{lgdr}}(n,z)} \equiv \begin{cases} \sqrt{1/2} \text{ if } n = 0 \\ \frac{1}{n}\left(z\sqrt{4n^2-1}n_{\mathrm{lgdr}}(n-1,z) - (n-1)\sqrt{\frac{2n+1}{2n-3}}n_{\mathrm{lgdr}}(n-2,z)\right) \text{ if } n > 0 \end{cases}$$

A.3.2 Explicit definition of the SVHs

With the help of the precursor functions defined in the previous section, we define a "source" term of the SVHs:

$$Y^{\mathrm{src}}_{n,m}(\theta,\phi) \equiv \begin{cases} \sqrt{\frac{1}{2\pi}}n_{\mathrm{lgdr}}(n,cos(\theta)) \text{ if } m = 0 \\ \sqrt{n(n+1)}\sin(\theta)\nu_{\mathrm{f}}(n,m,\cos(\theta))\frac{\exp(im\phi)}{m} \text{ if } m \neq 0 \end{cases}$$

We can cast the SVHs in the spherical basis, $[\hat{\mathbf{e}}_r, \hat{\mathbf{e}}_\theta, \hat{\mathbf{e}}_\phi]$:

$$\begin{aligned} \mathbf{X}_{n,m}(\theta,\phi) \equiv &\quad [0, \nu_{\mathrm{f}}(n,m,\cos\theta)\ i\ \exp(im\phi), -ns_{\mathrm{f}}(n,m,\cos\theta)\exp(im\phi)] \\ \mathbf{Y}_{n,m}(\theta,\phi) \equiv &\quad [Y^{\mathrm{src}}_{n,m}(\theta,\phi), 0, 0] \\ \mathbf{Z}_{n,m}(\theta,\phi) \equiv &\quad [0, ns_{\mathrm{f}}(n,m,\cos\theta)\exp(im\phi), \nu_{\mathrm{f}}(n,m,\cos\theta)\ i\ \exp(im\phi)] \end{aligned}$$

We have thus given an explicit algorithm that allows one to compute the SVHs, and thus the VPWs, in other words, all the base vectors of the multipole expansion of the electromagnetic fields that satisfy the Maxwell equations.

Appendix B

Mie theory

In this appendix, we will give the Mie solution for the scattering of a single, homogeneous sphere (radius a, relative permittivity ε_s, relative permeability μ_s) arbitrarily placed at the origin of the coordinate system, in a homogeneous, absorption-free background medium (relative permittivity ε_b, relative permeability μ_b). The vacuum wavelength under study is λ_0 and the wavevector in the homogeneous background medium is written $k_b \equiv n_b \frac{2\pi}{\lambda_0} \equiv \sqrt{\varepsilon_b \mu_b} \frac{2\pi}{\lambda_0}$, and respectively the wavevector inside the scatterer is $k_s \equiv \sqrt{\varepsilon_s \mu_s} \frac{2\pi}{\lambda_0}$.

The problem is reduced in section B.1 to a diagonal T-matrix, $\mathbf{T}$, that relates the incoming and scattered fields coefficients, $\mathbf{e}$ and $\mathbf{f}$, in the multipole basis of the VPWs: $\mathbf{f} = \mathbf{T}\mathbf{e}$. The resulting field *inside* the scatterer is treated separately in section B.3.

B.1 Mie coefficients expression

The incoming field $\mathbf{E}_0$ is represented by the incoming field coefficients expressed at the centre of the sphere, $e_{\mathrm{q,n,m}}$ which form the column matrix $\mathbf{e}$. The multipoles of the scatterer are excited by the incoming field, and the sphere will behave outside of its circumscribing sphere as a multipolar source. The scattered field $\mathbf{E}_\mathrm{s}(\mathbf{r})$ can be described by the scattered field coefficients $f_{\mathrm{q,n,m}}$ which form the column matrix $\mathbf{f}$:

$$\mathbf{E}_\mathrm{s}(\mathbf{r}) = \sum_{n,m} \left[\mathbf{M}^{\mathrm{out}}_{n,m}(k\mathbf{r})\, f_{q=1,n,m} + \mathbf{N}^{\mathrm{out}}_{n,m}(k\mathbf{r})\, f_{q=2,n,m} \right], \tag{B.1}$$

which can be written using the shorthand notation of appendix A.2.1:

$$\mathbf{E}_\mathrm{s}(\mathbf{r}) = [\mathbf{MN}]^{\mathrm{out}}(\mathbf{r}) \cdot \mathbf{f}. \tag{B.2}$$

The relationship between the incoming and scattered fields has the simple form:

$$\begin{aligned} f_{\mathrm{q=1,n,m}} &= b_n \frac{3}{2i(ka)^3} e_{\mathrm{q=1,n,m}} \\ f_{\mathrm{q=2,n,m}} &= a_n \frac{3}{2i(ka)^3} e_{\mathrm{q=2,n,m}} \end{aligned} \tag{B.3}$$

where a_n and b_n are the Mie coefficients of the sphere:

$$a_n = \frac{j_n(ak_b)}{h_n(ak_b)} \frac{\varepsilon_s \varphi_n(ak_b) - \varepsilon_b \varphi_n(ak_s)}{\varepsilon_b \varphi_1(ak_s) - \varepsilon_s \varphi_n^{(3)}(ak_b)} \tag{B.4}$$

$$b_n = \frac{j_n(ak_b)}{h_n(ak_b)} \frac{\mu_s \varphi_n(ak_b) - \mu_b \varphi_n(ak_s)}{\mu_b \varphi_1(ak_s) - \mu_s \varphi_n^{(3)}(ak_b)} \tag{B.5}$$

where j_n and h_n are the spherical Bessel and Hankel functions of the first kind; φ_n and $\varphi_n^{(3)}$ are the 'logarithmic derivatives' of j_n and h_n respectively:

$$\varphi_n(z) \equiv \frac{1}{j_n(z)} \frac{\mathrm{d}}{\mathrm{d}z}[z\ j_n(z)] \tag{B.6}$$

$$\varphi_n^{(3)}(z) \equiv \frac{1}{h_n(z)} \frac{\mathrm{d}}{\mathrm{d}z}[z\ h_n(z)]. \tag{B.7}$$

B.2 T-matrix of an isolated sphere

Using equations B.3, the scattering of the sphere can thus be described, for a given point $\mathbf{r}$ outside of the sphere, and a given maximal multipolar order $n_{\max}$, by a diagonal T-matrix of size $[2n_{\max}(n_{\max}+2)]^2$ whose diagonal coefficients are $b_n \frac{3}{2i(ka)^3}$ for the first $n_{\max}(n_{\max}+2)$ and $a_n \frac{3}{2i(ka)^3}$ for the next $n_{\max}(n_{\max}+2)$, each multipolar order $n \in [1..n_{\max}]$ being repeated $2n+1$ times:

$$\mathbf{f} = \mathbf{T}\mathbf{e} \tag{B.8}$$

$$T(p_1, p_2) = \delta(p_1 - p_2) \begin{cases} b_n \frac{3}{2i(ka)^3} & \text{if } p_1 \leq p_{\max},\ n = \mathrm{floor}(\sqrt{p_1}) \\ a_n \frac{3}{2i(ka)^3} & \text{if } p_1 > p_{\max},\ n = \mathrm{floor}(\sqrt{p_1 - p_{\max}}) \end{cases} \tag{B.9}$$

The scattering problem is thus solved for every point outside of the scatterer. In the next section we give the expression of the field inside the scatterer.

B.3 Field inside the sphere

The field inside the sphere, $\mathbf{E}_{\mathrm{int}}(\mathbf{r})$, can be expanded in terms of regular VPWs with coefficients $\mathbf{e}_{\mathrm{int}}$ that can be calculated from the scattered field coefficients $\mathbf{f}$ of the sphere: [Stout 2001]

$$\mathbf{E}_{\mathrm{int}}(\mathbf{r}) = \quad [\mathbf{MN}]^{in}(\mathbf{r}) \cdot \mathbf{e}_{\mathrm{int}}$$

$$\begin{aligned} e_{\mathrm{int},q=1,n,m} &= \mu_s \tfrac{k_s}{k_b} \tfrac{i}{\mu_b(k_s/k_b)\psi_n'(ak_s)\psi_n(ak_b) - \mu_s\psi_n(ak_s)\psi_n'(ak_b)} f_{q=1,n,m} \\ e_{\mathrm{int},q=2,n,m} &= \mu_s \tfrac{k_s}{k_b} \tfrac{i}{\mu_s\psi_n'(ak_s)\psi_n(ak_b) - (k_s/k_b)\mu\psi_n(ak_s)\psi_n'(ak_b)} f_{q=2,n,m}, \end{aligned}$$

where $\psi_n(x) = x j_n(x)$ is the Riccati-Bessel function.

Appendix C

Solving multiple scattering problems

In this appendix, we will give the explicit formulas that allows us to solve a multiple scattering problem. The system is composed of an ensemble of N_{sph} spherically-symetric scatterers. Together with the individual response of each sphere, the fields scattered by the $(N_{\text{sph}}-1)$ other spheres in the system are to be calculated formally for each scatterer by using the translation-addition theorem. The resulting multiple-scattering system is written in the form of (the inverse of) a T-matrix.

This T-matrix does not depend on the illumination conditions, but obtaining the solution for a given illumination (obtaining the scattered field coefficients $\mathbf{f}$ from the incoming coefficients $\mathbf{e}$) requires solving a system of the form $\mathbf{T}^{-1}\mathbf{f} = \mathbf{e}$, where $\mathbf{T}^{-1}$ is known explicitly, but not $\mathbf{T}$. From a numerical standpoint, this is the main difference between multiple scattering and single scattering from a homogeneous sphere, wherein the T-matrix is explicitely known, and moreover diagonal, rendering its inversion trivial. In most cases (*e.g.* when $n_{\max} > 2$ or $N_{\text{sph}} > 2$) one favors a numerical matrix inversions, due to the complexity of the matrix system of equations.

C.1 Translation-addition theorem

The translation-addition theorem permits the transformation of spherical waves (incoming or outgoing VPWs) centred around a given origin, to be expressed in terms of spherical waves developed about a different point. In this section, we give the essential formulas of this theorem, which allow the resolution of multiple scattering problems, as well as the evaluation of some physical quantities associated with those problems, like radiative and nonradiative decay rates (see appendix D.2). The equations presented below are adapted from [Stout 2002], and full derivations are avaiable in *e.g.* [Stein 1961, Cruzan 1962, Tsang 1985, Chew 1990].

Let O be the origin of a reference spherical coordinate system. We consider a point P which defines a spherical coordinate position vector $\mathbf{r} = \overrightarrow{OP}$. Consider now another origin O' for the spherical coordinates with position vector $\mathbf{r}_0 = \overrightarrow{OO'}$. The spherical coordinates of P around this new origin are $\mathbf{r}' = \mathbf{r} - \mathbf{r}_0$. The translation addition theorem allows one to express the VPWs centered on origin O, in terms of

VPWs centered on origin O':

$$[\mathbf{MN}]^{\text{inc}}(\mathbf{r}) = [\mathbf{MN}]^{\text{inc}}(\mathbf{r}')\ \mathbf{J}(\mathbf{r_0}) \tag{C.1}$$

$$[\mathbf{MN}]^{\text{out}}(\mathbf{r}) = \begin{cases} [\mathbf{MN}]^{\text{out}}(\mathbf{r}')\ \mathbf{J}(\mathbf{r_0}) & \text{if } |\mathbf{r}'| > |\mathbf{r}_0| \\ [\mathbf{MN}]^{\text{inc}}(\mathbf{r}')\ \mathbf{H}(\mathbf{r_0}) & \text{if } |\mathbf{r}'| < |\mathbf{r}_0| \end{cases} \tag{C.2}$$

where $\mathbf{J}(\mathbf{r})$ and $\mathbf{H}(\mathbf{r})$ are the regular and irregular translation matrices, respectively (see below in section C.1.1).

Equation C.1 allows one to express a free-propagating incoming field described at position O by a column matrix of incoming field coefficients $\mathbf{e}_O$, into an incoming field at position O', with a column matrix of coefficients $\mathbf{e}_{O'}$:

$$\mathbf{e}_O = \mathbf{J}(\mathbf{r}_0)\mathbf{e}_{O'}, \tag{C.3}$$

while equation C.2 allows, amongst other applications, to express the scattered field of a particle placed at position O (described by a column matrix $\mathbf{f}_O$ of outgoing VPWs centered on O) in terms of incident field placed at O' (in terms of a column matrix $\mathbf{e}_{O'}$ of ingoing VPWs centered on O'):

$$\mathbf{e}_{O'} = \mathbf{H}(\mathbf{r_0})\mathbf{f}_r, \tag{C.4}$$

an expansion which is valid as long as the local radius of the scatterer centred on O' is lower than the distance between the two centres, $|\mathbf{r}'| < |\mathbf{r}_0|$, a condition that is always true in the case of spherical particles.

We point out that equations C.1 and C.2 are, strictly speaking, only true in the infinite-dimensionnal VPW basis (each of the matrices is formally an infinite-rank matrix). In practice, and in order to carry out numerical computations, the infinite basis has to be truncated at a maximal expansion number, $n_{\max}$. This allows one to compute quasi-exact solutions of the scattering problem, since there is a maximal multipolarity number $n(R)$, the order of kR, beyond which the single-particle T-matrix elements of a scatterer of radius R are essentially zero.

C.1.1 Expression of the regular and irregular translation matrices

The $\mathbf{H}(\mathbf{r})$ matrix is defined by blocks:

$$\mathbf{H}(\mathbf{r}) = \begin{bmatrix} \mathbf{A}(k_b\mathbf{r}) & \mathbf{B}(k_b\mathbf{r}) \\ \mathbf{B}(k_b\mathbf{r}) & \mathbf{A}(k_b\mathbf{r}) \end{bmatrix}, \tag{C.5}$$

with each block consisting in $n_{\max}(n_{\max}+2)$ coefficients. The regular translation matrix $\mathbf{J}(\mathbf{r})$ can be computed by taking the regular part of $\mathbf{H}(\mathbf{r})$ (*i.e.* using the same expressions except for replacing spherical Hankel functions h_n by spherical Bessel functions j_n – see below).

We use *normalized* translation matrices. The coefficients of the **A** and **B** blocks can be cast using scalar translation-addition coefficients $a_{\nu,\mu,n,m}$: [Stout 2002]

$$\begin{aligned}
A_{\nu,\mu,n,m} = \quad & \tfrac{1}{2}\sqrt{\tfrac{1}{\nu(\nu+1)n(n+1)}}\big[2\mu m a_{\nu,\mu,n,m} \\
& + \sqrt{(n-m)(n+m+1)(\nu-\mu)(\nu+\mu+1)}\,a_{\nu,\mu+1,n,m+1} \\
& + \sqrt{(n+m)(n-m+1)(\nu+\mu)(\nu-\mu+1)}\,a_{\nu,\mu-1,n,m-1}\big] \\
B_{\nu,\mu,n,m} = \quad & \tfrac{-i}{2}\sqrt{\tfrac{2\nu+1}{2\nu-1)\nu(\nu+1)n(n+1)}}\big[2m\sqrt{(\nu-\mu)(\nu+\mu)}\,a_{\nu-1,\mu,n,m} \\
& + \sqrt{(n-m)(n+m+1)(\nu-\mu)(\nu-\mu-1)}\,a_{\nu-1,\mu+1,n,m+1} \\
& - \sqrt{(n+m)(n-m+1)(\nu+\mu)(\nu+\mu-1)}\,a_{\nu-1,\mu-1,n,m-1}\big]
\end{aligned}$$

where the $(k_b\mathbf{r})$ variable dependance on the scalar coefficients has been dropped for clarity. In order to calculate the scalar coefficients we define the following coefficients and base functions:

$$\begin{aligned}
a^+_{n,m} &\equiv -\sqrt{\tfrac{(n+m+1)(n-m+1)}{(2n+1)(2n+3)}} \\
a^-_{n,m} &\equiv \sqrt{\tfrac{(n+m)(n-m)}{(2n+1)(2n-1)}} \\
b^+_{n,m} &\equiv \sqrt{\tfrac{(n+m+2)(n-m+1)}{(2n+1)(2n+3)}} \\
b^-_{n,m} &\equiv \sqrt{\tfrac{(n-m)(n-m-1)}{(2n+1)(2n-1)}} \\
Y_{n,m}(\theta,\phi) &\equiv \exp(im\phi)\; P^m_n(\cos\theta)\sqrt{\tfrac{(2n+1)(n-m)!}{4\pi(n+m)!}} \qquad \text{(C.6)} \\
a_{\nu,\mu,0,0}(k_b r,\theta,\phi) &\equiv \sqrt{4\pi}(-1)^{\nu+\mu}Y_{\nu,-\mu}(\theta,\phi)h_\nu(k_b r)
\end{aligned}$$

where the P^m_n are the associated Legendre polynomials and the coefficients $a^\pm_{n,m}$ and $b^\pm_{n,m}$ are zero for $|m| > n$ or $n < 0$. The scalar coefficients for $n \neq 0$ or $m \neq 0$ can then be computed using the following recursive algorithm:

$a_{\nu,\mu,n,m}(r,\theta,\phi) \equiv$

$$\begin{cases}
\bullet\ 0 & \text{if } |m| > n \text{ or } |\mu| > \nu \text{ or } \nu < 0 \text{ or } n < 0 \\
\bullet\ (-1)^{\nu+\mu+n+m}a^*_{\nu,-\mu,n,-m}(-r^*,\theta,\phi) & \text{if } m < 0 \\
\bullet\ \text{(see above)} & \text{if } n = m = 0 \\
\bullet\ \frac{1}{b^+_{n-1,n-1}}\big[b^+_{\nu-1,\mu-1}a_{\nu-1,\mu-1,n-1,n+1}(r,\theta,\phi) & \\
\quad + b^-_{\nu+1,\mu-1}a_{\nu+1,\mu-1,n-1,n-1}(r,\theta,\phi)\big] & \text{if } n = m \\
\bullet\ \frac{1}{a^+_{n-1,m}}\big[a^-_{\nu+1,\mu}a_{\nu+1,\mu,n-1,m}(r,\theta,\phi) & \\
\quad + a^+_{\nu-1,\mu}a_{\nu-1,\mu,n-1,m}(r,\theta,\phi) & \\
\quad - a^-_{n-1,m}a_{\nu,\mu,n-2,m}(r,\theta,\phi)\big] & \text{elsewhere}
\end{cases}$$

The regular translation matrices can be calculated using the same algorithm, but replacing spherical Hankel functions h_n by spherical Bessel functions j_n in the definition of $Y_{n,m}(\theta,\phi)$ (equation C.6).

C.2 Multiple-scattering T-matrix

We consider an ensemble of N scatterers (each characterized by a known T-matrix) illuminated with a known incident field. If there are only linear scattering interactions between each of the N scatterers, it follows from the superposition principle that for a given incident field upon the system, each scatterer i will behave as if it individually received the superposition of the incoming field, and of the field scattered to its position by each of the $N-1$ other scatterers. Since the latter sum depends itself on the field scattered by the i-th scatterer, we are left with a system of coupled equations. In the case of an ensemble of homogeneous, spherical scatterers, we can formulate the problem using Mie theory and the translation-addition theorem. We give a derivation of the expression of the multiple-particle T-matrix below.

Let O be the arbitrary origin of the coordinate system, position vector, $(\mathbf{u}_i)_i$ the positions of the spheres and $\mathbf{T}_i$ their individual T-matrices. We define the spherical coordinates centered on each sphere, particle-centered radius $\mathbf{r_i} = \mathbf{r} - \mathbf{u}_i$. Each sphere produces a scattered field $\mathbf{E}_\mathrm{s}(\mathbf{r_i})$ that can be written in terms of outgoing VPWs centered on themselves with scattered coefficients $\mathbf{f}_i$:

$$\mathbf{E}_\mathrm{s}(\mathbf{r}_i) = [\mathbf{MN}]^{out}(\mathbf{r}_i) \cdot \mathbf{f}_i$$

Using equation C.4, this scattered field can be expressed as an incoming field upon another sphere j with the VPWs centered on the sphere j:

$$\mathbf{E}_s^{i\to j}(\mathbf{r}_j) = [\mathbf{MN}]^{\mathrm{in}}(\mathbf{r}_j) \cdot \left[\mathbf{H}(\mathbf{u}_j - \mathbf{u}_i)\mathbf{f}_i\right] \tag{C.7}$$

Let $\mathbf{e}_O$ be the column matrix describing the incident field upon the system with VPWs centered on O, using equation C.3 it can be described in terms of VPWs centered on the scatterer j:

$$\mathbf{E}_\mathrm{i}(\mathbf{r}_j) = [\mathbf{MN}]^{\mathrm{in}}(\mathbf{r}_j)\mathbf{J}(\mathbf{u}_j)\mathbf{e}_O. \tag{C.8}$$

The excitation field for the sphere j thus writes:

$$\mathbf{E}_\mathrm{exc}(\mathbf{r}_j) = [\mathbf{MN}]^{\mathrm{in}}(\mathbf{r}_j) \cdot \left[\mathbf{J}(\mathbf{u}_j)\mathbf{e}_O + \sum_{i\neq j} \mathbf{H}(\mathbf{u}_j - \mathbf{u}_i)\mathbf{f}_i\right]. \tag{C.9}$$

and the excitation field coefficients for the sphere j are thus:

$$\mathbf{e}_\mathrm{exc,j} = \mathbf{J}(\mathbf{u}_j)\mathbf{e}_O + \sum_{i\neq j} \mathbf{H}(\mathbf{u}_j - \mathbf{u}_i)\mathbf{f}_i \tag{C.10}$$

Since $\mathbf{f}_i = \mathbf{T}_i\mathbf{e}_\mathrm{exc,i}$ we obtain the coupled system:

$$\mathbf{e}_\mathrm{exc,j} - \sum_{i\neq j} \mathbf{H}(\mathbf{u}_j - \mathbf{u}_i)\mathbf{T}_i\mathbf{e}_\mathrm{exc,i} = \mathbf{J}(\mathbf{u}_j)\mathbf{e}_{0,j}. \tag{C.11}$$

where $\mathbf{e}_{0,j} = \mathbf{J}(\mathbf{u}_j)\mathbf{e}_O$ are the incoming field coefficients of sphere j. The matrix form of this coupled equations system can be cast:

$$\begin{bmatrix} \mathbf{Id} & -\mathbf{H}(\mathbf{u}_1 - \mathbf{u}_2)\mathbf{T}_2 & \cdots & -\mathbf{H}(\mathbf{u}_1 - \mathbf{u}_N)\mathbf{T}_N \\ -\mathbf{H}(\mathbf{u}_2 - \mathbf{u}_1)\mathbf{T}_1 & \mathbf{Id} & \cdots & -\mathbf{H}(\mathbf{u}_2 - \mathbf{u}_N)\mathbf{T}_N \\ \vdots & \vdots & \ddots & \vdots \\ -\mathbf{H}(\mathbf{u}_N - \mathbf{u}_1)\mathbf{T}_1 & -\mathbf{H}(\mathbf{u}_N - \mathbf{u}_2)\mathbf{T}_2 & \cdots & \mathbf{Id} \end{bmatrix} \begin{bmatrix} \mathbf{e}_\mathrm{exc,1} \\ \mathbf{e}_\mathrm{exc,2} \\ \vdots \\ \mathbf{e}_\mathrm{exc,N} \end{bmatrix} = \begin{bmatrix} \mathbf{e}_{0,1} \\ \mathbf{e}_{0,2} \\ \vdots \\ \mathbf{e}_{0,N} \end{bmatrix}$$

The multiple-scattering matrix is then obtained by multiplying both sides by the inverse of the leftmost matrix in the latter equation, then multiplying both sides by the block diagonal matrix of individual T-matrices, $\mathrm{diag}\left(\mathbf{T}_{i\in[1..N]}\right)$, in order to recover the scattered field coefficients on the left hand side:

$$\begin{bmatrix} \mathbf{f}_1 \\ \mathbf{f}_2 \\ \vdots \\ \mathbf{f}_N \end{bmatrix} = \begin{bmatrix} \mathbf{T}_1^{-1} & -\mathbf{H}(\mathbf{u}_1-\mathbf{u}_2) & \cdots & -\mathbf{H}(\mathbf{u}_1-\mathbf{u}_N) \\ -\mathbf{H}(\mathbf{u}_2-\mathbf{u}_1) & \mathbf{T}_2^{-1} & \cdots & -\mathbf{H}(\mathbf{u}_2-\mathbf{u}_N) \\ \vdots & \vdots & \ddots & \vdots \\ -\mathbf{H}(\mathbf{u}_N-\mathbf{u}_1) & -\mathbf{H}(\mathbf{u}_N-\mathbf{u}_2) & \cdots & \mathbf{T}_N^{-1} \end{bmatrix}^{-1} \begin{bmatrix} \mathbf{e}_{0,1} \\ \mathbf{e}_{0,2} \\ \vdots \\ \mathbf{e}_{0,N} \end{bmatrix}, \tag{C.12}$$

where we succeeded into expressing the scattered field coefficients directly in terms of a matrix product of the incident field coefficients. The multiple-scattering T-matrix is thus:

$$\mathbf{T} = \begin{bmatrix} \mathbf{T}_1^{-1} & -\mathbf{H}(\mathbf{u}_1-\mathbf{u}_2) & \cdots & -\mathbf{H}(\mathbf{u}_1-\mathbf{u}_N) \\ -\mathbf{H}(\mathbf{u}_2-\mathbf{u}_1) & \mathbf{T}_2^{-1} & \cdots & -\mathbf{H}(\mathbf{u}_2-\mathbf{u}_N) \\ \vdots & \vdots & \ddots & \vdots \\ -\mathbf{H}(\mathbf{u}_N-\mathbf{u}_1) & -\mathbf{H}(\mathbf{u}_N-\mathbf{u}_2) & \cdots & \mathbf{T}_N^{-1} \end{bmatrix}^{-1} \tag{C.13}$$

It should be noted that only $\mathbf{T}^{-1}$ is known analytically, and not $\mathbf{T}$ itself, in the general case. When one only needs to get the scattered field coefficients $\mathbf{f}$ for a given illumination $\mathbf{e}_O$, a fast and accurate numerical technique consists in solving the matrix system $\mathbf{T}^{-1}\mathbf{f} = \mathbf{e}_O$ in $\mathbf{f}$ using iterative techniques. In some cases though, such as when considering a number of different illumination conditions (solving the scattering problem for various incoming field coefficients $\mathbf{e}$ on the same system), the explicit values of the T-matrix may be required, and one should carry out the complete matrix inversion of Equation C.13. In general, matrices like the one on the right side of eq.(C.13) are numerically ill-conditioned for matrix inversion. However, direct (*e.g.* gaussian-pivot type) matrix inversions work quite well if one employs analytical matrix balancing techniques.[Stout 2008]

Appendix D

Figure of Merit computations

D.1 Cross-sections

The scattering, extinction and absorption cross-sections for a system of N scatterers illuminated by a plane wave, are defined in terms of power flux using the Poynting vectors $\mathbf{P}_{\text{inc}}$, $\mathbf{P}_{\text{scat}}$ and $\mathbf{P}_{\text{ext}}$ of the incident, scattering and extinction flux respectively:

$$\begin{aligned}
\mathbf{P}_{\text{inc}} = & \quad \tfrac{1}{2}\text{Re}\big[\mathbf{E}_{\text{inc}}(\mathbf{r}) \times \mathbf{H}_{\text{inc}}(\mathbf{r})\big] \\
\mathbf{P}_{\text{scat}}(\mathbf{r}) = & \quad \tfrac{1}{2}\sum_{i,j=1}^{N} \text{Re}\big[\mathbf{E}^{(i)}_{\text{scat}}(\mathbf{r}) \times \mathbf{H}^{(j)]}_{\text{scat}}(\mathbf{r})\big] \\
\mathbf{P}_{\text{ext}}(\mathbf{r}) = & \quad \tfrac{1}{2}\sum_{j=1}^{N} \text{Re}\big[\mathbf{E}_{\text{inc}}(\mathbf{r}) \times \mathbf{H}^{(j)}_{\text{scat}}(\mathbf{r}) + \mathbf{E}^{(j)}_{\text{scat}}(\mathbf{r}) \times \mathbf{H}_{\text{inc}}(\mathbf{r})\big],
\end{aligned}$$

where the extinction power flux is taken from the incident field by the N scatterers, and converted into radiated power and power dissipated by ohmic losses.

The scattering cross-section is defined by the total power flux radiated in the far-field, divided by the incident flux. Let $S(R)$ be the spherical surface of radius R, and $\text{d}\Omega = R\sin\theta \text{d}\theta\text{d}\phi$ the solid angle variation, the scattering cross-section can thus be cast:

$$\sigma_{\text{scat}} = \frac{1}{|\mathbf{P}_{\text{inc}}|}\lim_{R\to\infty}\int_{S(R)} \mathbf{P}_{\text{scat}}(\mathbf{r}) \cdot \mathbf{r}\ \text{d}\Omega.$$

In the following derivationss (equations D.1 and D.2) we assume that the plane wave, of incoming wavevector direction $\hat{\mathbf{k}}_{\text{i}}$ and linear electric polarization direction $\hat{\mathbf{e}_{\text{pol}}}$, is expressed at the origin with the incoming field expansion coefficients $\mathbf{e}_O$ defined by: [Stout 2001]

$$\begin{aligned}
e_{O,q=1,n,m} &= -i^n 4\pi \mathbf{X}^*_{n,m}(\hat{\mathbf{k}}_{\text{i}}) \cdot \hat{\mathbf{e}_{\text{pol}}} \\
e_{O,q=2,n,m} &= -i^{n+1} 4\pi \mathbf{Z}^*_{n,m}(\hat{\mathbf{k}}_{\text{i}}) \cdot \hat{\mathbf{e}_{\text{pol}}},
\end{aligned}$$

where $\mathbf{X}_{n,m}$ and $\mathbf{Z}_{n,m}$ are the VSHs defined in A.3. Using the multipole expansion of the scattered fields, together with the orthonormality and far-field limits of the VPWs, the scattering cross-section can be cast: [Stout 2001]

$$\sigma_{\text{scat}} = \frac{1}{k_b^2}\sum_{i=1}^{N}\sum_{j=1}^{N} \text{Re}\big[\mathbf{f}_i^{\dagger} \cdot \mathbf{J}(\mathbf{u}_i - \mathbf{u}_j)\ \mathbf{f}_j\big] \tag{D.1}$$

where $\mathbf{f}_j$ and $\mathbf{u}_j$ are the scattered field expansion coefficients and the position of the sphere j, respectively. In a similar manner, the extinction cross-section is defined by:

$$\sigma_{\text{ext}} = \frac{1}{|\mathbf{P}_{\text{inc}}|} \lim_{R\to\infty} \int_{S(R)} \mathbf{P}_{\text{ext}}(\mathbf{r}) \cdot \mathbf{r} \, \mathrm{d}\Omega.$$

Once again, by using the incident and scattered multipole expansion of the fields together with the orthonormality properties and far-field limits of the VPWs, the extinction cross-section can be cast: [Stout 2001]

$$\sigma_{\text{ext}} = -\frac{1}{k_b^2} \sum_{j=1}^{N} \mathrm{Re}\big[\mathbf{e}_O^{\dagger} \cdot \mathbf{J}(-\mathbf{u}_j)\ \mathbf{f}_j\big]. \tag{D.2}$$

By conservation of energy, the absorption cross-section is given by:

$$\sigma_{\text{abs}} = \sigma_{\text{ext}} - \sigma_{\text{scat}} \tag{D.3}$$

D.2 Decay rate enhancements

D.2.1 Body-centered T-matrices and Green function formulation

The dyadic Green function, $\overleftrightarrow{\mathbf{G}}$, of the antenna contains the information necessary for electromagnetic calculations in that it yields the electric field everywhere via the integral formula[Chew 1990]:

$$\mathbf{E}(\mathbf{x}) = i\omega\mu_0 \int d\mathbf{x}' \, \overleftrightarrow{\mathbf{G}}(\mathbf{x} - \mathbf{x}') \, \mathbf{j}_e(\mathbf{x}') \tag{D.4}$$

We simplify matters by restricting $\overleftrightarrow{\mathbf{G}}(\mathbf{x} - \mathbf{x}')$ to situations where both the source current positions, $\mathbf{x}'$, and 'receptor' positions, $\mathbf{x}$, are located within the host medium. The Green function can then be separated into an 'unperturbed' Green function of the homogeneous exterior medium Green function, $\overleftrightarrow{\mathbf{G}}_0$, plus a 'scattering' contribution, $\overleftrightarrow{\mathbf{G}}_{\text{s}}$[Chew 1990, Novotny 2006]:

$$\overleftrightarrow{\mathbf{G}}(\mathbf{x}, \mathbf{x}') = \overleftrightarrow{\mathbf{G}}_0(\mathbf{x}, \mathbf{x}') + \overleftrightarrow{\mathbf{G}}_{\text{s}}(\mathbf{x}, \mathbf{x}') \tag{D.5}$$

The homogeneous, 'unperturbed' Green function is translationally invariant and satisfies the equation:

$$\nabla \times \nabla \times \overleftrightarrow{\mathbf{G}}_0(\mathbf{x} - \mathbf{x}') - k_b^2 \overleftrightarrow{\mathbf{G}}_0(\mathbf{x} - \mathbf{x}') = \overleftrightarrow{\mathbb{I}} \, \delta^3(\mathbf{x} - \mathbf{x}') \tag{D.6}$$

where $k_b = (\omega/c)\sqrt{\varepsilon_b}$ is the wavenumber of the exterior medium. A technical difficulty is that $\overleftrightarrow{\mathbf{G}}_0$ is singular at the origin, but this has been studied in detail and one can show that $\overleftrightarrow{\mathbf{G}}_0$ can be well defined provided that we treat it as a

distribution and take care in treating the limit $\mathbf{x} \to \mathbf{x}'$.[Chew 1990] Expressing $\overleftrightarrow{\mathbf{G}}_0$ in direct space with $\mathbf{r} \equiv \mathbf{x} - \mathbf{x}'$, one has[?, Novotny 2006]:

$$\overleftrightarrow{\mathbf{G}}_0(\mathbf{r}) = \frac{e^{ik_b r}}{4\pi k_b^2 r^3}\text{P.V.}\left\{(1-ik_b r)\left(3\widehat{\mathbf{rr}} - \overleftrightarrow{\mathbf{Id}}\right) + k_b^2 r^2\left(\overleftrightarrow{\mathbf{Id}} - \widehat{\mathbf{rr}}\right)\right\} - \frac{\overleftrightarrow{\mathbf{Id}}}{3k_b^2}\delta^3(\mathbf{r}) \tag{D.7}$$

where P.V. stands for principal value. As explained in ref.[Chew 1990], the 3D delta function term depends on the exclusion volume chosen for the principal value. The formula presented here corresponds to a principal value chosen as either a spherical or cubic infinitesimal volume around the source point. Replacing the total Green function in eq.(D.4) with the homogeneous Green function of (D.7) yields the electric field, $\mathbf{E}_0$, produced by an isolated point dipole:

$$\mathbf{E}_0(\mathbf{x}) = \frac{e^{ik_b r}}{4\pi\varepsilon_b\varepsilon_0 r^3}\left\{(1-ik_b r)\left[3\widehat{\mathbf{r}}\left(\widehat{\mathbf{r}}\cdot\mathbf{p}_e\right) - \mathbf{p}_e\right] + k_b^2 r^2\left[\mathbf{p}_e - \widehat{\mathbf{r}}\left(\widehat{\mathbf{r}}\cdot\mathbf{p}_e\right)\right]\right\} - \frac{\mathbf{p}_e}{3\varepsilon_b\varepsilon_0}\delta^3(\mathbf{r}) \tag{D.8}$$

The information coming from the antenna structure is embodied in the scattering part of the total Green function, $\overleftrightarrow{\mathbf{G}}_\text{s}$. The scattering Green function, $\overleftrightarrow{\mathbf{G}}_\text{s}$, must take into account the multiple scattering of the emitter radiation from all the N components of the antenna structure. For the purpose of calculation, it is advantageous to express the scattering Green function in terms of a multiple scattering T-matrix which we define in operator notation as:

$$\overleftrightarrow{\mathbf{G}}_\text{s} = \overleftrightarrow{\mathbf{G}}_0\left(\sum_{i=1,j=1}^{N}\overleftrightarrow{\mathbf{T}}^{(i,j)}\right)\overleftrightarrow{\mathbf{G}}_0 \tag{D.9}$$

where i and j are particle labels. The multiple scattering T-matrix, $\mathbf{T}$, has thus been split up into N^2 operators, $\overleftrightarrow{\mathbf{T}}^{(i,j)}$, that we call "body-centered T-matrices": [Stout 2002, Stout 2011]

$$\mathbf{T} = \begin{bmatrix} \mathbf{T}_N^{(1,1)} & \mathbf{T}_N^{(1,2)} & \cdots & \mathbf{T}_N^{(1,N)} \\ \mathbf{T}_N^{(2,1)} & \mathbf{T}_N^{(2,2)} & \cdots & \mathbf{T}_N^{(2,N)} \\ \vdots & \vdots & \ddots & \vdots \\ \mathbf{T}_N^{(N,1)} & \mathbf{T}_N^{(N,2)} & \cdots & \mathbf{T}_N^{(N,N)} \end{bmatrix} \tag{D.10}$$

From a multiple scattering viewpoint, one can visualize each $\overleftrightarrow{\mathbf{T}}^{(i,j)}$ as representing all multiple scattering events in which the first particle encountered by incident radiation is j and the last particle to be encountered is i.

D.2.2 Multipole formulas for Decay rate enhancements

The total emitted power is evaluated by time averaging $P_\text{t} \equiv -\mathbf{E}_\text{t}\cdot\mathbf{j}_\text{src}$ over a period, where $\mathbf{E}_\text{t}$ is the electric field produced by the source current while taking into account interactions with the antenna structure. Averaging this power over a

period, $T = 2\pi/\omega$, we obtain [Novotny 2006]:

$$\Gamma_{\mathrm{t}} \equiv -\frac{1}{T}\int_0^T dt \int d\mathbf{x}\, \mathbf{E}_{\mathrm{t}}\left(\mathbf{x},t\right)\cdot\mathbf{j}_e\left(\mathbf{x},t\right) = \frac{\omega^3}{2}\mu_0\,\mathrm{Im}\left\{\mathbf{p}_e^*\left(\mathbf{x}_j\right)\cdot\overleftrightarrow{\mathbf{G}}\left(\mathbf{x}_j,\mathbf{x}_j\right)\cdot\mathbf{p}_e\left(\mathbf{x}_j\right)\right\} \tag{D.11}$$

Some of the power emanating from the dipole emitter will be dissipated by the antenna. The rest will be radiated off into the far field where it can be detected. The calculation of the radiated power proceeds by first taking the far-field limit of the electric field given by eq.(D.4). The electric field is transverse in the far-field limit, and we can readily obtain the **H** field from the electric field via the relation [Bohren 1983]:

$$\lim_{r\to\infty}\mathbf{H}_{\mathrm{t}}\left(\mathbf{r}\right) = \frac{k_b}{\mu_0\omega}\widehat{\mathbf{r}}\times\mathbf{E}_{\mathrm{t}}$$

In the $r\to\infty$ limit, the time averaged Poynting vector is thus:

$$\lim_{r\to\infty}\langle\mathbf{S}\rangle = \lim_{r\to\infty}\frac{1}{2}\mathrm{Re}\left\{\mathbf{E}_{\mathrm{t}}^*\times\mathbf{H}_{\mathrm{t}}\right\} = \frac{1}{2}\frac{k_b}{\omega\mu_0}\widehat{\mathbf{r}}\left\|\mathbf{E}_{\mathrm{t}}\right\|^2 \tag{D.12}$$

The far-field irradiance, $I_{\mathrm{r}}(\theta,\phi)$, and total radiated power are defined respectively by:

$$I_{\mathrm{r}}\left(\theta,\phi\right) \equiv \lim_{r\to\infty} r^2\langle\mathbf{S}\rangle\cdot\widehat{\mathbf{r}} \qquad \text{and} \qquad \Gamma_{\mathrm{r}} \equiv \int I_{\mathrm{r}}\left(\theta,\phi\right)\,\mathrm{d}\Omega \tag{D.13}$$

In order to determine the modifications to Γ_{t}, $I_{\mathrm{r}}\left(\theta,\phi\right)$, and Γ_{r} induced by the antenna, we will need to normalize these values with respect to the corresponding quantities of an isolated emitter placed inside the homogeneous background. In this case, the analytical expressions for the field and homogeneous Green function of eqs.(D.7) and (D.8) yield the textbook results for dipole emission in a homogeneous medium. Notably, the power emitted in a homogeneous dielectric medium is:

$$\Gamma_{\mathrm{t},0} = \frac{\omega^3}{2}\mu_0\,\mathrm{Im}\left\{\mathbf{p}_e^*\left(\mathbf{x}_j\right)\cdot\overleftrightarrow{\mathbf{G}}_0\left(\mathbf{x}_j,\mathbf{x}_j\right)\cdot\mathbf{p}_e\left(\mathbf{x}_j\right)\right\} = \left|\mathbf{p}_e\right|^2\frac{\omega^3}{12\pi\varepsilon_0 c^2}\,\mathrm{Re}\left\{k_b\right\}$$

The classic far-field radiation pattern and radiated power, Γ_0, are readily obtained from eq.(D.8) applied to eqs.(D.12) and (D.13):

$$I_{\mathrm{r},0}\left(\widehat{\mathbf{r}}\right) = \frac{\omega^3 k_b}{32\pi^2\varepsilon_0 c^2}\left(1-\left(\widehat{\mathbf{r}}\cdot\widehat{\mathbf{p}}_e\right)^2\right)\left|\mathbf{p}_e\right|^2, \quad \Gamma_0 \equiv \int d\Omega\, I_{\mathrm{r},0}\left(\theta,\phi\right) = \left|\mathbf{p}_e\right|^2\frac{\omega^3 k_b}{12\pi\varepsilon_0 c^2} \tag{D.14}$$

The purpose of this section is to generalize the analytic expressions for emitted and radiated powers to the case in which the emitter is located near a nano-antenna structure. We saw in the previous section that the multiple-scattering T-matrix determines the scattering Green function (equation D.9). The scattering Green function can then be expressed on the VPW basis, provided that we also express the homogeneous Green function on the VPW basis. Taking advantage of the translational invariance of $\overleftrightarrow{\mathbf{G}}_0\left(\mathbf{x},\mathbf{x}'\right)$, it can be written [Chew 1990]:

$$\overleftrightarrow{\mathbf{G}}_0\left(\mathbf{r},\mathbf{0}\right) = ik_b\sum_{m=-1}^{1}\mathbf{N}_{1,m}^{\mathrm{in}}\left(k_b\mathbf{r}\right)\mathbf{N}_{1,m}^{\mathrm{out}}\left(0\right) - \frac{\widehat{\mathbf{r}}\widehat{\mathbf{r}}}{k_b^2}\delta\left(\mathbf{r}\right) \tag{D.15}$$

Employing this expression in eq.(D.4), the unperturbed electric field created by an isolated point dipole, denoted $\mathbf{E}_0$, is then expressed:

$$\mathbf{E}_0(\mathbf{x}) = \omega^2\mu_0 \int d\mathbf{x}' \overleftrightarrow{\mathbf{G}}_0(\mathbf{x},\mathbf{x}') \cdot \mathbf{p}_e\, \delta^3(\mathbf{x}') = \frac{ik_b\omega^2 p_e}{\varepsilon_0 c^2} \sum_{m=-1}^{1} \mathbf{N}_{1m}(k_b\mathbf{x})\, f_{2,1,m}$$

where we define the outgoing dipole field coefficients, $f_{q=2,n=1,m}$, to be given by

$$f_{2,1,m} \equiv \mathbf{N}^{\text{out}}_{1,m}(0) \cdot \widehat{\mathbf{n}}$$

and $\widehat{\mathbf{n}}$ is the unit vector in the direction of the emitter dipole moment, defined such that $\mathbf{p}_e = p_e\widehat{\mathbf{n}}$. All other emitter multipoles, $n > 1$ or $q \neq 2$, are null. Utilizing the analytical expression for $\mathbf{N}^{\text{out}}_{1,m}(0)$, we obtain the following expressions for the emitter field coefficients:

$$\begin{aligned} f_{q,n,0} &= \delta_{q,2}\delta_{n,1}\sqrt{\frac{1}{6\pi}}\widehat{\mathbf{z}} \cdot \widehat{\mathbf{n}}, \\ f_{q,n,1} &= \frac{\delta_{q,2}\delta_{n,1}}{2\sqrt{3\pi}}(-\widehat{\mathbf{x}} + i\widehat{\mathbf{y}}) \cdot \widehat{\mathbf{n}}, \\ f_{q,n,-1} &= \frac{\delta_{q,2}\delta_{n,1}}{2\sqrt{3\pi}}(\widehat{\mathbf{x}} + i\widehat{\mathbf{y}}) \cdot \widehat{\mathbf{n}} \end{aligned}$$

Employing expression (D.15) for $\overleftrightarrow{\mathbf{G}}_0$ in eqs.(D.9), (D.5) and (D.4) of the previous section and invoking the translation-addition theorem, we obtain an entirely multipolar expression for the field radiated by a dipole emitter interacting with an antenna structure: [Stout 2011]

$$\begin{aligned} \mathbf{E}_{\text{t}}(\mathbf{r}) = \mathbf{E}_0 + \mathbf{E}_{\text{s}} &= \frac{ip_e k_b\omega^2}{\varepsilon_0 c^2}\left[\mathbf{N}(\mathbf{r})\, f + \sum_{j,l=1}^{N} \left[\mathbf{M}(k\mathbf{r}_j), \mathbf{N}(k\mathbf{r}_j)\right] T^{(j,l)}\, H^{(l,e)}\, f\right] \\ &\equiv \frac{ip_e k_b\omega^2}{\varepsilon_0 c^2}\widetilde{\mathbf{E}}_{\text{t}}(\mathbf{r}) \end{aligned} \tag{D.16}$$

where f denotes a column matrix containing the emitter coefficients in the multipole space (with only electric dipole elements non-zero) and $H^{(l,e)} \equiv H(k_b(\mathbf{x}_l - \mathbf{x}_e))$ are the irregular translation-addition matrices between the position of particle l and the emitter position.

In the second line of eq.(D.16), we defined a dimensionless field, $\widetilde{\mathbf{E}}_{\text{t}}$, proportional to the total electric field. This definition of $\widetilde{\mathbf{E}}_{\text{t}}$ proves convenient when normalizing the antenna irradiance, $I_{\text{r}}(\theta,\phi)$, with respect to $\Gamma_0/(4\pi)$ of the isolated emitter. Using the definition of eq.(D.16) in eqs.(D.12) and (D.13), and dividing by the irradiance of the isolated emitter (eq. D.14), the normalized irradiance is given by:

$$\widetilde{I}_{\text{r}} \equiv \frac{4\pi I_{\text{r}}(\theta,\phi)}{\Gamma_0} = 24\pi^2 \lim_{r\to\infty} (k_b r)^2 \left\|\widetilde{\mathbf{E}}_{\text{t}}(\mathbf{r})\right\|^2 \tag{D.17}$$

The electric field of eq.(D.16), can then be utilized in equation (D.11) to obtain the total decay rate enhancement factor: [Stout 2011]

$$\widetilde{\Gamma}_{\mathrm{t}} \equiv \frac{\Gamma_{\mathrm{t}}}{\Gamma_{\mathrm{t},0}} = 1 + \frac{\mathrm{Re}\left\{6\pi k_b \sum_{j,l=1}^{N} f^{\dagger}\, H^{(e,j)}\, T^{(j,l)}\, H^{(l,e)}\, f\right\}}{\mathrm{Re}\left\{k_b\right\}} \tag{D.18}$$

Likewise, the enhancement in radiative decay rate is obtained by inserting eq.(D.16) into eqs.(D.12) and (D.13). Utilizing the translation-addition theorem and the orthogonality properties of the vector spherical harmonics, one obtains for the radiative decay rate enhancement: [Stout 2011]

$$\begin{aligned}\widetilde{\Gamma}_{\mathrm{r}} \equiv \frac{\Gamma_{\mathrm{r}}}{\Gamma_0} = 1 + 6\pi \sum_{i,j,k,l=1}^{N} \left[T^{(j,i)}\, H^{(i,e)}\, f\right]^{\dagger}\, J^{(j,k)}\, T^{(k,l)}\, H^{(l,e)}\, f \\ + 12\pi\, \mathrm{Re}\left[\sum_{j,l=1}^{N} f^{\dagger}\, J^{(e,j)}\, T^{(j,l)}\, H^{(l,e)}\, f\right]\end{aligned} \tag{D.19}$$

where we see that eqs.(D.19) and (D.18) required the use of both regular, $\mathbf{J}$, and irregular, $\mathbf{H}$, translation-addition matrices (see section C.1).

The multiple-scattering results of eqs.(D.18) and (D.19) simplify considerably when a single antenna particle is present: [Stout 2011]

$$\widetilde{\Gamma}_{\mathrm{t}} = 1 + \frac{\mathrm{Re}\left\{6\pi k_b f^{\dagger}\, H^{(e,j)}\, t\, H^{(j,e)}\, f\right\}}{\mathrm{Re}\left\{k_b\right\}} \tag{D.20}$$

and

$$\widetilde{\Gamma}_{\mathrm{r}} = 1 + 6\pi \left[H^{(j,e)}\, f\right]^{\dagger}\, t^{\dagger}\, t\, H^{(j,e)}\, f + 12\pi\, \mathrm{Re}\left[f^{\dagger}\, J^{(e,j)}\, t\, H^{(j,e)}\, f\right] \tag{D.21}$$

where t is the single-particle T-matrix. If the T-matrix is that of a spherical (Mie) scatterer, then eqs.(D.20) and (D.21) are equivalent to expressions that were derived previously for Mie scatterers.[Kerker 1980, Ruppin 1982, Kim 1988, Colas des Francs 2008]

Appendix E

Dipole and quadripole models derivation

E.1 Electric dipole dimer illuminated from the far-field

E.1.1 Effective polarizabilities

Using eq. (2.5), the field scattered by the sphere $j = 1, 2$ at the center of the sphere $i = 2, 1$ is:

$$\mathbf{E}^{(j)}_{\text{scat}}(\mathbf{r}_i) = \frac{e^{ikd}}{4\pi\varepsilon_m\varepsilon_0 d^3}\left\{k^2d^2(\hat{\mathbf{r}}_i\times\mathbf{p}^{(j)})\times\hat{\mathbf{r}}_i + (1-ikd)\big[3(\hat{\mathbf{r}}_i\cdot\mathbf{p}^{(j)})\hat{\mathbf{r}}_i - \mathbf{p}^{(j)}\big]\right\},$$

where $\hat{\mathbf{r}}_i$ is the unit vector pointing from sphere j to sphere i. In the transverse case, $\hat{\mathbf{r}}_l\cdot\mathbf{p} = 0$ and $(\hat{\mathbf{r}}_l\times\mathbf{p})\times\hat{\mathbf{r}}_l = \mathbf{p}$, whereas in the longitudinal case, $\hat{\mathbf{r}}_l\cdot\mathbf{p} = p$ and $\hat{\mathbf{r}}_l\times\mathbf{p} = 0$ (hence there is no "far field" *i.e.* $\propto k^2d^2$ term in the longitudinal case), and we have:

$$\mathbf{E}^{(j)}_{\text{scat,T}}(\mathbf{r}_i) = \frac{e^{ikd}}{4\pi\varepsilon_m\varepsilon_0 d^3}(1-ikd+k^2d^2)\mathbf{p}^{(j)},$$
$$\mathbf{E}^{(j)}_{\text{scat,L}}(\mathbf{r}_i) = \frac{e^{ikd}}{4\pi\varepsilon_m\varepsilon_0 d^3}(ikd-1)\mathbf{p}^{(j)}.$$

Using the notation γ as defined in eqs. (2.7a) and (2.7b), we then deduce eqs. (2.6a) and (2.6b) from the definition of the excitation fields ($E^{(j)}_{\text{exc}} \equiv [\mathbf{E}_{\text{inc}}(x_j) + \mathbf{E}^{(i)}_{\text{scat}}(x_j)]\cdot\hat{\mathbf{z}}$). Those coupled equations can also be written:

$$\begin{aligned}
E^{(1)}_{\text{exc}} &= E^{(1)}_{\text{inc}} + \gamma(E^{(2)}_{\text{inc}} + \gamma E^{(1)}_{\text{exc}})\\
E^{(1)}_{\text{exc}}(1-\gamma^2) &= E^{(1)}_{\text{inc}}(1+\gamma E^{(2)}_{\text{inc}}/E^{(1)}_{\text{inc}})\\
E^{(1)}_{\text{exc}} &= E^{(1)}_{\text{inc}}\frac{1+\gamma E^{(2)}_{\text{inc}}/E^{(1)}_{\text{inc}}}{1-\gamma^2}\\
E^{(2)}_{\text{exc}} &= E^{(2)}_{\text{inc}}\frac{1+\gamma E^{(1)}_{\text{inc}}/E^{(2)}_{\text{inc}}}{1-\gamma^2}.
\end{aligned}$$

We define the 'effective' polarizabilities as:

$$\begin{aligned}
\mathbf{p}^{(j)}(\omega) &= \varepsilon_0\varepsilon_m\alpha(\omega)E^{(j)}_{\text{exc}}(\omega)\hat{\mathbf{z}}\\
&= \varepsilon_0\varepsilon_m\alpha(\omega)E^{(j)}_{\text{inc}}\frac{E^{(j)}_{\text{exc}}}{E^{(j)}_{\text{inc}}}(\omega)\hat{\mathbf{z}}\\
&\equiv \varepsilon_0\varepsilon_m\alpha^{(j)}_{\text{eff}}(\omega)E^{(j)}_{\text{inc}}(\omega)\hat{\mathbf{z}},
\end{aligned}$$

to obtain:

$$\alpha_{\text{eff}}^{(j)} = \alpha \frac{1 + \gamma E_{\text{inc}}^{(i)}/E_{\text{inc}}^{(j)}}{1-\gamma^2},$$

from which we deduce eqs. (2.8a) to (2.8d).

E.1.2 Scattering cross-sections

To obtain an analytical expression of the scattering cross-section, we now have to find an expression of the fields in the far-field limit. Using:

$$\begin{aligned}
\hat{\mathbf{z}} &= \cos(\theta)\hat{\mathbf{r}} + \sin(\theta)\hat{\theta}, \\
|\mathbf{r} - \mathbf{x}^{(j)}| &= \left[(x - x^{(j)})^2 + y^2 + z^2\right]^{1/2} \\
&\approx (r^2 - 2xx^{(j)})^{1/2} = r\left(1 - \frac{2xx^{(j)}}{r^2}\right)^{1/2} \\
&\approx r - x^{(j)}\sin(\theta)\cos(\phi) \equiv r - \beta_{\text{T}}^{(j)}, \\
|\mathbf{r} - \mathbf{z}^{(j)}| &\approx r - z^{(j)}\cos(\theta) \equiv r - \beta_{\text{L}}^{(j)},
\end{aligned}$$

we obtain:

$$\begin{aligned}
\lim_{\mathbf{r}\to\infty} \mathbf{E}_{\text{scat}}^{(j)}(\mathbf{r}) &= (\omega/c)^2 \frac{\mathrm{e}^{ik|\mathbf{r}-\mathbf{x}^{(j)}|}}{4\pi\varepsilon_0 r}(\hat{\mathbf{z}} - \hat{\mathbf{r}}\cos\theta)p^{(i)} \\
&= (\omega/c)^2 \frac{\mathrm{e}^{ikr}\mathrm{e}^{-ik\beta^{(j)}}}{4\pi\varepsilon_0 r}(\hat{\mathbf{z}} - \hat{\mathbf{r}}\cos\theta)p^{(i)} \\
&= (\omega/c)^2 \frac{\mathrm{e}^{ikr}\mathrm{e}^{-ik\beta^{(j)}}}{4\pi\varepsilon_0 r} p^{(i)}\sin\theta\hat{\theta},
\end{aligned}$$

which yields the total scattered electric and magnetic fields $\mathbf{E}(\mathbf{r})$ and $\mathbf{H}(\mathbf{r})$ in the far-field:

$$\begin{aligned}
\mathbf{E}(\mathbf{r}) &= (\omega/c)^2 \frac{\mathrm{e}^{ikr}}{4\pi\varepsilon_0 r}\left(\sum_{j=1}^{2} p^{(j)}\mathrm{e}^{-ik\beta^{(j)}}\right)\sin\theta\hat{\theta}, \\
\mathbf{H}(\mathbf{r}) &= \omega k \frac{\mathrm{e}^{ikr}}{4\pi r}\left(\sum_{j=1}^{2} p^{(j)}\mathrm{e}^{-ik\beta^{(j)}}\right)\sin\theta\hat{\phi}.
\end{aligned}$$

We then have the time-averaged far-field Poynting vector $\mathbf{P}(\mathbf{r})$:

$$\begin{aligned}
\mathbf{P}(\mathbf{r}) &= \frac{1}{2}\Re\left[(\mathbf{E})^* \wedge \mathbf{H}\right] \\
&= \frac{\sin^2(\theta)\omega^3 k}{32\pi^2\varepsilon_0 c^2 r^2}\left[|p^{(1)}|^2 + |p^{(2)}|^2 + 2\Re(p^{(1)}(p^{(2)})^*\mathrm{e}^{ik(\beta^{(2)}-\beta^{(1)})})\right]\hat{\mathbf{r}}.
\end{aligned}$$

Given the incident field irradiance $\mathbf{P}_{\text{inc}} = \frac{1}{2}|E_0|^2(\varepsilon_m\varepsilon_0/\mu_0)^{1/2}\hat{\mathbf{z}}$, we can now write the differential scattering cross-section (see *e.g.* [Bohren 1983]):

$$\begin{aligned}
\frac{\mathrm{d}^2\sigma}{\mathrm{d}^2\Omega}(\theta,\phi) &\equiv \lim_{r\to\infty} r^2\hat{\mathbf{r}}\cdot\frac{\mathbf{P}(\mathbf{r})}{|\mathbf{P}_{\text{inc}}|} \\
&= \frac{k^4}{16\pi^2E_0^2}\sin^2\theta\Big\{|\alpha_{\text{eff}}^{(1)}E_{\text{inc}}^{(1)}|^2 + |\alpha_{\text{eff}}^{(2)}E_{\text{inc}}^{(2)}|^2 + 2\Re[\alpha_{\text{eff}}^{(1)}E_{\text{inc}}^{(1)}(\alpha_{\text{eff}}^{(2)}E_{\text{inc}}^{(2)})^*\mathrm{e}^{ik(\beta^{(2)}-\beta^{(1)})}]\Big\}, \\
\sigma_{\text{scat}} &= \int\frac{\mathrm{d}^2\sigma}{\mathrm{d}^2\Omega}(\theta,\phi)\mathrm{d}\Omega \\
&= \iint_S\frac{\mathrm{d}^2\sigma}{\mathrm{d}^2\Omega}(\theta,\phi)\sin\theta\mathrm{d}\theta\mathrm{d}\phi \\
&= \frac{k^4}{16\pi^2E_0^2}\Big[2\pi(|\alpha_{\text{eff}}^{(1)}E_{\text{inc}}^{(1)}|^2 + |\alpha_{\text{eff}}^{(2)}E_{\text{inc}}^{(2)}|^2)\int_0^\pi\sin^3\theta\mathrm{d}\theta \\
&\quad + 2\iint_S\sin^3\theta\mathrm{d}\theta\mathrm{d}\phi\Re[\alpha_{\text{eff}}^{(1)}E_{\text{inc}}^{(1)}(\alpha_{\text{eff}}^{(2)}E_{\text{inc}}^{(2)})^*\mathrm{e}^{ik(\beta^{(2)}-\beta^{(1)})}]\Big],
\end{aligned}$$

where S stands for the solid angle space ($\theta\in[0,\pi]$, $\phi\in[0,2\pi]$). Let us consider the term:

$$B = \iint_S\sin^3\theta\ \Re[\alpha_{\text{eff}}^{(1)}E_{\text{inc}}^{(1)}(\alpha_{\text{eff}}^{(2)}E_{\text{inc}}^{(2)})^*\mathrm{e}^{ik(\beta^{(2)}-\beta^{(1)})}]\mathrm{d}\theta\mathrm{d}\phi.$$

At this point, we must calculate separately the B term for the three different illuminations. We first derive the $k_\parallel$ term:

$$\begin{aligned}
B_{k_\parallel} &= \iint_S\sin^3\theta\ \Re[\alpha_{\text{eff},k_\parallel}^{(1)}E_0^2\mathrm{e}^{-ikd}(\alpha_{\text{eff},k_\parallel}^{(2)})^*\mathrm{e}^{ikd\sin\theta\cos\phi}]\mathrm{d}\theta\mathrm{d}\phi \\
&= E_0^2\int_0^\pi\sin^3\theta\ \Re[\alpha_{\text{eff},k_\parallel}^{(1)}\mathrm{e}^{-ikd}(\alpha_{\text{eff},k_\parallel}^{(2)})^*\int_0^{2\pi}\mathrm{e}^{ikd\sin\theta\cos\phi}\mathrm{d}\phi\mathrm{d}\theta.
\end{aligned}$$

Here we use the ordinary regular Bessel function of zeroth order J_0 and the fact that it is an even function:

$$\begin{aligned}
J_0(x) = J_0(-x) &= \frac{1}{2\pi}\int_0^{2\pi}\mathrm{e}^{ix\cos\phi}\mathrm{d}\phi \\
B_{k_\parallel} &= 2\pi E_0^2\int_0^\pi\sin^3\theta\ \Re[\alpha_{\text{eff},k_\parallel}^{(1)}\mathrm{e}^{-ikd}(\alpha_{\text{eff},k_\parallel}^{(2)})^*J_0(kd\sin\theta)]\mathrm{d}\theta \\
&= 4\pi E_0^2\Re[\alpha_{\text{eff},k_\parallel}^{(1)}\mathrm{e}^{-ikd}(\alpha_{\text{eff},k_\parallel}^{(2)})^*]\int_0^{\pi/2}\sin^3\theta J_0(kd\sin\theta)\mathrm{d}\theta.
\end{aligned}$$

Despite our efforts, we did not find the above integral calculated 'as is' in literature. We thus used a handbook formula from [Abramowitz 1972], equation 11.4.10 :

$$\int_0^{\pi/2}J_\mu(z\sin t)\sin^{\mu+1}t\cos^{2\nu+1}t\mathrm{d}t = \frac{2^\nu\Gamma(\nu+1)}{z^{\nu+1}}J_{\mu+\nu+1}(z),$$

which is correct as long as $\Re(\mu) > -1$ and $\Re(\nu) > -1$. Using $z = kd$, $\mu = 0$ with $\nu = -1/2$ and $1/2$, the formula yields:

$$\begin{aligned} C &\equiv \int_0^{\pi/2} \sin^3\theta J_0(kd\sin\theta)\mathrm{d}\theta \\ &= \int_0^{\pi/2} \sin\theta J_0(kd\sin\theta)\mathrm{d}\theta - \int_0^{\pi/2} \sin\theta\cos^2\theta J_0(kd\sin\theta)\mathrm{d}\theta \\ &= \frac{\Gamma(1/2)}{(2kd)^{1/2}} J_{1/2}(kd) - \frac{\sqrt{2}\Gamma(3/2)}{(kd)^{3/2}} J_{3/2}(kd) \\ &= j_0(kd) - \frac{j_1(kd)}{kd}, \end{aligned}$$

where we used j_0 and j_1 the spherical Bessel functions of order 0 and 1, which have analytical formulas in terms of usual functions:

$$\begin{aligned} j_0(x) &= \frac{\sin x}{x}, \\ j_1(x) &= \frac{\sin x}{x^2} - \frac{\cos x}{x}. \end{aligned}$$

We obtain:

$$B_{k_\parallel} = 4\pi E_0^2 \Re[\alpha^{(1)}_{\mathrm{eff},k_\parallel} \mathrm{e}^{-ikd} (\alpha^{(2)}_{\mathrm{eff},k_\parallel})^*] \left[\sin(kd)(\frac{1}{kd} - \frac{1}{(kd)^3}) + \frac{\cos(kd}{(kd)^2} \right].$$

The calculus are identical for the $\mathrm{T}, \mathrm{k} \perp$ case:

$$B_{\mathrm{H}_\parallel} = 4\pi E_0^2 |\alpha_{\mathrm{eff},\mathrm{H}_\parallel}|^2 \left[\sin(kd)(\frac{1}{kd} - \frac{1}{(kd)^3}) + \frac{\cos(kd}{(kd)^2} \right].$$

The integration of the B term for the $(E_\parallel)$ illumination is easier:

$$\begin{aligned} B_{\mathrm{E}_\parallel} &= \iint_S \sin^3\theta \ \Re[\alpha^{(1)}_{\mathrm{eff},\mathrm{E}_\parallel} E_0^2 (\alpha^{(2)}_{\mathrm{eff},\mathrm{E}_\parallel})^* \mathrm{e}^{ikd\cos\theta}] \mathrm{d}\theta\mathrm{d}\phi \\ &= 2\pi E_0^2 |\alpha_{\mathrm{eff},\mathrm{E}_\parallel}|^2 \int_0^\pi \sin^3\theta\cos(kd\cos\theta)\mathrm{d}\theta \\ &= 2\pi E_0^2 |\alpha_{\mathrm{eff},\mathrm{E}_\parallel}|^2 \int_{-1}^1 (1-u^2)\cos(kdu)\mathrm{d}u \\ &= 2\pi E_0^2 |\alpha_{\mathrm{eff},\mathrm{E}_\parallel}|^2 \left\{ -[\frac{u^2}{kd}\sin(kdu)]_{-1}^1 + \int_{-1}^1 \frac{2u}{kd}\sin(kdu)\mathrm{d}u + [\frac{\sin(kdu)}{kd}]_{-1}^1 \right\} \\ &= 2\pi E_0^2 |\alpha_{\mathrm{eff},\mathrm{E}_\parallel}|^2 \left\{ [\frac{-2u\cos(kdu)}{(kd)^2}]_{-1}^1 - \int_{-1}^1 \frac{-2}{(kd)^2}\cos(kdu)\mathrm{d}u \right\} \\ B_{\mathrm{E}_\parallel} &= 8\pi E_0^2 |\alpha_{\mathrm{eff},\mathrm{E}_\parallel}|^2 \left(\frac{\sin(kd)}{(kd)^3} - \frac{\cos(kd)}{(kd)^2} \right). \end{aligned}$$

using:

$$\begin{aligned} \int_0^\pi \sin^3(\theta)\mathrm{d}\theta &= \frac{4}{3}, \\ \sigma_{\mathrm{scat}} &= \frac{k^4}{16\pi^2 E_0^2} \left[2\pi(|\alpha^{(1)}_{\mathrm{eff}} E^{(1)}_{\mathrm{inc}}|^2 + |\alpha^{(2)}_{\mathrm{eff}} E^{(2)}_{\mathrm{inc}}|^2)\frac{4}{3} + 2B \right], \end{aligned}$$

we finally obtain:

$$\sigma_{\mathrm{scat},k_\parallel} = \frac{k^4}{6\pi}\left[|\alpha^{(1)}_{\mathrm{eff},k\parallel}|^2 + |\alpha^{(2)}_{\mathrm{eff},k\parallel}|^2 + 2\Re(\alpha^{(1)}_{\mathrm{eff},k\parallel}(\alpha^{(2)}_{\mathrm{eff},k\parallel})^* \mathrm{e}^{-ikd})\mathrm{A}^{\mathrm{IF,T}}\right],$$
$$\sigma_{\mathrm{scat},\mathrm{H}_\parallel} = \frac{k^4}{3\pi}|\alpha^{(1)}_{\mathrm{eff},\mathrm{H}_\parallel}|^2\left(1+\mathrm{A}^{\mathrm{IF,T}}\right),$$
$$\sigma_{\mathrm{scat},\mathrm{E}_\parallel} = \frac{k^4}{3\pi}|\alpha^{(1)}_{\mathrm{eff},\mathrm{E}_\parallel}|^2\left(1+\mathrm{A}^{\mathrm{IF,L}}\right),$$

which are eqs. (2.11a) to (2.11c).

E.2 Decay rates enhancements of a single particle with induced dipoles and quadripoles

We consider the multipole formulas of the total decay rate enhancement factor, equation D.20:

$$\tilde{\Gamma}_{\mathrm{tot}} = \quad 1 + 6\pi\mathrm{Re}[f^\dagger H^{(\mathrm{em,s})} t H^{(\mathrm{s,em})} f]. \tag{E.1}$$

The antenna consists in a single particle placed in the $+z$ direction with respect to an emitter in transverse ("orbital" number $m = 1$, emitter oriented on the X axis) or longitudinal ($m = 0$, emitter oriented on the Z axis) coupling. In a quadrupolar assumption, we have:

$$f = \begin{bmatrix} e_1 \\ 0 \\ h_1 \\ 0 \end{bmatrix}, \; H^{(\mathrm{em,s})} = \begin{bmatrix} A(kd) & B(kd) \\ B(kd) & A(kd) \end{bmatrix}, \; t = \mathrm{Diag}(c_1^e, c_2^e, c_1^m, c_2^m).$$

The superscripts (em,s) and (s,em) respectively refer to a translation from the emitter to the sphere, and from the sphere to the emitter. The coefficients h_1 (null for an electric emitter) and e_1 (null for a magnetic emitter) are the incident magnetic and electric dipole coefficients, normalized to $1/\sqrt{6\pi}$. The two coupling geometries will involve $A_{n,m,\nu,\mu}$ and $B_{n,m,\nu,\mu}$ matrix blocks, where $[A|B]_{n,m,\nu,\mu}$ is the coupling from the multipole order n with orbital number m, to the multipole order ν with orbital number μ:

$$A^{\mathrm{L}}(kd) = \begin{bmatrix} A_{1,0,1,0} & A_{1,0,2,0} \\ A_{1,0,2,0} & A_{2,0,2,0} \end{bmatrix},$$
$$A^{\mathrm{T}}(kd) = \begin{bmatrix} A_{1,1,1,1} & A_{1,1,2,1} \\ A_{1,1,2,1} & A_{2,1,2,1} \end{bmatrix},$$
$$B^{\mathrm{L}}(kd) = 0,$$
$$B^{\mathrm{T}}(kd) = \begin{bmatrix} B_{1,1,1,1} & B_{1,1,2,1} \\ B_{1,1,2,1} & B_{2,1,2,1} \end{bmatrix}.$$

$$H^{(s,em)} = \begin{bmatrix} A & -B \\ -B & A \end{bmatrix}. \tag{E.2}$$

The right-hand side of equation E.1 can thus be cast:

$$\tilde{\Gamma}^{\mathrm{L,u}}_{\mathrm{tot}} = 1 + \mathrm{Re}[c_1^u (A_{1,0,1,0})^2 + c_2^u (A_{1,0,2,0})^2], \tag{E.3}$$
$$\tilde{\Gamma}^{\mathrm{T,u}}_{\mathrm{tot}} = 1 + \mathrm{Re}[c_1^u (A_{1,1,1,1})^2 + c_2^u (A_{1,1,2,1})^2 - c_1^v (B_{1,1,1,1})^2 - c_2^v (B_{1,1,2,1})^2], \tag{E.4}$$

where u and v refer to electric ($u = e$, $v = m$) or magnetic ($u = m$, $v = e$) emitters. The A and B coefficients can be calculated from their analytic expressions (see appendix C.1.1) with the angles $\theta = \phi = 0$:

$$\begin{aligned}
A_{1,1,1,1} &= \tfrac{1}{2}(\bar{\alpha}^s_{1,1,1,1} + \bar{\alpha}^s_{1,0,1,0}) \\
&= \tfrac{1}{2}(\bar{\alpha}^s_{0,0,0,0} + \tfrac{b^-_{2,0}}{b^+_{0,0}}\bar{\alpha}^s_{2,0,0,0} + \bar{\alpha}^s_{0,0,0,0} + \tfrac{a^-_{2,0}}{a^+_{0,0}}\bar{\alpha}^s_{2,0,0,0}) \\
&= \tfrac{1}{2}(\tfrac{-1}{\sqrt{5}}\bar{\alpha}^s_{2,0,0,0} + 2\bar{\alpha}^s_{0,0,0,0}) \\
&= -\tfrac{1}{2\sqrt{5}}\sqrt{4\pi}Y_{2,0}(0,0)h_2(kd) + \sqrt{4\pi}Y_{0,0}(0,0)h_0(kd) \\
&= -\tfrac{P_2^0(1)}{2}h_2(kd) + P_0^0(1)h_0(kd) \\
&= \tfrac{1}{2}(2h_0(kd) - h_2(kd)) \\
A_{1,1,1,1} &= \tfrac{3i}{2}\tfrac{e^{ikd}}{(kd)^3}(1 - ikd - (kd)^2).
\end{aligned}$$

Similarly, the other coefficients can be cast:

$$\begin{aligned}
B_{1,1,1,1} &= \tfrac{3i}{2}\tfrac{e^{ikd}}{(kd)^2}(kd + i), \\
A_{1,0,1,0} &= -3i\tfrac{e^{ikd}}{(kd)^3}(1 - ikd), \\
A_{1,0,2,0} &= \tfrac{3}{\sqrt{5}}\tfrac{e^{ikd}}{(kd)^4}(5i(kd)^2 - 15kd - 15i), \\
A_{1,1,2,1} &= \tfrac{\sqrt{15}}{2}\tfrac{e^{ikd}}{(kd)^4}(-(kd)^3 - 3i(kd)^2 + 6kd + 6i), \\
B_{1,1,2,1} &= \tfrac{\sqrt{15}}{2}\tfrac{e^{ikd}}{(kd)^3}(-(kd)^2 - 3ikd + 3).
\end{aligned}$$

Equations E.3 and E.4 can thus be cast explicitly:

$$\tilde{\Gamma}^{L,u}_{\mathrm{tot}} = 1 + \mathrm{Re}\left[-9\tfrac{\mathrm{e}^{2ikd}}{(kd)^6}(1 - ikd)^2 c_1^u + 45\tfrac{\mathrm{e}^{2ikd}}{(kd)^8}(ik^2d^2 - 3kd - 3i)^2 c_2^u\right] \tag{E.5}$$
$$\begin{aligned}
\tilde{\Gamma}^{T,u}_{\mathrm{tot}} = 1 + \mathrm{Re}\big[&-\tfrac{9\mathrm{e}^{2ikd}}{4(kd)^6}(1 - ikd - k^2d^2)^2 c_1^u + \tfrac{15\mathrm{e}^{2ikd}}{4(kd)^8}(-k^3d^3 - 3ik^2d^2 + 6kd + 6i)^2 c_2^u \\
&+\tfrac{9\mathrm{e}^{2ikd}}{4(kd)^4}(kd + i)^2 c_1^v - \tfrac{15\mathrm{e}^{2ikd}}{(kd)^6}(-k^2d^2 - 3ikd + 3)^2 c_2^v\big],
\end{aligned} \tag{E.6}$$

E.3 Transverse coupling of a dielectric dipolar sphere to an electric dipole

Let us derive analytical formulas for the Poynting vector in the far field region when an electric dipole emitter is transversely coupled to a dielectric sphere that is

dominantly characterized by electric and magnetic dipole polarizabilities. Fig.E.1 defines the angular coordinates used in thisderivation. The surrounding medium has relative permittivity ε_m and vacuum permeability μ_0. The electric and magnetic fields produced by an electric dipole with dipolar moment denoted $\mathbf{p}$, placed at origin are given by [Jackson 1999]:

$$\mathbf{E}_{\mathrm{p}}(r\hat{\mathbf{r}}) = \frac{e^{ikr}}{4\pi\varepsilon_m\varepsilon_0 r^3}\left[k^2r^2(\hat{\mathbf{r}}\times\mathbf{p})\times\hat{\mathbf{r}} + (1-ikr)(3(\hat{\mathbf{r}}\cdot\mathbf{p})\hat{\mathbf{r}}-\mathbf{p})\right], \quad \text{(E.7)}$$

$$\mathbf{H}_{\mathrm{p}}(r\hat{\mathbf{r}}) = \frac{e^{ikr}}{4\pi n_0 r}ck^2(1+\frac{i}{kr})\hat{\mathbf{r}}\times\mathbf{p}, \quad \text{(E.8)}$$

with n_0 the refractive index of the embedding medium ($\varepsilon_m = n_0^2$), and $c = \sqrt{1/\varepsilon_0\mu_0}$ the vacuum celerity. When $\mathbf{p} = p\exp(i\phi_p)\hat{\mathbf{x}}$, the far field limits are given by:

$$\mathbf{E}_{\mathrm{p,ff}}(r\hat{\mathbf{r}}) = -\frac{e^{ikr}}{4\pi\varepsilon_m\varepsilon_0 r}k^2\sin(\theta_x)p\exp(i\phi_p)\hat{\theta_x}, \quad \text{(E.9)}$$

$$\mathbf{H}_{\mathrm{p,ff}}(r\hat{\mathbf{r}}) = -\frac{e^{ikr}}{4\pi n_0 r}ck^2\sin(\theta_x)p\exp(i\phi_p)\hat{\varphi_x}. \quad \text{(E.10)}$$

When the dipole is displaced by a distance d from the origin on the $\hat{\mathbf{z}}$ axis, its phase in the far-field is modified by the far-field phase shift $\exp(-ikd\cos\theta_z)$[Rolly 2011a] while its amplitude, whose correction is proportional to d/r is not modified in the far-field approximation:

$$\mathbf{E}_{\mathrm{p,ff}}(r\hat{\mathbf{r}},d) = -\frac{e^{ikr}}{4\pi\varepsilon_m\varepsilon_0 r}k^2\sin(\theta_x)p\exp(i\phi_p)\exp(-ikd\cos\theta_z)\hat{\theta_x}, \quad \text{(E.11)}$$

$$\mathbf{H}_{\mathrm{p,ff}}(r\hat{\mathbf{r}},d) = -\frac{e^{ikr}}{4\pi n_0 r}ck^2\sin(\theta_x)p\exp(i\phi_p)\exp(-ikd\cos\theta_z)\hat{\varphi_x}. \quad \text{(E.12)}$$

On the other hand, the field produced by a magnetic dipole with moment $\mathbf{m} = m\exp(i\phi_m)\hat{\mathbf{y}}$ placed at origin is given by [Jackson 1999]:

$$\mathbf{E}_{\mathrm{m}}(r\hat{\mathbf{r}}) = -\frac{e^{ikr}}{4\pi\varepsilon_0 n_0 cr}k^2(1+\frac{i}{kr})\hat{\mathbf{r}}\times\mathbf{m},$$

$$\mathbf{H}_{\mathrm{m}}(r\hat{\mathbf{r}}) = \frac{e^{ikr}}{4\pi r^3}\left[k^2r^2(\hat{\mathbf{r}}\times\mathbf{m})\times\hat{\mathbf{r}} + (1-ikr)(3(\hat{\mathbf{r}}\cdot\mathbf{m})\hat{\mathbf{r}}-\mathbf{m})\right],$$

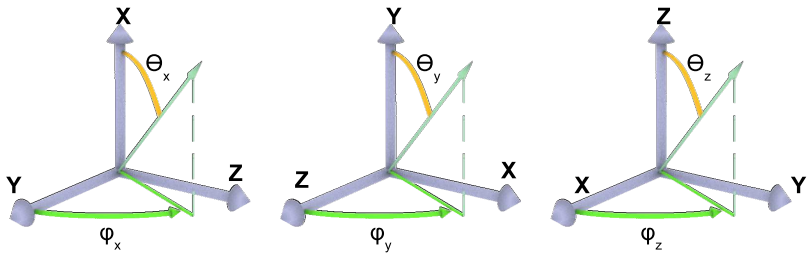

Figure E.1: The angular coordinates system used in this demonstration. The zenith angles θ_{i} and azimuthal angles φ_{i} are defined respectively to the 3 axis, $i = x, y, z$. The choice $i = z$ corresponds to the usual spherical coordinates.

and the far-field contributing terms are:

$$\begin{aligned}\mathbf{E}_{\mathrm{m,ff}}(r\hat{\mathbf{r}}) &= \frac{e^{ikr}}{4\pi\varepsilon_0 n_0 cr}k^2\sin(\theta_y)m\exp(i\phi_m)\hat{\varphi_y},\\ \mathbf{H}_{\mathrm{m,ff}}(r\hat{\mathbf{r}}) &= -\frac{e^{ikr}}{4\pi r}k^2\sin(\theta_y)m\exp(i\phi_m)\hat{\theta_y}.\end{aligned}$$

Similarly to the case of an electric dipole, when the magnetic dipole is displaced by a distance d along the $\hat{\mathbf{z}}$ axis, its phase is modified in the far-field approximation by the term $\exp(-ikd\cos\theta_z)$:

$$\mathbf{E}_{\mathrm{m,ff}}(r\hat{\mathbf{r}},d) = \frac{e^{ikr}}{4\pi\varepsilon_0 n_0 cr}k^2\sin(\theta_y)m\exp(i\phi_m)\exp(-ikd\cos\theta_z)\hat{\varphi_y}, \quad \text{(E.13)}$$

$$\mathbf{H}_{\mathrm{m,ff}}(r\hat{\mathbf{r}},d) = -\frac{e^{ikr}}{4\pi r}k^2\sin(\theta_y)m\exp(i\phi_m)\exp(-ikd\cos\theta_z)\hat{\theta_y}. \quad \text{(E.14)}$$

The amplitude of the emitting electric dipole is taken equal to unity with a phase reference equal to zero: $\mathbf{p}_{\mathrm{em}} = \hat{\mathbf{x}}$. The cartesian directions $+x, +y$ will be the phase references respectively for the electric and magnetic dipoles. Using Eqs. (E.7) and (E.8), the field produced by the emitter at a distance d on the $+\hat{\mathbf{z}}$ direction can be cast:

$$\begin{aligned}\mathbf{E}_0(d\hat{\mathbf{z}}) &= -\frac{e^{ikd}}{4\pi\varepsilon_m\varepsilon_0 d^3}(1-ikd-k^2d^2)\hat{\mathbf{x}},\\ \mathbf{H}_0(d\hat{\mathbf{z}}) &= \frac{e^{ikd}}{4\pi n_0 d^3}c(k^2d^2+ikd)\hat{\mathbf{y}}.\end{aligned}$$

In the case of a spherical, homogeneous scatterers, the polarizabilities are given by Mie theory. We use dimensionless polarizabilities for notational simplicity:

$$\begin{aligned}\tilde{\alpha} = i\frac{3}{2k^3a^3}a_1; \qquad \tilde{\beta} = i\frac{3}{2k^3a^3}b_1,\\ \mathbf{p}_{\mathrm{in}} = 4\pi a^3\varepsilon_0\varepsilon_m\tilde{\alpha}\mathbf{E}_0(d\hat{\mathbf{z}}); \qquad \mathbf{m}_{\mathrm{in}} = 4\pi a^3\tilde{\beta}\mathbf{H}_0(d\hat{\mathbf{z}}).\end{aligned}$$

We then have :

$$\begin{aligned}\mathbf{p}_{\mathrm{in}} &= 4\pi a^3\varepsilon_0\varepsilon_m\tilde{\alpha}\mathbf{E}_0(d\hat{\mathbf{z}})\\ &= -e^{ikd}\Big(\frac{a}{d}\Big)^3(1-ikd-k^2d^2)\tilde{\alpha}\hat{\mathbf{x}}\\ \mathbf{p}_{\mathrm{in}} &= \gamma_e\tilde{\alpha}\hat{\mathbf{x}}, \quad \text{(E.15)}\\ \mathbf{m}_{\mathrm{in}} &= 4\pi a^3\tilde{\beta}\mathbf{H}_0(d\hat{\mathbf{z}})\\ \mathbf{m}_{\mathrm{in}} &= \gamma_m\frac{c}{n_0}\tilde{\beta}\hat{\mathbf{y}}, \quad \text{(E.16)}\end{aligned}$$

where $\gamma_e \equiv -e^{ikd}\frac{a^3}{d^3}(1-ikd-k^2d^2)$ and $\gamma_m \equiv e^{ikd}\frac{a^3}{d^3}(ikd+k^2d^2)$ are dimensionless field coupling factors between the emitter and the electric and magnetic resonance of the sphere, respectively. By summation of the right-hand terms in Eqs. (E.9) to

(E.14), and replacing $\mathbf{p}_{\text{in}}$ and $\mathbf{m}_{\text{in}}$ by their expressions in Eqs. (E.15) and (E.16), the far fields from the 3 dipoles together can be cast:

$$\begin{aligned}
\mathbf{E}_{\text{tot,ff}}(r\hat{\mathbf{r}},d) &= -\frac{e^{ikr}}{4\pi\varepsilon_m\varepsilon_0 r}k^2\Big[(1+\gamma_e\tilde{\alpha}\exp^{-ikd\cos\theta_z})\sin(\theta_x)\hat{\theta_x} \\
&\quad -\gamma_m\tilde{\beta}\sin(\theta_y)\exp(-ikd\cos\theta_z)\hat{\varphi_y}\Big] \\
\mathbf{H}_{\text{tot,ff}}(r\hat{\mathbf{r}},d) &= -\frac{e^{ikr}}{4\pi n_0 r}ck^2\Big[(1+\gamma_e\tilde{\alpha}e^{-ikd\cos\theta_z})\sin(\theta_x)\hat{\varphi_x} \\
&\quad +\gamma_m\tilde{\beta}\sin(\theta_y)e^{-ikd\cos\theta_z}\hat{\theta_y}\Big].
\end{aligned}$$

The time-averaged Poynting vector can be cast :

$$\begin{aligned}
\mathbf{P}(x,y,z,r) &= \frac{1}{2}\Re(\mathbf{E}^*{}_{\text{ff}}\times\mathbf{H}_{\text{ff}}) \\
&= \frac{\omega k^3}{32\pi^2\varepsilon_0\varepsilon_m r^2}\Re\Big[|1+\gamma_e\tilde{\alpha}e^{-ikd\cos\theta_z)}|^2\sin^2(\theta_x)\hat{\theta_x}\times\hat{\varphi_x} \\
&\quad +|\gamma_m\tilde{\beta}|^2\sin^2(\theta_y)\hat{\theta_y}\times\hat{\varphi_y} \\
&\quad +(1+\gamma_e\tilde{\alpha}e^{-ikd\cos\theta_z})^*\sin(\theta_x)\gamma_m\tilde{\beta}\sin(\theta_y)e^{-ikd\cos\theta_z}\hat{\theta_x}\times\hat{\theta_y} \\
&\quad +(\gamma_m\tilde{\beta}e^{-ikd\cos\theta_z})^*\sin(\theta_y)(1+\gamma_e\tilde{\alpha}e^{-ikd\cos\theta_z})\sin(\theta_x)\hat{\varphi_x}\times\hat{\varphi_y}
\end{aligned}$$

$\hat{\theta_x}\times\hat{\varphi_x}$ and $\hat{\theta_y}\times\hat{\varphi_y}$ both equal $\hat{\mathbf{r}}$ since $(\hat{\mathbf{r}},\hat{\theta_i},\hat{\varphi_i})$ is an orthonormal base $(i=x,y,z)$. For notational simplicity we choose to use the reduced cartesian coordinates, *i.e.* the x,y,z coordinates of the unit radial vector $\hat{\mathbf{r}}$. With $(l,m,n)=(x,y,z)$, (y,z,x) or (z,x,y) we have:

$$\begin{gathered}
\cos(\theta_l)=l,\ \sin(\theta_l)=\sqrt{1-l^2}, \\
\cos(\varphi_l)=m/\sqrt{1-l^2},\ \sin(\varphi_l)=n/\sqrt{1-l^2}, \\
\hat{\theta_x}\times\hat{\theta_y}=\tfrac{z}{\sqrt{1-x^2}\sqrt{1-y^2}}\hat{\mathbf{r}}, \\
\hat{\varphi_x}\times\hat{\varphi_y}=\tfrac{z}{\sqrt{1-x^2}\sqrt{1-y^2}}\hat{\mathbf{r}},
\end{gathered}$$

and thus :

$$\begin{aligned}
\mathbf{P}(x,y,z) &= \frac{\omega k^3}{32\pi^2 r^2\varepsilon_0\varepsilon_m}\Big\{(1-x^2)|1+\gamma_e\tilde{\alpha}e^{-ikdz}|^2+(1-y^2)|\gamma_m\tilde{\beta}|^2 \\
&\quad +2z\Re[\gamma_m^*\tilde{\beta}^*e^{ikdz}(1+\gamma_e\tilde{\alpha}e^{-ikdz})]\Big\}\hat{\mathbf{r}}.
\end{aligned} \tag{E.17}$$

E.4 Far-field intensity of an electromagnetic dipoles and quadripoles scatterer

In this section we derive the far-field Poynting vector produced by a scatterer whose far-field response is dominated by its electric and magnetic dipoles and quadrupoles.

The coupling is Transverse: the emitter is oriented on the $\hat{\mathbf{z}}$ axis and the centre of the scatterer is placed at a distance d on the $+x$ axis, $\mathbf{u}_1 = d\hat{\mathbf{x}}$. We first define some coefficients that simplify the display of the equations:

$$\begin{aligned}
e^{i\Phi} &\equiv \exp(-ik\hat{\mathbf{r}}\cdot\mathbf{r_1}) \\
&= \exp(-ikd\sin(\theta)\cos(\varphi)). \\
K_\mathrm{c} &\equiv \tfrac{1}{4\pi\varepsilon_0\varepsilon_m}k^2 \\
K_\mathrm{r} &\equiv \tfrac{e^{ikr}}{r} \\
K &\equiv K_\mathrm{r}K_\mathrm{c} \\
\gamma_1^e &\equiv e^{ikd}(k^2d^2+ikd-1)(a/d)^3 \\
\gamma_1^m &\equiv e^{ikd}(ikd+k^2d^2)(a/d)^3 \\
p_1 &= p_0\gamma_1^e\tilde{\alpha}_1^e \\
m_1 &= p_0\gamma^m\tilde{\alpha}_1^m c/n_0
\end{aligned}$$

In the latter expression, $e^{i\Phi}$ is the the far-field phase shift, K_c is a normalization coefficient and K_r contains the far-field dependence of the fields on the radius r. $\gamma_\mathrm{i}^{\mathrm{e/m}}$ is the dimensionless coupling coefficient between the dipole emitter and the electric/magnetic multipole of order i. p_1 and m_1 are the induced dipolar moments (see previous section).

The fields produced by the dipoles (electric dipolar emitter, electric and induced magnetic dipoles excited in the particle respectively) can be cast, in the local spherical basis:

$$\mathbf{E}_0^{\mathrm{ff}}(r,\theta,\phi) = p_0K\sin(\theta)\hat{\mathbf{e}}_\theta \tag{E.18}$$

$$\mathbf{E}_{\mathrm{d,e}}^{\mathrm{ff}}(r,\theta,\phi) = p_1Ke^{i\Phi}\sin(\theta)\hat{\mathbf{e}}_\theta \tag{E.19}$$

$$\mathbf{E}_{\mathrm{d,m}}^{\mathrm{ff}}(r,\theta,\phi) = m_1Ke^{i\Phi}\tfrac{n_0}{c}(\cos\phi\hat{\mathbf{e}}_\theta - \cos\theta\sin\phi\hat{\mathbf{e}}_\phi) \tag{E.20}$$

The fields produced by both induced quadrupoles can be derived following the method detailed in [Stout 2011]. In order to obtain an excitation field that corresponds to the current notation used in this derivation, the only nonzero coefficient of the incoming field's vector, $\mathbf{f}$, is $f_{\mathrm{n=1,m=0}} = -2i\sqrt{2\pi}p_0K_\mathrm{c}/\sqrt{3}$. The coupling between an electric dipole emitter and the quadrupoles of the scatterer can be cast from the nonzero coefficients of the irregular translation coefficients between the scatterer and the source:

$$\begin{aligned}
A_{2,-1,1,\pi}(kd,\pi/2,\pi) &= -A_{2,1,1,0}(kd,\pi/2,\pi) \\
&= -\sqrt{15}\frac{\exp(ikd)(k^3d^3+3ik^2d^2-6kd-6i)}{2\sqrt{2}(kd)^4} \\
B_{2,-2,1,\pi}(kd,\pi/2,\pi) &= -B_{1,0,2,2}(kd,\pi/2,\pi) \\
&= \sqrt{15}\frac{\exp(ikd)(k^2d^2+3ikd-3)}{2\sqrt{2}(kd)^3}
\end{aligned}$$

with the other $A_{2,\mathrm{m},1,0}(kd,\pi/2,\pi)$ and $B_{2,\mathrm{m},1,0}(kd,\pi/2,\pi)$ equal to zero. The emitter thus couples to the induced quadrupoles, q^e and q^m, and we obtain the coupling

coefficients and the quadrupole moments:

$$\begin{aligned}\gamma_2^e \equiv &\quad -\tfrac{5}{3kd}(k^3d^3+3ik^2d^2-6kd-6i)\tfrac{a^3}{d^3}\\ \gamma_2^m \equiv &\quad \tfrac{5}{3kd}(k^2d^2+3ikd-3)\tfrac{a^3}{d^3}\\ q^e = &\quad p_0\gamma_2^e\tilde{\alpha}_2^e\\ q^m = &\quad p_0\gamma_2^m\tilde{\alpha}_2^m\end{aligned}$$

Their respective electric far-fields if centered at the origin are:

$$\begin{aligned}E_{\mathrm{q,e},0} \equiv &\quad \lim_{r\to\infty}\big[A_{2,-1,1,0}(kd,\pi/2,\pi)\mathbf{N}^{\mathrm{out}}_{2,-1}(r,\theta,\phi)\\ &\quad +A_{2,1,1,0}(kd,\pi/2,\pi)\mathbf{N}^{\mathrm{out}}_{2,1}(r,\theta,\phi)\big]t_2^e f_{1,0}\\ E^{\mathrm{ff}}_{\mathrm{q,e},0} = &\quad Kq^e\bigg(\cos(2\theta)\cos\phi\hat{\mathbf{e}}_\theta-\cos\theta\sin\phi\hat{\mathbf{e}}_\phi\bigg)\\ E_{\mathrm{q,m},0} \equiv &\quad \lim_{r\to\infty}\big[B_{2,-2,1,0}(kd,\pi/2,\pi)\mathbf{M}^{\mathrm{out}}_{2,-2}(r,\theta,\phi)\\ &\quad +B_{2,2,1,0}(kd,\pi/2,\pi)\mathbf{M}^{\mathrm{out}}_{2,2}(r,\theta,\phi)\big]t_2^m f_{1,0}\\ E^{\mathrm{ff}}_{\mathrm{q,m},0} = &\quad Kq^m\bigg(\sin\theta\cos(2\phi)\hat{\mathbf{e}}_\theta-\tfrac{\sin(2\theta)\sin(2\phi)}{2}\hat{\mathbf{e}}_\phi\bigg)\end{aligned}$$

where $\mathbf{N}^{\mathrm{out}}_{n,m}$ and $\mathbf{M}^{\mathrm{out}}_{n,m}$ are the outgoing VPWs. Similarly to dipoles, the quadrupoles are centered at $\mathbf{u}_1$ and their phase experience a modification of $e^{i\Phi}$ in the far field region:

$$\begin{aligned}\mathbf{E}^{\mathrm{ff}}_{\mathrm{q,e}}(r,\theta,\phi) = K\quad & e^{i\Phi}q^e\times\bigg(\cos(2\theta)\cos\phi\hat{\mathbf{e}}_\theta\\ &-\cos\theta\sin\phi\hat{\mathbf{e}}_\phi\bigg)\end{aligned}\tag{E.21}$$

$$\begin{aligned}\mathbf{E}^{\mathrm{ff}}_{\mathrm{q,m}}(r,\theta,\phi) = K\quad & e^{i\Phi}q^m\times\bigg(\sin\theta\cos(2\phi)\hat{\mathbf{e}}_\theta\\ &-\tfrac{\sin(2\theta)\sin(2\phi)}{2}\hat{\mathbf{e}}_\phi\bigg)\end{aligned}\tag{E.22}$$

The total, normalized (respectively to the ED emitter maximum far-field irradiance) far-field irradiance can be cast:

$$\begin{aligned}I(\theta,\phi) &= \frac{1}{p_0^2K^2}|\mathbf{E}^{\mathrm{ff}}_0+\mathbf{E}^{\mathrm{ff}}_{\mathrm{d,e}}+\mathbf{E}^{\mathrm{ff}}_{\mathrm{d,m}}+\mathbf{E}^{\mathrm{ff}}_{\mathrm{q,e}}+\mathbf{E}^{\mathrm{ff}}_{\mathrm{q,m}}|^2\\ &= \bigg|\bigg(\sin\theta(1+e^{i\Phi}\gamma_1^e\tilde{\alpha}_1^e)+e^{i\Phi}\big(\gamma_1^m\tilde{\alpha}_1^m\cos\phi\\ &\quad +\gamma_2^e\cos(2\theta)\cos\phi+\gamma_2^m\sin\theta\cos(2\phi)\big)\bigg)\hat{\mathbf{e}}_\theta\\ &\quad -\bigg(\cos\theta\sin\phi(\tilde{\alpha}_1^m\gamma_1^m+\gamma_2^e\tilde{\alpha}_2^e)\\ &\quad +\frac{1}{2}\gamma_2^m\tilde{\alpha}_2^m\sin(2\theta)\sin(2\phi)\bigg)e^{i\Phi}\hat{\mathbf{e}}_\phi\bigg|^2\end{aligned}$$

Finally we have:

$$
\begin{aligned}
I(\theta,\phi) \quad = \quad & \Big| \sin(\theta)\hat{\mathbf{e}_\theta} + e^{i\Phi}\gamma_1^e\tilde{\alpha}_1^e \sin(\theta)\hat{\mathbf{e}_\theta} \\
& + e^{i\Phi}\gamma_1^m\tilde{\alpha}_1^m(\cos(\phi)\hat{\mathbf{e}_\theta} - \sin(\phi)\cos(\theta)\hat{\mathbf{e}_\phi}) \\
& + e^{i\Phi}\gamma_2^e\tilde{\alpha}_2^e(\cos(\phi)\cos(2\theta)\hat{\mathbf{e}_\theta} - \sin(\phi)\cos(\theta)\hat{\mathbf{e}_\phi}) \\
& + e^{i\Phi}\gamma_2^m\tilde{\alpha}_2^m(\cos(2\phi)\sin(\theta)\hat{\mathbf{e}_\theta} - \frac{\sin(2\phi)\sin(2\theta)}{2}\hat{\mathbf{e}_\phi}) \Big|^2 ,
\end{aligned}
$$

which is equation 3.12 in the main text. In the last equation, each subsequent line stands for the field produced by the emitter, and the induced electric dipole, magnetic dipole, electric quadrupole, and magnetic quadrupole respectively.

Glossary and Acronyms

dBi Isotropic decibel. See equation 1.13. 18, 105

DDA Discrete Dipole Approximation. See [Evlyukhin 2011] and references therewithin. 2

diagonal scalar T-matrix assumption the T-matrix of the individual N scatterers is assumed to be diagonal in p, and scalar for every multipolarity index n, *i.e.* $t_{n,m,\nu,\mu} = \delta(n-\nu)\delta(m-\mu)t_n$. This is the case when the scatterer is a sphere made of homogeneous material, or for a shperically symmetric scatterer. These assumptions simplify the explicit formulas derived in this thesis, but the general method to derive them is compatible with the case of non-diagonal T-matrices (split ring resonator shapes for instance); they are made throughout the whole thesis, except in section 2.2. 2

DNA Deoxyribonucleic Acid : one of the base components of life on Earth, it stores genetic information. Its unique structure and properties make it a very interesting tool in nano-sciences : for instance, it can be used to fix a given distance between different nanoparticles in small or large-scale structures. 43, 46

ED Electric Dipole. 51

EMWs Electromagnetic waves. 33

GMT Generalised Mie Theory. 16, 17, 22, 42, 49, 51, 60

incoming field a field that is incoming from sources located outside of the considered spherical surface. The poynting vector flux through the surface is thus null. The radial dependence of incoming fields can be cast using spherical Bessel functions and their derivatives. 15, 71

IR Infrared electromagnetic radiation, *i.e.* wavelengths between $\approx$ 800 nm and 300 μm. Near IR: between 800 nm and 1.4μm. 47

LDOS Local Density of Optical states. See *e.g.* [Novotny 2006]. 10

MD Magnetic dipole. 47

optical antenna optical antennas are transducers in the visible spectrum of the electromagnetic field: they allow the conversion of the electromagnetic energy coming from the far-field to locally avaiable electromagnetic energy (*e.g.* into a sub-wavelength sized electric field intensity spot). 10, 41, 106

scattered field scattered fields are the multipole expansion fields that satisfy scattering boundary conditions, the Poynting flux is directed towards the exterior of the considered spherical surface, which thus encloses a source. The radial dependence of scattered fields can be cast using outgoing spherical Hankel functions and their derivatives. 15, 71

split ring resonator a planar or thick split-ring geometry that allows an easy "hybrid" coupling between the electric and magnetic induced dipoles (and/or between the different multipoles) of the structure. See section 2.2. 21, 30

visible spectrum visible electromagnetic radiation, *i.e.* wavelengths between $\approx$ 400 nm and $\approx$ 800 nm. 1, 3, 33, 55, 103

VPWs Vector Partial Waves, the incident and outgoing $\mathbf{M}_{n,m}$ and $\mathbf{N}_{n,m}$. See appendix A.2. 15, 77, 101

VSHs Vector Spherical Harmonics, $\mathbf{X}_{n,m}$, $\mathbf{Y}_{n,m}$ and $\mathbf{Z}_{n,m}$. See appendix A.3. 85

List of Mathematical Symbols

Greek symbols

angular frequency (ω) of the (harmonic) electromagnetic field under consideration. Most of the equations omit the $e^{-i\omega t}$ dependence of the fields. 15

coupling factor (γ) between 2 dipoles, resulting from the propagation of the dipole field from one dipole to the other, plus the polarization of the field (α). 23

cross sections (σ_{scat}, σ_{ext}) σ_{scat}, σ_{ext} are the scattering and extinction cross sections, respectively. See e.g. [Bohren 1983]. 25

decay rates ($\Gamma_{\text{rad}}, \Gamma_{\text{tot}}$) $\Gamma_{\text{rad}}, \Gamma_{\text{tot}}$ are the radiative and total decay rates of an emitter, respectively. Any given value of Γ is a normalized (dimensionless) decay rate, ratio of the decay rate with the antenna structure over the decay rate in the embedding medium, Γ_0. For clarity a tilde is often used in this context, e.g. $\tilde{\Gamma}_{\text{rad}} = \Gamma_{\text{rad}}/\Gamma_0$. 42, 63

dimensionless polarizabilities ($\tilde{\alpha}$) polarizability divided by the volume of the scatterer. For spheres of radius a, $\tilde{\alpha} = \alpha/(4\pi a^3)$. 56

permittivity (ε) relative permittivity of a medium; ε_0 is the (absolute) permittivity of vacuum. 34

pi (π) ratio of the perimeter of a circle to its diameter. 13

quantum efficiency (η) of an emission. η is the quantum efficiency if the initial emitter is perfect ($\eta_0 = 1$) while η_{eff} is the final (effective) quantum efficiency when considering a non-unit initial quantum efficiency. 6, 9, 18, 42, 46, 63

relative phase (ϕ) between two dipoles. $\phi = \arg(p_2/p_1)$. 24

wavelength (λ) wavelength of the impeding light. Unless specified otherwise, λ refers to λ_0, the wavelength of the corresponding radiation in vacuum. 15

Mathematical symbols

far-field phase shift ($\mathrm{e}^{i\Phi}$) that is due to the displacement of the i-th scatterer from the origin, $\mathrm{e}^{i\Phi} \equiv \frac{\mathrm{e}^{ikr_i}}{\mathrm{e}^{ikr_0}}$. Due to the far-field approximation, the numerical value is taken as the first significant term of the expansion of the phase shift in series of $1/r$ as $r \to \infty$, that is, $\mathrm{e}^{ik\hat{\mathbf{r}}\cdot\mathbf{u}_i}$, a quantity that is explicitly defined in each formula derivation. 59, 97, 100

imaginary number (i) $i \in \mathbb{C}$, $i^2 = -1$. 13

Roman symbols

cartesian base coordinates (x, y, z) (the reference coordinate system). 14

directivity (D_{dBi}) expressed in isotropic decibels (dBi). $D_{\text{dBi}} = 10\log(4\pi P/\Gamma_{\text{rad}})$ where P is the power per steradian emitted in the direction of interest and Γ_{rad} is the total radiative power of the antenna.

An isolated dipole radiates with a directivity of 1.76 dBi, while a perfectly isotropic radiation has a directivity of 0 dBi. 63

efficiencies (Q_{scat}, Q_{ext}) Q_{scat}, Q_{ext} are the scattering and extinction efficiencies, respectively. They are defined by the interaction cross section divided by a relevant geometric cross section, for a sphere of radius a : $Q = \sigma/(\pi a^2)$. When there are multiple scatterers the total cross section is divided by the sum of the geometric cross sections. 26

electric dipole moment ($\mathbf{p}$) $\mathbf{p}_0$ is the emitting dipole moment. 23

electric field ($\mathbf{E}$, E) $\mathbf{E}$ is the vector field associated to the electric field; E is the (complex) scalar electric field at one position, the projection of $\mathbf{E}$ on a specified or otherwise trivially inferred axis. The 0 or inc subscripts designate an incoming field; the scat subscript designates a scattered field; the tot subscript designates a total (incoming plus scattered) field; and the exc subscript designates an excitation field, sum of the incoming field plus the fields scattered by all the other scatterers except the one under consideration. 15

magnetic field ($\mathbf{H}$, H) Same as $\mathbf{E}$ but for the magnetic field instead of the electric field. 15

multipole expansion numbers (n, m) $n \in \mathbb{N}^*$ is the multipole order ($n = i$ refers to a 2^i-pole) and $m \in [-n..n]$ is the orbital number. See A.1. 30, 69, 73

number of scatterers (N) (generally assumed to be spheres) of the considered scattering system or optical antenna. This ensemble is indexed by the integer i. 14

origin (O) of the sperical or cartesian coordinate system. 14, 106

particle-centered radius ($\mathbf{r}_i$) radius centered on the i^{th} scatterer, $\mathbf{r}_i = \mathbf{r}_0 - \mathbf{u}_i$ where $\mathbf{r}_0$ is the radius centered on origin and $\mathbf{u}_i$ is the position vector. $|\mathbf{r}_i| = r_i$. 14, 82

position vector ($\mathbf{u}_i$) of the $i^{\text{th}} \in N$ scatterer. 14, 82, 106

radius (a) of a sphere. 25

spherical base coordinates (r, θ, φ) (standard conventions apply, see 1.9). 14

wavevector ($\mathbf{k}$, k) $\mathbf{k}$ is the considered wavevector ; k is the associated wavenumber, defined in a homogeneous medium by $k = \omega n_m / c_0$. 15, 34

Subscripts, superscripts and diacritical signs

Longitudinal (L) longitudinal coupling: the 2 or more interacting dipoles are parallel to each other and oriented along the line that intersects them both. 22

Transverse (T) transverse coupling: the 2 or more interacting dipoles are parallel to each other and oriented perpendicularly to the line that intersects them both. 22, 100

Bibliography

[Abramowitz 1972] M. Abramowitz and I.A. Stegun. Handbook of mathematical functions with formulas, graphs, and mathematical tables. Selected Government Publications. Wiley, 1972. (Cited on pages 35 and 93.)

[Albella 2013] Pablo Albella, M. Ameen Poyli, Mikolaj K. Schmidt, Stefan A. Maier, Fernando Moreno, Juan José Sáenz and Javier Aizpurua. *Low-Loss Electric and Magnetic Field-Enhanced Spectroscopy with Subwavelength Silicon Dimers*. The Journal of Physical Chemistry C, vol. 117, no. 26, pages 13573–13584, 2013. (Cited on pages 23, 46 and 67.)

[Aouani 2011] Heykel Aouani. *Optical nanoantennas to enhance and control molecular fluorescence in subwavelength volumes*. PhD thesis, Université Paul Cézanne - Aix-Marseille III, September 2011. (Cited on pages 19 and 20.)

[Bharadwaj 2007] Palash Bharadwaj and Lukas Novotny. *Spectral dependence of single molecule fluorescence enhancement*. Opt. Express, vol. 15, no. 21, pages 14266–14274, Oct 2007. (Cited on page 18.)

[Bharadwaj 2009] Palash Bharadwaj, Bradley Deutsch and Lukas Novotny. *Optical Antennas*. Adv. Opt. Photonics, vol. 1, no. 3, pages 438–483, Nov 2009. (Cited on page 10.)

[Bohren 1983] Craig F. Bohren and Donald R. Huffman. Absorption and scattering of light by small particles. Wiley science paperback series. Wiley, 1983. (Cited on pages 4, 88, 93 and 105.)

[Bonod 2010] Nicolas Bonod, Alexis Devilez, Brice Rolly, Sebastien Bidault and Brian Stout. *Ultracompact and unidirectional metallic antennas*. Phys. Rev. B, vol. 82, no. 11, page 115429, SEP 16 2010. (Cited on page 53.)

[Busson 2011] Mickael P. Busson, Brice Rolly, Brian Stout, Nicolas Bonod, Eric Larquet, Albert Polman and Sébastien Bidault. *Optical and Topological Characterization of Gold Nanoparticle Dimers Linked by a Single DNA Double Strand*. Nano Lett., vol. 11, no. 11, pages 5060–5065, 2011. (Cited on pages 43 and 45.)

[Busson 2012a] Mickael P. Busson, Brice Rolly, Brian Stout, Nicolas Bonod and Sébastien Bidault. *Accelerated single photon emission from dye molecule-driven nanoantennas assembled on DNA*. Nat. Commun., vol. 3, page 962, July 2012. (Cited on pages 44 and 46.)

[Busson 2012b] Mickaël P. Busson, Brice Rolly, Brian Stout, Nicolas Bonod, Jérôme Wenger and Sébastien Bidault. *Photonic Engineering of Hybrid Metal–Organic Chromophores*. Angewandte Chemie International Edition, vol. 51, no. 44, pages 11083–11087, 2012. (Cited on page 46.)

[Campione 2011] Salvatore Campione, Sergiy Steshenko and Filippo Capolino. *Complex bound and leaky modes in chains of plasmonic nanospheres.* Opt. Express, vol. 19, no. 19, pages 18345–18363, Sep 2011. (Cited on page 35.)

[Carminati 2006] R. Carminati, J. J. Greffet, C. Henkel and J. M. Vigoureux. *Radiative and non-radiative decay of a single molecule close to a metallic nanoparticle.* Opt. Commun., vol. 261, no. 2, pages 368–375, May 2006. (Cited on pages 42, 44 and 47.)

[Chew 1990] W.C. Chew. Waves and fields in inhomogeneous media. Van Nostrand Reinhold, 1990. (Cited on pages 37, 79, 86, 87 and 88.)

[Colas des Francs 2008] G. Colas des Francs, A. Bouhelier, E. Finot, J. C. Weeber, A. Dereux, C. Girard and E. Dujardin. *Fluorescence relaxation in the near–field of a mesoscopic metallic particle: distance dependence and role of plasmon modes.* Opt. Express, vol. 16, no. 22, pages 17654–17666, Oct 2008. (Cited on pages 4, 5, 42 and 90.)

[Conforti 2010] Matteo Conforti and Massimiliano Guasoni. *Dispersive properties of linear chains of lossy metal nanoparticles.* J. Opt. Soc. Am. B, vol. 27, no. 8, pages 1576–1582, Aug 2010. (Cited on pages 35, 38 and 40.)

[Crandall 2006] Richard E. Crandall. *Note on fast polylogarithm computation*, 2006. http://people.reed.edu/ crandall/papers/Polylog.pdf. (Cited on page 36.)

[Cruzan 1962] O.R. Cruzan. *Translational addition theorems for spherical vector wave functions.* Q. Appl. Math., vol. 20, no. 1, pages 33–40, 1962. (Cited on page 79.)

[Curto 2010] Alberto G. Curto, Giorgio Volpe, Tim H. Taminiau, Mark P. Kreuzer, Romain Quidant and Niek F. van Hulst. *Unidirectional Emission of a Quantum Dot Coupled to a Nanoantenna.* Science, vol. 329, no. 5994, pages 930–933, AUG 20 2010. (Cited on page 11.)

[Devilez 2010] Alexis Devilez, Brian Stout and Nicolas Bonod. *Compact Metallo-Dielectric Optical Antenna for Ultra Directional and Enhanced Radiative Emission.* ACS Nano, vol. 4, no. 6, pages 3390–3396, JUN 2010. (Cited on pages 11, 63 and 66.)

[Esteban 2010] R. Esteban, T. V. Teperik and J. J. Greffet. *Optical Patch Antennas for Single Photon Emission Using Surface Plasmon Resonances.* Phys. Rev. Lett., vol. 104, no. 2, page 026802, Jan 2010. (Cited on page 11.)

[Evlyukhin 2011] Andrey B. Evlyukhin, Carsten Reinhardt and Boris N. Chichkov. *Multipole light scattering by nonspherical nanoparticles in the discrete dipole approximation.* Phys. Rev. B, vol. 84, page 235429, Dec 2011. (Cited on pages 2, 67 and 103.)

[Geffrin 2012] J.M. Geffrin, B. García-Cámara, R. Gómez-Medina, P. Albella, L.S. Froufe-Pérez, C. Eyraud, A. Litman, R. Vaillon, F. González, M. Nieto-Vesperinas, J.J. Sáenz and F. Moreno. *Magnetic and electric coherence in forward- and back-scattered electromagnetic waves by a single dielectric subwavelength sphere.* Nat. Commun., vol. 3, pages 1171–, November 2012. (Cited on page 59.)

[Gomez-Medina 2011] Raquel Gomez-Medina, Braulio Garcia-Camara, Irene Suarez-Lacalle, Francisco Gonzalez, Fernando Moreno, Manuel Nieto-Vesperinas and Juan Jose Saenz. *Electric and magnetic dipolar response of germanium nanospheres: interference effects, scattering anisotropy, and optical forces.* J. Nanophotonics, vol. 5, page 053512, 2011. (Cited on page 57.)

[Gozhenko 2003] Victor V. Gozhenko, Leonid G. Grechko and Keith W. Whites. *Electrodynamics of spatial clusters of spheres: Substrate effects.* Phys. Rev. B, vol. 68, no. 12, page 125422, Sep 2003. (Cited on pages 23 and 67.)

[Greffet 2010] Jean-Jacques Greffet, Marine Laroche and Fran çois Marquier. *Impedance of a Nanoantenna and a Single Quantum Emitter.* Phys. Rev. Lett., vol. 105, no. 11, page 117701, Sep 2010. (Cited on page 10.)

[Jackson 1999] John David Jackson. Classical electrodynamics : Third edition. John Wiley & Sons, New York, 1999. (Cited on pages 3, 4 and 97.)

[Johnson 1972] P. B. Johnson and R. W. Christy. *Optical Constants of the Noble Metals.* Phys. Rev. B, vol. 6, pages 4370–4379, Dec 1972. (Cited on pages 4, 5 and 32.)

[Karaveli 2011] Sinan Karaveli and Rashid Zia. *Spectral Tuning by Selective Enhancement of Electric and Magnetic Dipole Emission.* Phys. Rev. Lett., vol. 106, page 193004, May 2011. (Cited on page 46.)

[Kerker 1980] Milton Kerker, Dau-Sing Wang and H. Chew. *Surface enhanced Raman scattering (SERS) by molecules adsorbed at spherical particles: errata.* Appl. Opt., vol. 19, no. 24, pages 4159–4174, Dec 1980. (Cited on pages 42 and 90.)

[Kerker 1983] M. Kerker, D.-S. Wang and C. L. Giles. *Electromagnetic scattering by magnetic spheres.* J. Opt. Soc. Am., vol. 73, no. 6, pages 765–767, Jun 1983. (Cited on page 57.)

[Khlebtsov 2006] B Khlebtsov, A Melnikov, V Zharov and N Khlebtsov. *Absorption and scattering of light by a dimer of metal nanospheres: comparison of dipole and multipole approaches.* Nanotechnology, vol. 17, no. 5, pages 1437–1445, MAR 14 2006. (Cited on page 23.)

[Khlebtsov 2013] Nikolai G. Khlebtsov. *T-matrix method in plasmonics: An overview.* Journal of Quantitative Spectroscopy and Radiative Transfer,

vol. 123, no. 0, pages 184 – 217, 2013. <ce:title>Peter C. Waterman and his scientific legacy</ce:title>. (Cited on page 67.)

[Kim 1988] Young Sik Kim, P.T. Leung and Thomas F. George. *Classical decay rates for molecules in the presence of a spherical surface: A complete treatment.* Surf. Sci., vol. 195, no. 1–2, pages 1–14, 1988. (Cited on pages 42 and 90.)

[Koenderink 2006] A. Femius Koenderink and Albert Polman. *Complex response and polariton-like dispersion splitting in periodic metal nanoparticle chains.* Phys. Rev. B, vol. 74, no. 3, page 033402, JUL 2006. (Cited on page 35.)

[Lereu 2008] A. L. Lereu, G. Sanchez-Mosteiro, P. Ghenuche, R. Quidant and N. F. Van Hulst. *Individual gold dimers investigated by far- and near-field imaging.* J. Microsc. (Oxford, U. K.), vol. 229, no. 2, pages 254–258, 2008. (Cited on page 10.)

[Li 2007] Jingjing Li, Alessandro Salandrino and Nader Engheta. *Shaping light beams in the nanometer scale: A Yagi-Uda nanoantenna in the optical domain.* Phys. Rev. B, vol. 76, page 245403, Dec 2007. (Cited on page 53.)

[Liaw 2010] J. W. Liaw, C. S. Chen and J. H. Chen. *Enhancement or quenching effect of metallic nanodimer on spontaneous emission.* J. Quant. Spectrosc. Radiat. Transfer, vol. 111, no. 3, pages 454–465, February 2010. (Cited on pages 42, 44 and 47.)

[Lindell 1994] I.V. Lindell. Electromagnetic waves in chiral and bi-isotropic media. The Artech House Antenna Library. Artech House, 1994. (Cited on page 31.)

[Linton 2009] C.M. Linton and I. Thompson. *One- and two-dimensional lattice sums for the three-dimensional Helmholtz equation.* J. Comput. Phys., vol. 228, no. 6, pages 1815 – 1829, 2009. (Cited on pages 35 and 37.)

[Markel 1993] V. A. Markel. *Coupled-dipole Approach to Scattering of Light from a One-dimensional Periodic Dipole Structure.* J. Mod. Opt., vol. 40, no. 11, pages 2281–2291, 1993. (Cited on page 23.)

[Mazur 1953] P. Mazur and B.R.A. Nijboer. *On the statistical mechanics of matter in an electromagnetic field. I: Derivation of the maxwell equations from electron theory.* Physica, vol. 19, pages 971 – 986, 1953. (Cited on page 31.)

[Mertens 2007] H. Mertens, A. F. Koenderink and A. Polman. *Plasmon-enhanced luminescence near noble-metal nanospheres: Comparison of exact theory and an improved Gersten and Nitzan model.* Phys. Rev. B, vol. 76, page 115123, Sep 2007. (Cited on page 52.)

[Mie 1908] Gustav Mie. *Beiträge zur Optik trüber Medien, speziell kolloidaler Metallösungen.* Ann. Phys. (Berlin, Ger.), vol. 330, no. 3, pages 377–445, 1908. (Cited on pages 2, 5, 6 and 16.)

[Noginova 2008] N. Noginova, G. Zhu, M. Mavy and M. A. Noginov. *Magnetic dipole based systems for probing optical magnetism.* J. Appl. Phys., vol. 103, no. 7, page 07E901, 2008. (Cited on page 30.)

[Nordlander 2004] P Nordlander, C Oubre, E Prodan, K Li and MI Stockman. *Plasmon hybridizaton in nanoparticle dimers.* Nano Lett., vol. 4, no. 5, pages 899–903, MAY 2004. (Cited on page 24.)

[Novotny 2006] L. Novotny and B. Hecht. Principles of nano-optics. Cambridge University Press, 2006. (Cited on pages 9, 10, 11, 86, 87, 88 and 103.)

[Novotny 2011] Lukas Novotny and Niek van Hulst. *Antennas for light.* Nat. Photonics, vol. 5, no. 2, pages 83–90, 2011. (Cited on page 10.)

[Palik 1998] E.D. Palik and G. Ghosh. Handbook of optical constants of solids. Academic Press, Boston, 1998. (Cited on page 25.)

[Pinchuk 2005] A Pinchuk and G Schatz. *Anisotropic polarizability tensor of a dimer of nanospheres in the vicinity of a plane substrate.* Nanotechnology, vol. 16, no. 10, pages 2209–2217, OCT 2005. (Cited on page 23.)

[Raab 2005] R.E. Raab and O.L. De Lange. Multipole theory in electromagnetism: Classical, quantum, and symmetry aspects, with applications. International Series of Monographs on Physics. OUP Oxford, 2005. (Cited on page 31.)

[Rolly 2011a] Brice Rolly, Brian Stout, Sebastien Bidault and Nicolas Bonod. *Crucial role of the emitter–particle distance on the directivity of optical antennas.* Opt. Lett., vol. 36, no. 17, pages 3368–3370, Sep 2011. (Cited on pages 52 and 97.)

[Rolly 2011b] Brice Rolly, Brian Stout and Nicolas Bonod. *Metallic dimers: When bonding transverse modes shine light.* Phys. Rev. B, vol. 84, page 125420, Sep 2011. (Cited on page 24.)

[Rolly 2012a] Brice Rolly, Betina Bebey, Sebastien Bidault, Brian Stout and Nicolas Bonod. *Promoting magnetic dipolar transition in trivalent lanthanide ions with lossless Mie resonances.* Phys. Rev. B, vol. 85, page 245432, Jun 2012. (Cited on page 46.)

[Rolly 2012b] Brice Rolly, Nicolas Bonod and Brian Stout. *Dispersion relations in metal nanoparticle chains: necessity of the multipole approach.* J. Opt. Soc. Am. B, vol. 29, no. 5, pages 1012–1019, May 2012. (Cited on pages 33, 36, 37 and 38.)

[Rolly 2012c] Brice Rolly, Brian Stout and Nicolas Bonod. *Boosting the directivity of optical antennas with magnetic and electric dipolar resonant particles.* Opt. Express, vol. 20, no. 18, pages 20376–20386, Aug 2012. (Cited on pages 11, 30 and 56.)

[Ruppin 1982] R. Ruppin. *Surface modes of two spheres.* Phys. Rev. B, vol. 26, no. 6, pages 3440–3444, Sep 1982. (Cited on pages 42 and 90.)

[Sersic 2009] Ivana Sersic, Martin Frimmer, Ewold Verhagen and A. Femius Koenderink. *Electric and Magnetic Dipole Coupling in Near-Infrared Split-Ring Metamaterial Arrays.* Phys. Rev. Lett., vol. 103, page 213902, Nov 2009. (Cited on page 30.)

[Stein 1961] Seymour Stein. *Addition theorems for spherical wave function.* Q. Appl. Math., vol. 19, pages 15–24, 1961. (Cited on page 79.)

[Stout 2001] B Stout, JC Auger and J Lafait. *Individual and aggregate scattering matrices and cross-sections: conservation laws and reciprocity.* J. Mod. Opt., vol. 48, no. 14, pages 2105–2128, NOV 20 2001. (Cited on pages 78, 85 and 86.)

[Stout 2002] Brian Stout, Jean-Claude Auger and Jacques Lafait. *A transfer matrix approach to local field calculations in multiple-scattering problems.* J. Mod. Opt., vol. 49, no. 13, pages 2129–2152, 2002. (Cited on pages 37, 79, 81 and 87.)

[Stout 2008] Brian Stout, J. C. Auger and Alexis Devilez. *Recursive T matrix algorithm for resonant multiple scattering: applications to localized plasmon excitations.* J. Opt. Soc. Am. A, vol. 25, no. 10, pages 2549–2557, Oct 2008. (Cited on pages 69 and 83.)

[Stout 2011] B. Stout, A. Devilez, B. Rolly and N. Bonod. *Multipole methods for nanoantennas design: applications to Yagi-Uda configurations.* J. Opt. Soc. Am. B, vol. 28, no. 5, pages 1213–1223, May 2011. (Cited on pages 10, 42, 87, 89, 90 and 100.)

[Stout 2012] Brian Stout, Brice Rolly, Mandiaye Fall, Jerome Hazart and Nicolas Bonod. *Laser-particle interactions in shaped beams : beam power normalization.* Journal of Quantitative Spectroscopy and Radiative Transfer, no. 0, 2012. (Cited on page 71.)

[Taminiau 2008] Tim H. Taminiau, Fernando D. Stefani and Niek F. van Hulst. *Enhanced directional excitation and emission of single emitters by a nano-optical Yagi-Uda antenna.* Opt. Express, vol. 16, no. 14, pages 10858–10866, Jul 2008. (Cited on page 11.)

[Tanabe 2008] Katsuaki Tanabe. *Field Enhancement around Metal Nanoparticles and Nanoshells: A Systematic Investigation.* J. Phys. Chem. C, vol. 112, no. 40, pages 15721–15728, 2008. (Cited on page 38.)

[Thomas 2004] M. Thomas, J.-J. Greffet, R. Carminati and J. R. Arias-Gonzalez. *Single-molecule spontaneous emission close to absorbing nanostructures.*

Appl. Phys. Lett., vol. 85, no. 17, pages 3863–3865, 2004. (Cited on pages 6 and 47.)

[Thommen 2006] Quentin Thommen and Paul Mandel. *Left-handed properties of erbium-doped crystals.* Opt. Lett., vol. 31, no. 12, pages 1803–1805, Jun 2006. (Cited on page 46.)

[Tsang 1980] L. Tsang and J. A. Kong. *Multiple scattering of electromagnetic waves by random distributions of discrete scatterers with coherent potential and quantum mechanical formalism.* J. Appl. Phys., vol. 51, no. 7, pages 3465–3485, 1980. (Cited on page 69.)

[Tsang 1985] Leung Tsang, Jin Au Kong and Robert T. Shin. Theory of microwave remote sensing. Wiley series in remote sensing. John Wiley & Sons New York, 1985. (Cited on pages 37 and 79.)

[Varault 2013] S. Varault, B. Rolly, G. Boudarham, G. Demésy, B. Stout and N. Bonod. *Multipolar effects on the dipolar polarizability of magneto-electric antennas.* Opt. Express, vol. 21, no. 14, pages 16444–16454, Jul 2013. (Cited on pages 31, 32 and 33.)

[Weber 1973] M. J. Weber, T. E. Varitimos and B. H. Matsinger. *Optical Intensities of Rare-Earth Ions in Yttrium Orthoaluminate.* Phys. Rev. B, vol. 8, pages 47–53, Jul 1973. (Cited on pages 46 and 47.)

[Yang 2010] Shu-Chun Yang, Hiromu Kobori, Chieh-Lun He, Meng-Hsien Lin, Hung-Ying Chen, Cuncheng Li, Masayuki Kanehara, Toshiharu Teranishi and Shangjr Gwo. *Plasmon Hybridization in individual Gold Nanocrystal Dimers: Direct Observation of Bright and Dark Modes.* Nano Lett., vol. 10, no. 2, pages 632–637, FEB 2010. (Cited on page 24.)

[Zou 2006] Shengli Zou and George C. Schatz. *Combining Micron-Size Glass Spheres with Silver Nanoparticles to Produce Extraordinary Field Enhancements for Surface-Enhanced Raman Scattering Applications.* Israel Journal of Chemistry, vol. 46, no. 3, pages 293–297, 2006. (Cited on page 63.)